Title
Metabolic Signatures of Prostate Cancer and Renal Cell Carcinoma using High-Resolution NMR and Hyperpolarized 13C MRI

Author
Sun, Jinny

Publication Date
2020

Peer reviewed|Thesis/dissertation

Metabolic Signatures of Prostate Cancer and Renal Cell Carcinoma using High-resolution NMR and Hyperpolarized 13C MRI

by

Jinny Sun

DISSERTATION

Submitted in partial satisfaction of the requirements for degree of

DOCTOR OF PHILOSOPHY

in

Bioengineering

in the

GRADUATE DIVISION

of the

UNIVERSITY OF CALIFORNIA, SAN FRANCISCO
AND
UNIVERSITY OF CALIFORNIA, BERKELEY

Approved:

DocuSigned by:
John Kurhanewicz
593BD10CA23A498...

John Kurhanewicz
Chair

DocuSigned by:
Sabrina Ronen
DocuSigned by:
Rahul Aggarwal
E870F084A5CA4CC...

Sabrina Ronen

Rahul Aggarwal

Committee Members

This dissertation is dedicated to my parents,

Linggan Qiu and Boqin Sun

And my grandfather,

Zuwen Qiu

ACKNOWLEDGEMENTS

I am extremely grateful for all of the opportunities and support that I have received from the scientific community at UCSF.

First and foremost, I would like to thank my thesis advisor, Dr. John Kurhanewicz, for introducing me to the wonderful world of metabolic imaging and supporting me during my graduate research. I am extremely grateful to John for providing me the opportunity to learn about and to conduct cutting-edge research here at UCSF. John nurtured my scientific curiosity and gave me the freedom to learn at my own pace, but made sure I never strayed too far. John's open and friendly attitude paved the way for a close, collaborative research group and I am proud to have been a part of the team.

I would also like to acknowledge my amazing mentors in the UCSF community. I would like to thank Dr. Sabrina Ronen and Dr. Rahul Agarwal for providing constructive feedback and support as members of my dissertation committee. I greatly appreciate all the time and advice you have given throughout my graduate career to guide my research directions and build collaborative networks to advance my research. I also appreciate Dr. Daniel Vigneron, Dr. Sabrina Ronen, Dr. Rahul Agarwal, and Dr. Niren Murthy for their scientific guidance as members of my qualifying exam committee. Dr. Sharmila Majumdar provided expert advice and mentorship as my Bioengineering graduate advisor. I would also like to thank Dr. Alexander Pines for taking me into his lab when I was an undergraduate at UC Berkeley and giving me the opportunity to learn about molecular imaging and to teach undergraduate chemistry classes. Sincere thanks to Matt Ramirez and Clancy Slack for mentoring me and making my first research experience memorable.

I would like to express my sincere gratitude to Dr. Renuka Sriram, who has been an inspiring mentor throughout my time at UCSF. She has provided countless scientific and personal guidance and shaped me into a better scientist. She taught me the importance of understanding every step of what I did, whether it was an experimental protocol or a new research direction, and showed me what it truly means to be an independent researcher.

Dr. Donna Peehl has also been an inspiring mentor during the latter part of my graduate work. Friendly and approachable, she provides insightful feedback with a positive attitude and always makes time to discuss new research results, scientific writing, and even career advice. She has helped me grow professionally and maximize my potential. I would like to also thank Dr. Hongjuan Zhao and Rosalie Nolley from Stanford for their friendly collaboration and expertise with patient tissues.

I greatly appreciate the opportunity to work closely with Dr. Robert Bok during my graduate work. Friendly and approachable, he has been an amazing mentor during my graduate studies. Despite his busy schedule with preclinical and clinical research, he always makes time to help with scientific studies and advise on project directions. His patience, thoughtfulness, and passion when teaching surgical techniques or discussing scientific results has been an inspiration when I train my mentees.

I extend my warmest appreciation to Romelyn Delos Santos, who has looked out for me since I joined the group and took care of the behind-the-scenes work despite her busy preclinical and clinical workload. She made me feel welcome and her fun, cheerful attitude kept me laughin. I would also like to thank Mark Van Criekinge for teaching me how to design, build, and fix all kinds of laboratory equipment (from centrifuges and lyophilizers to bioreactors and NMR spectrometers). I truly appreciate all of the jokes, life lessons, and rare Belgium beers he shared

with me during my dissertation work. Much thanks to Mark Kelly and Sukumar Subramaniam for helping me design new pulse sequences and troubleshoot issues with the NMR spectrometers. I would also like to thank members of the Ronen Lab (Chloe Najac, Marina Radoul, Pavithra Viswanath, Anne Marie Gillespie, Georgios Batsios) for sharing their expertise and lyophilizer throughout my graduate studies.

I would also like to thank members of the Kurhanewicz lab (Justin Delos Santos, Natalie Korn, Hecong Qin, Jessie Lee, Shubhangi Aggarwal, Jeremy Bancroft Brown, Joao Piraquive Agudelo, Dave Korenchan) for an enriching graduate experience both inside and outside of the lab. Thank you all for the thoughtful discussions and fun adventures, from eating all-you-can-eat hotpot to watching whales and indulging in our love for escaping rooms. It was a pleasure to work with you guys, and I am very fortunate to have learned from each of you. Thanks also to my friends in the Bioengineering program who introduced me to board games and kept me engaged, especially Dominic Tong for the lunches and brainstorming sessions.

Outside of UCSF, I would like to thank my family and friends for supporting me throughout my career. I am especially thankful to my father, mother, and grandfather for sparking my interest in biology and NMR. Special thanks to my west coast friends (Katherine Wei, Miriam Beyder, Jing Lu, Hank Fanchiu, Jennifer Jong, Thomas Chow, Richie Chen, Anisha Narayan, Joann Liang, Jessica Aduan) who celebrated my milestones with me and kept me sane throughout the years. Lastly, I am eternally grateful to my partner Erick Lu, for the late-night discussions, support and laughter. I am so lucky to have you in my life. Thank you for being on this journey with me.

Metabolic Signatures of Prostate Cancer and Renal Cell Carcinoma using High-Resolution NMR and Hyperpolarized ^{13}C MRI

Jinny Sun

ABSTRACT

Non-invasive techniques to assess metabolic reprogramming during cancer progression can be used to improve therapeutic selection and provide an early assessment of therapeutic response or resistance in individual patients. Prior studies have shown that metabolic reprogramming plays a key role in the development of prostate cancer and renal cell carcinoma (RCC). This dissertation further elucidates the metabolic alterations that occur in treatment-resistant prostate cancer and in patient-derived models of RCC using high-resolution nuclear magnetic resonance (NMR) spectroscopy and hyperpolarized (HP) ^{13}C magnetic resonance imaging (MRI), with the goal of identifying new non-invasive diagnostic imaging tools. Glycolysis, metabolism of pyruvate and glutamate via the tricarboxylic acid (TCA) cycle, glutaminolysis, and glutathione synthesis are upregulated in castration-resistant prostate cancer (CRPC) compared to their androgen-dependent counterparts, using human cell lines as well a treatment-driven transgenic murine model. These metabolic alterations were reversed in castration-resistant murine tumors by treatment with a secondary androgen pathway inhibitor, apalutamide, suggesting that early metabolic responses to treatment can be monitored using non-invasive imaging techniques. Furthermore, treatment-emergent small cell neuroendocrine prostate cancer, a consequence of protracted treatment with primary androgen deprivation therapy and secondary androgen pathway inhibitors, exhibits significantly upregulated glycolysis, TCA cycle metabolism of pyruvate and glutamate, and glutaminolysis, as well as

significantly altered redox capacity compared to castration-resistant prostate adenocarcinoma using patient-derived xenograft models. Finally, the metabolic differences associated with the tumor microenvironment were compared between various patient-derived models of RCC, finding that RCC patient-derived xenografts (PDXs) displayed higher redox capacity and were more proliferative than cells and tissue slices derived from the PDXs and maintained *ex vivo*. The work presented in this dissertation suggests that a combination of HP [1-^{13}C]pyruvate, [2-^{13}C]pyruvate, [5-^{13}C]glutamine, and [1-^{13}C]dehydroascorbate can be used to distinguish advanced prostate cancer and RCC subtypes in future HP ^{13}C MRI of patients for improved treatment selection and monitoring.

TABLE OF CONTENTS

CHAPTER ONE: Introduction 1

CHAPTER TWO: Optimization of Methods for NMR-based Metabolomics and Hyperpolarized ^{13}C MRI 9

2.1. Metabolomics and fluxomics using stable isotope tracers 10

2.2. Stable isotope labeling methods for preclinical research 12

2.2.1. Stable isotope labeling methods for preclinical cell and mouse models 12

2.2.2. Preclinical models of prostate cancer and renal cell carcinoma 14

2.3. Crude cell and tissue extraction methods 16

2.3.1. Quenching and harvesting of cells and tissues 16

2.3.2. Homogenization of cells and tissue 17

2.3.3. Extraction of cells and tissue for metabolomics 18

2.3.4. Solvent considerations for NMR 20

2.4. High-resolution NMR acquisition of cell and tissue extracts 21

2.4.1. Advantages of high-field NMR for metabolomics and fluxomics 21

2.4.2. Quantitative ^{1}H NMR of ^{13}C-labeled cell and tissue extracts 22

2.4.3. 1D and 2D NMR methods for ^{13}C isotopomer analysis 26

2.5. NMR-based ^{13}C isotopomer analysis 37

2.6. Oxygen consumption rate of cells and tissues 40

2.7. Hyperpolarized ^{13}C NMR and MRI of cell, tissue, and murine models 43

CHAPTER THREE: Resistance to Androgen Deprivation Therapy Leads to Altered Metabolism in Prostate Cancer Cell and Murine Models 46

3.1. Abstract 47

3.2. Introduction 48

3.3. Materials and Methods 50

3.4. Results 58

3.4.1. Glycolysis, TCA cycle metabolism, glutaminolysis, and redox capacity is increased in PC-3 versus LNCaP cells 59

3.4.2. Changes in glucose and glutamine metabolism in the TRAMP model in response to primary androgen deprivation therapy 69

3.5. Discussion 73

3.6. Future Directions 78

CHAPTER FOUR: Metabolic Adaptations of Treatment-Emergent Small Cell Neuroendocrine Prostate Cancer using Patient-Derived Xenograft Models 82

4.1. Abstract 83

4.2. Introduction 83

4.3. Materials and Methods 87

4.4. Results 90

4.5. Discussion 94

CHAPTER FIVE: Metabolic Comparisons of Patient-Derived Models of Renal Cell Carcinoma using NMR and Hyperpolarized ^{13}C MRI 97

5.1. Abstract 98

5.2. Introduction 100

5.2.1. Metabolic alterations of renal cell carcinoma 100

5.2.2. Preclinical models of renal cell carcinoma 103

5.3. Materials and Methods 103

5.4. Results 108

5.4.1. Validation of PDX models 108

5.4.2. Characterization of ^{13}C-glucose metabolism using high-resolution NMR 109

5.4.3. Characterization of glycolysis and redox capacity using hyperpolarized ^{13}C MRI 109

5.5. Discussion 117

REFERENCES 122

LIST OF FIGURES

CHAPTER TWO:

Figure 2.1. Overview of anaplerotic reactions involved in the TCA cycle 11

Figure 2.2. Changes in metabolite fractional enrichment over 24 hours in [1,6-$^{13}C_2$]glucose-labeled LNCaP cells 12

Figure 2.3. Metabolic comparison of [U-^{13}C]glucose-labeled NCI-H660 xenografts in subcutaneous and subrenal capsule sites 15

Figure 2.4. Effects of tissue extraction methods on spectral quality of 1D proton NMR 19

Figure 2.5. Representative 1D carbon spectra of [U-^{13}C]glucose acquired at 500 MHz and 800 MHz 23

Figure 2.6. Representative 1D proton spectra with and without ^{13}C-decoupling of a [U-^{13}C]glutamine-labeled cell extract 25

Figure 2.7. 1D proton spectra of [U-^{13}C]glucose-labeled tissue extract demonstrate ^{13}C isotope effects on ^{1}H chemical shifts 26

Figure 2.8. Representative 1D proton spectrum of the lipid fraction of LNCaP cells 27

Figure 2.9. Schematic of possible ^{13}C isotopomer patterns resulting from [U-^{13}C]glucose and [U-^{13}C]glutamine into the TCA cycle 28

Figure 2.10. Representative 1D carbon spectra of a [U-^{13}C]glucose-labeled cell extract 29

Figure 2.11. Schematic of NMR-detectable glutamate isotopomer patterns and representative 1D carbon spectra of a [U-^{13}C]glucose-labeled cell extract 30

Figure 2.12. 2D ^{1}H -^{1}H TOCSY spectra of a [U-^{13}C]glutamine-labeled cell extract 31

Figure 2.13. 2D ^{1}H-^{13}C HSQC spectrum of a [U-^{13}C]glucose-labeled cell extract 32

Figure 2.14. ^{13}C-glutamate and ^{13}C-asparate isotopomer regions from ^{1}H-^{13}C HSQC spectrum of a [U-^{13}C]glucose-labeled cell extract 33

Figure 2.15. Inversion efficiency of conventional 180° pulses and adiabatic pulses 34

Figure 2.16. 1D projections of ^{1}H-^{13}C HSQC pulse sequences 35

Figure 2.17. TCACALC GUI interface 39

Figure 2.18. Bioreactor schematic for oxygen consumption rate measurements of living cells and tissue in real time 41

Figure 2.19. Oxygen consumption rate measurements using fiber optics oxygen sensors, Oxygraph+, and Seahorse XFe24 42

CHAPTER THREE:

Figure 3.1. High-resolution NMR spectra of LNCaP and PC-3 cell extracts 59

Figure 3.2. Metabolic comparison of LNCaP and PC-3 cells 61

Figure 3.3. Key enzymes and associated cofactors were assessed in LNCaP and PC-3 cells using biochemical assays 62

Figure 3.4. ^{13}C Isotopomer modeling of [U-^{13}C]glucose-labeled LNCaP and PC-3 cells using TCACALC 63

Figure 3.5. 1D ^{1}H spectrum of the lipid fraction of LNCaP and PC-3 cell extracts 65

Figure 3.6. Oxygen consumption rate and relative substrate utilization for TCA metabolism of LNCaP and PC-3 cells 67

Figure 3.7. Relative mass contribution of ^{13}C-glucose to downstream metabolites 68

Figure 3.8. Gene expression pathway analysis of LNCaP and PC-3 cells 69

Figure 3.9. TRAMP treatment timeline and tumor volume changes in response to orchiectomy 70

Figure 3.10. High-resolution NMR spectra of TRAMP tumor extracts..... 70

Figure 3.11. Fractional enrichment profiles of TRAMP tumors labeled with [U-^{13}C]glucose or [U-^{13}C]glutamine..... 72

Figure 3.12. Key enzymes were assessed in TRAMP tumors using enzymatic assays 73

Figure 3.13. Schematic detailing the metabolic alterations observed between ADPC and CRPC 74

Figure 3.14. Tumor growth rate of CRPC TRAMP tumors treated with apalutamide 79

Figure 3.15. Relative changes in metabolite concentration in CRPC TRAMP tumors treated with apalutamide 79

Figure 3.16. Relative changes in fractional enrichment of [U-^{13}C]glucose-labeled CRPC TRAMP tumors treated apalutamide 80

CHAPTER FOUR:

Figure 4.1. Quantification of aqueous metabolites in aCRPC and t-SCNC PDX tumor extracts using 1D ^{13}C-decoupled proton NMR 91

Figure 4.2. Principal Component Analysis performed on 1D proton spectra of aCRPC and t-SCNC extracts labeled with [U-^{13}C]glucose and [U-^{13}C]glutamine..... 92

Figure 4.3. Fractional enrichment profiles of CRPC and t-SCNC PDX tumors labeled with [U-^{13}C]glucose and [U-^{13}C]glutamine 93

Figure 4.4. Schematic detailing the metabolic alterations observed between aCRPC and t-SCNC tumor..... 95

CHAPTER FIVE:

Figure 5.1. Model propagation from murine orthotopic tumors to tissue slice culture and primary cell culture 102

Figure 5.2. Immunohistology and VHL gene mutation status of patient-derived RCC models 109

Figure 5.3. Representative 1D proton NMR spectra of patient-derived RCC models..... 110

Figure 5.4. Fractional enrichment profiles of patient-derived RCC models 113

Figure 5.5. Oxygen consumption rate of TSC and PDX tissues..... 114

Figure 5.6. Hyperpolarized [1-^{13}C]pyruvate metabolism of RCC tissue slices in an NMR-compatible TSC bioreactor..... 115

Figure 5.7. Hyperpolarized [1-^{13}C]pyruvate MRI and LDH activity using a RCC PDX model..... 116

Figure 5.8. Hyperpolarized [1-^{13}C] dehydroascorbate MRI using a RCC PDX model..... 117

LIST OF TABLES

CHAPTER TWO:

Table 2.1. High-field NMR spectrometers available at the University of California, San Francisco 22

Table 2.2. J_{CC} coupling constants for glutamate and aspartate 30

Table 2.3. J_{CH} constants of key metabolites 33

Table 2.4. Comparison of ^{13}C-metabolite quantification using 1D ^{1}H with presaturation versus 2D ^{1}H-^{13}C HSQC 36

Table 2.5. Existing ^{13}C isotopomer models for NMR and MS 38

CHAPTER THREE:

Table 3.1. Steady-state intracellular aqueous metabolite concentrations of unlabeled LNCaP and PC-3 cell extracts 60

Table 3.2. Steady-state lipid concentrations of unlabeled LNCaP and PC-3 cell extracts 66

Table 3.3. Steady-state aqueous metabolite concentrations of androgen-dependent and castration-resistant TRAMP tumors 71

CHAPTER FOUR:

Table 4.1. List of CRPC and t-SCNC PDX lines used in this study 87

CHAPTER FIVE:

Table 5.1. Metabolic profiling of patient-derived RCC models 112

LIST OF ABBREVIATIONS

1D	**One Dimensional**
2D	**Two Dimensional**
INEPT	**Insensitive Nuclei Enhanced by Polarization Transfer**
ADC	**Apparent Diffusion Coefficient**
ADPC	**Androgen-Dependent Prostate Cancer**
ADT	**Androgen Deprivation Therapy**
API	**Androgen Pathway Inhibitor**
AR	**Androgen Receptor**
ARN-509	**Apalutamide**
AS	**Active Surveillance**
ATCC	**American Type Culture Collection**
ATP	**Adenosine Triphosphate**
CDX	**Cell-Derived Xenograft**
CHIRP	**Compressed High Intensity Radiated Pulse**
CPMG	**Carr-Purcell-Meiboom-Gill Pulse Sequence**
CRPC	**Castration-Resistant Prostate Cancer**
D_2O	**Deuterated Water**
dDNP	**Dissolution Dynamic Nuclear Polarization**
DHA	**Dehydroxyascorbate**
DNP	**Dynamic Nuclear Polarization**
DSS	**4,4-dimethyl-4-silapentane-1-sulfonic acid**
ERETIC	**electronic reference to access in vivo concentrations**

FDG PET	**^{18}F-fluorodeoxyglucose Positron Emission Tomography**
FE	**Fractional Enrichment**
GARP	**Globally-Optimized Alternating-Phase, Rectangular Pulse**
GDH	**Glutamic Dehydrogenase**
GLS	**Glutaminase**
GPX2	**Glutathione Peroxidase**
GSEA	**Gene Set Enrichment Analysis**
GSH	**Reduced Glutathione**
GSS	**Glutathione Synthase**
HMDB	**Human Metabolome Database**
HP	**Hyperpolarized**
HSQC	**Heteronuclear Single Quantum Coherence Spectroscopy**
$HSQC_0$	**Extrapolated Time-Zero HSQC**
IHC	**Immunohistochemistry**
INEPT	**Insensitive Nuclei Enhanced by Polarization Transfer**
k_{pl}	**Pyruvate to Lactate Conversion Rate**
Lac	**Lactate**
LDH	**Lactate Dehydrogenase**
mCRPC	**Metastatic CRPC**
Met	**Metabolite of Interest**
mpMRI	**Multiparametric Magnetic Resonance Imaging**
MRI	**Magnetic Resonance Imaging**
MS	**Mass Spectrometry**

NMR	**Nuclear Magnetic Resonance**
OCR	**Oxygen Consumption Rate**
OXPHOS	**Oxidative Phosphorylation**
PBS	**Phosphate-Buffered Saline**
PC	**Pyruvate Carboxylase**
PCA	**Principal Component Analysis**
PDH	**Pyruvate Dehydrogenase**
PDX	**Patient-Derived Xenograft**
PSA	**Prostate Specific Antigen**
PULCON	**Pulse Length-Based Concentration Determination**
Pyr	**Pyruvate**
Q-HSQC	**Quantitative HSQC**
Q-OCCAHSQC	**Quantitative Offset-Compensated CPMG-Adjusted HSQC**
QQ-HSQC	**Quick Quantitative HSQC**
RCC	**Renal Cell Carcinoma**
RECIST	**Response Evaluation Criteria in Solid Tumors**
Ref	**Reference**
RF	**Radiofrequency**
ROI	**Region of Interest**
SCNC	**Small Cell Neuroendocrine Prostate Cancer**
SIRM	**Stable Isotope Resolved Metabolomics**
SNR	**Signal-to-Noise Ratio**
SRC	**Subrenal Capsule**

SubQ	**Subcutaneous**
t-SCNC	**Treatment-Emergent Small Cell Neuroendocrine Prostate Cancer**
TCA	**Tricarboxylic Acid Cycle**
TMS	**Tetramethylsilane**
TOCSY	**Total Correlation Spectroscopy**
TRAMP	**Transgenic Adenocarcinoma of the Mouse Prostate**
aCRPC	**Castration-Resistant Prostate Adenocarcinoma**
TSC	**Tissue Slice Culture**
TSP	**Trimethylsilylpropanoic Acid**
VitC	**Vitamin C, or Ascorbate**
YS	**Unidirectional Anaplerotic Flux Leading to Succinyl-CoA Relative to Citrate Synthase Flux**

CHAPTER ONE

Introduction

Cancer Metabolism – NMR-based Metabolomics

Metabolic reprogramming is a hallmark of oncogenic transformation that contributes to tumor growth, metastatic spread, and therapeutic resistance[1-4]. Alterations in metabolism reflect the combined effect of genomic, transcriptomic, and proteomic changes[5], which include the dysregulation of growth signaling pathways (e.g., PI3K, MYC) and mutations in tumor suppressor genes (e.g., p53, PTEN, VHL). Given the wide array of factors that influence cellular metabolism, the metabolic changes that occur during the progression of cancer and its response to treatment are still being elucidated. Understanding the specific changes in metabolic pathways and the settings in which they are altered can improve diagnosis of disease, monitoring response to treatment, and identification of new therapeutic targets.

Conventional metabolomic studies, also known as metabolic profiling, assess metabolic perturbations by measuring intracellular metabolite concentrations. However, this does not give a complete picture of the dynamics of cellular metabolism. In a simple A → B reaction scenario, increased flux through this pathway would result in measurable increased concentrations of the product. However, metabolic pathways are intrinsically interconnected, and the product may be used in several downstream reactions. Therefore, an increased pathway flux may not be detectable by measuring the concentration of the product metabolite if downstream pathway activities are also increased[6]. Furthermore, cellular homeostatic mechanisms regulate intracellular metabolite concentrations to be within nontoxic levels[6] and close to the K_M value of the associated enzymes to optimize reaction rates[7]. This greatly limits the ability of metabolomics, which relies on measurements of steady-state metabolite concentrations to detect metabolic perturbations.

Advances in nuclear magnetic resonance (NMR) and mass spectrometry (MS)-based stable isotope tracing methods such as ^{13}C isotopomer analysis, also known as metabolic flux analysis (MFA) and stable isotope-resolved metabolomics (SIRM), have improved our understanding of how changes in steady state metabolism and metabolic fluxes reflect oncogenic and microenvironmental changes during cancer progression and therapeutic response[8,9]. Ultimately, these techniques can be used to identify new metabolic biomarkers for the development of novel diagnostic and therapeutic targets[10,11]. However, there are major challenges in both acquiring the ^{13}C isotopomer data and its subsequent analysis that first must be solved. Currently, isotopomer analysis is most often performed using direct detect ^{13}C NMR spectroscopy, but this method is limited by the inherently low sensitivity of NMR and requires large quantities of tissue (>100 million cells or >200 mg tissue) that are infeasible to obtain for primary cell lines and patient tissue samples. Furthermore, ^{13}C NMR isotopomer analysis is limited by the absence of glutaminolysis in the existing isotopomer flux models. Chapter 2 of this dissertation discusses the techniques used to characterize key metabolic pathways associated with cancer progression and therapeutic response, including: (1) NMR-based metabolic profiling to quantify the concentrations of metabolites, and (2) NMR-based stable-isotope tracing to determine metabolic activity by measuring the fractional enrichment of metabolites and (3) hyperpolarized (HP) ^{13}C MRI to noninvasively assess metabolic fluxes and redox state.

Metabolism of Prostate Cancer and Metabolic Changes Associated with Therapeutic Response and Resistance

Prostate cancer is the most commonly diagnosed non-cutaneous cancer in men and the second leading cause of cancer death[12]. Due to over-diagnosis and over-treatment of indolent,

low-risk disease, active surveillance (AS) involving serial measurements of serum prostate-specific antigen (PSA) and biopsies as well as multiparametric MRI (mpMRI) has been implemented in the clinic to monitor disease progression and reduce rates of over-treatment[13,14]. A pressing need in the clinical management of patients with prostate cancer at the time of diagnosis is an accurate method for distinguishing aggressive, potentially lethal prostate cancer from indolent disease in individual patients in order to assess whether active surveillance (AS) is appropriate or aggressive treatment is needed[15]. Another important clinical need in the setting of advanced prostate cancer is the early assessment of therapeutic response and the development of therapeutic resistance in order to select new therapeutic approaches at an earlier and more effective time point[16,17]. This thesis focuses on determining metabolic changes associated with therapeutic response/resistance in order to identify HP ^{13}C labeled metabolic probes that could be used to non-invasively image therapeutic response/resistance in men receiving therapy for advanced prostate cancer.

Prostate metabolism is especially interesting due to the fact that normal prostate metabolism is quite unique. The prostate gland is responsible for producing and secreting large amounts of citrate. To do this, healthy prostate tissue accumulates very high levels of zinc due to upregulation of the zinc transporter hZIP-1 and down-regulates aconitase activity which inhibits citrate oxidation, resulting in a truncated TCA cycle[18,19]. The citrate is subsequently secreted from the prostate epithelial cell as a major component of semen. As a result, normal prostate exhibits an atypically higher glucose uptake as compared to other normal organs in order to fuel net citrate production and secretion.

In prostate cancer, there is a dramatic reduction of zinc uptake due to down-regulated hZIP-1-mediated transport, resulting in an upregulation of aconitase activity. Citrate is

subsequently oxidized in the TCA cycle to contribute to the energetic and synthetic requirements of cancer evolution and progression[20]. Furthermore, previous studies have shown that the rate of aerobic glycolysis ("Warburg effect") increases as prostate tumors become more aggressive[21-24].

Prostate cancer metabolism also changes in response to androgen deprivation therapy (ADT), which is the mainstay treatment for patients with advanced recurrent or metastatic prostate cancer. Initially all patients respond to ADT, which lowers serum testosterone to castration level and dramatically reduces tumor burden. A patient study also demonstrated that glycolytic activity was reduced after effective androgen deprivation therapy using HP ^{13}C MRI[25,26]. Eventually patients stop responding to ADT and develop castration-resistant prostate cancer (CRPC)[27,28]. Unfortunately, current biochemical and clinical biomarkers cannot reliably predict the development of CPRC, or subsequent response to therapy[29]. Furthermore, the metabolic phenotype of CRPC has not been fully defined. Chapter 3 of this dissertation will identify the differences in metabolism between androgen-dependent prostate cancer (ADPC) and CRPC using human cell lines and a transgenic adenocarcinoma of the mouse prostate (TRAMP) model of CRPC. This project has been designed to have a significant clinical impact by investigating metabolic changes that inform on the early development of CRPC and thereby providing information on which HP ^{13}C MRI probes should be used in patient studies.

Furthermore, CRPC includes two main subtypes: castration-resistant prostate adenocarcinoma (aCRPC) and treatment-emergent small cell neuroendocrine prostate cancer (t-SCNC). While small cell prostate cancer is typically a rare variant, presenting in less than 1% of all *de novo* prostate cancer cases, t-SCNC has become more prevalent due to the use of potent second-line androgen pathway inhibitors (APIs) such as enzalutamide, abiraterone, and apalutamide[30-32]. t-SCNC is an aggressive subtype of prostate cancer that is more lethal than

aCRPC and contributes to at least 25% of the 26,000 deaths from prostate cancer per year in the United States[33,34]. Both phenotypes often exist in the same patient, and patients with t-SCNC are expected to show poor response to new second-line androgen deprivation therapies. For example, Xtandi® (enzalutamide), which costs up to $129,000 for a year's course of treatment, is expected to have up to a 50% initial failure rate in this patient population. This suggests the need for new diagnostic methods and therapeutic targets to manage these treatment-resistant subtypes. A preliminary study indicating an early metabolic response to apalutamide using a TRAMP model of CRPC is presented in Chapter 3.

Recent genomic and metabolomic characterization of small cell neuroendocrine pancreatic[35] and lung[36] tumors have shown that a combined upregulation of the PI3K/AKT pathway and MYC expression lead to elevated aerobic glycolysis and glutaminolysis[37]. However, it is unknown whether t-SCNC utilizes glucose and glutamine differently from aCRPC tumors. Chapter 4 will investigate the metabolic alterations related to neuroendocrine transdifferentiation using patient-derived xenograft (PDX) models of CRPC and t-SCNC.

Metabolism of Patient-Derived Renal Cell Carcinoma Models

Renal cell carcinoma (RCC) is the most common type of kidney cancer and one of the top 10 malignancies in the United States, with ~50,000 Americans diagnosed each year and ~14,000 deaths[12]. Over the past 30 years, there has been a consistent increase in the diagnosis of RCC with no decline in mortality. This in part reflects over-diagnosis and over-treatment of clinically insignificant disease, as well as lack of reliable diagnostic tools to detect aggressive tumors at a curable stage[38]. Although several FDA-approved therapies have emerged for

treatment of metastatic RCC[39], all patients eventually demonstrate resistance and metastatic RCC remains an incurable disease.

Predictive preclinical RCC models such as PDXs, tissue slice cultures, and cell lines are needed to improve the diagnosis and treatment of RCC patients in the clinic. Each model has merits and drawbacks based on the representation of important biological features (intact stromal and epithelial architecture, microenvironment, tissue heterogeneity, gene expression and preservation of mutations). Traditional patient-derived cell lines and cell line-derived xenografts (CDXs) allow for high-throughput studies. However, these models generally do not accurately reflect the disease state found in patients and are a major factor in the low success rate of oncogenic drug development[40,41]. In contrast, PDXs and organoids better represent the composition of patient tumors and are preferred for preclinical drug development and biomarker discovery, but typically do not permit high-throughput studies. It is still unclear how fundamental biological processes in each preclinical model are altered by their respective experimental growth conditions, and a direct comparison of the metabolic phenotypes of these models has not yet been performed. Chapter 5 of this dissertation describes how metabolism is influenced by the respective environments and growth conditions of several patient-derived RCC models: *in vivo* PDXs, *ex vivo* culture of precision-cut tissue slices derived from PDXs, and *in vitro* culture of primary cells derived from PDXs.

The dissertation chapters are organized in the following manner:

Chapter 2 gives an overview of the methodologies used to study cancer metabolism and the optimization of each technique, including stable isotope tracer methods, cell and tissue

extraction techniques, high-resolution NMR acquisition and quantification of cell and tissue extracts, oxygen consumption measurements, ^{13}C isotopomer analysis, and HP ^{13}C MRI.

Chapter 3 investigates metabolic changes associated with androgen-independence using human prostate cancer cell lines and a transgenic murine (TRAMP) model of prostate cancer.

Chapter 4 examines metabolic alterations in treatment-emergent small cell neuroendocrine prostate cancer using patient-derived xenograft models.

Chapter 5 compares the metabolic phenotypes of patient-derived tissue models of renal cell carcinoma.

CHAPTER TWO

Optimization of Methods for NMR-based Metabolomics and Hyperpolarized ^{13}C MRI

2.1. Metabolomics and fluxomics using stable isotope tracers

Conventional metabolomic studies, also known as metabolic profiling, identify altered metabolic pathways based on changes in steady-state metabolite concentrations. While these studies are high-throughput, static measurements of steady-state metabolite concentrations provide little insight into the dynamics of cellular metabolism, which is characterized by multiple parameters including nutrient uptake, metabolite efflux rates, intracellular metabolite concentrations, metabolic pathway fluxes, and nutrient source of metabolite synthesis[42]. Most intracellular metabolites are tightly regulated to remain at low concentrations (pM to mM range) and are involved in complex, highly interconnected networks of metabolic pathways. For example, pyruvate is a central carbon metabolite at the intersection of several key metabolic pathways, and its intracellular concentration is typically in the μM range. As shown in **Figure 2.1**, pyruvate is the end product of glycolysis, but can also be produced from or converted into alanine and lactate. Pyruvate can be converted to acetyl-CoA through oxidative decarboxylation by the enzyme pyruvate dehydrogenase (PDH). Acetyl-CoA can either enter the TCA cycle, be utilized for fatty acid synthesis. Pyruvate can also undergo ATP-dependent carboxylation to oxaloacetate via pyruvate carboxylase (PC). In addition to pyruvate, the TCA cycle can also rely on other anaplerotic sources such as glutamine, which enters via glutamate, and odd-chain fatty acids undergoing β-oxidation, which enter via succinyl-CoA. Thus, the steady-state concentration alone identifies neither the source or the fate of pyruvate since it is involved in so many interconnecting metabolic pathways.

The source and fate of any metabolite of interest can be assessed using stable isotope tracers, which delineate metabolic pathways by providing quantitative knowledge of their intracellular fluxes. The study of metabolic fluxes using stable isotope tracers, also known as

fluxomics, consists of the following steps: experimental design to determine choice of stable isotope tracer, isotopic labeling experiments, sample preparation, and measurement of isotopic labeling using NMR or mass spectroscopy (MS). Quantitative metrics that can be determined using stable isotope tracers include: (1) concentrations of steady-state intracellular metabolites as well as extracellular metabolites that are exported into media such as lactate, (2) the fractional enrichment (FE) of a given metabolite, which is a measurement of the relative contribution of the ^{13}C-labeled tracer to the production of the metabolite of interest, and (3) the ^{13}C isotopomer labeling patterns and distribution, which are critical in the analysis of pathways such as the TCA cycle in which there is recycling of the metabolite of interest.

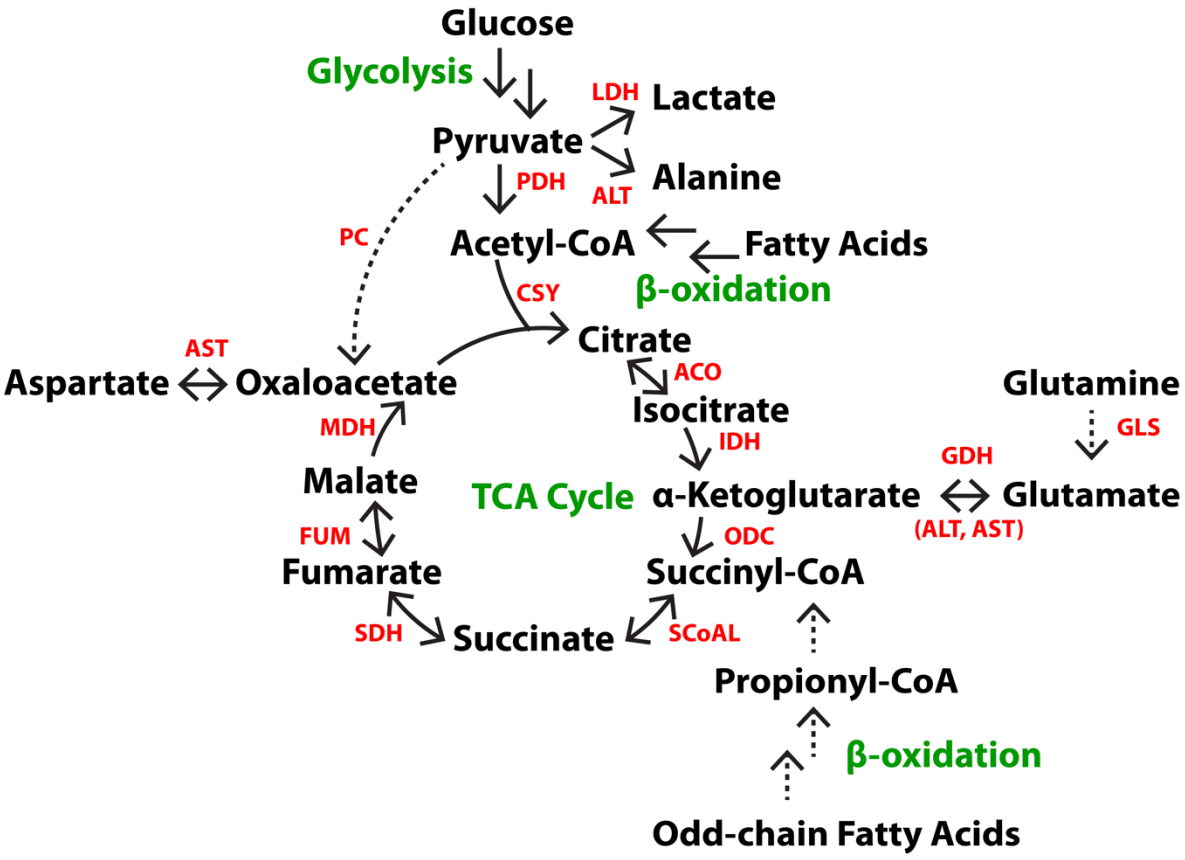

Figure 2.1. Overview of anaplerotic reactions involved in the TCA cycle. The metabolites (black) and enzymes (red) involved in each metabolic pathway (green) are shown. Dashed lines indicate anaplerotic pathways.

2.2. Stable isotope labeling methods for preclinical research

2.2.1. Stable isotope labeling methods for preclinical cell and mouse models

The most common stable isotope tracers permit measurements of ^{13}C FE of glucose, pyruvate, glutamine, and fatty acids (i.e., acetate, octanoate, palmitate)[43,44]. The best isotope tracers have high incorporation of the ^{13}C-label in downstream metabolites, and high accuracy and reproducibility in flux estimations[45,46]. The optimal isotopic tracer depends on which metabolic pathways are of greatest interest. [1,2-$^{13}C_2$]glucose is the best tracer to assess glycolysis and the pentose phosphate pathway (PPP), [U-^{13}C]glucose is ideal for analysis of pyruvate contribution to the TCA cycle, and [U-^{13}C]glutamine is preferred for analysis of glutaminolysis and glutamate contribution to the TCA cycle[45,46]. In addition to having high ^{13}C enrichment, the downstream metabolites also must be present in sufficient concentrations in order to be detected using NMR or MS. This is especially important for NMR-based methods

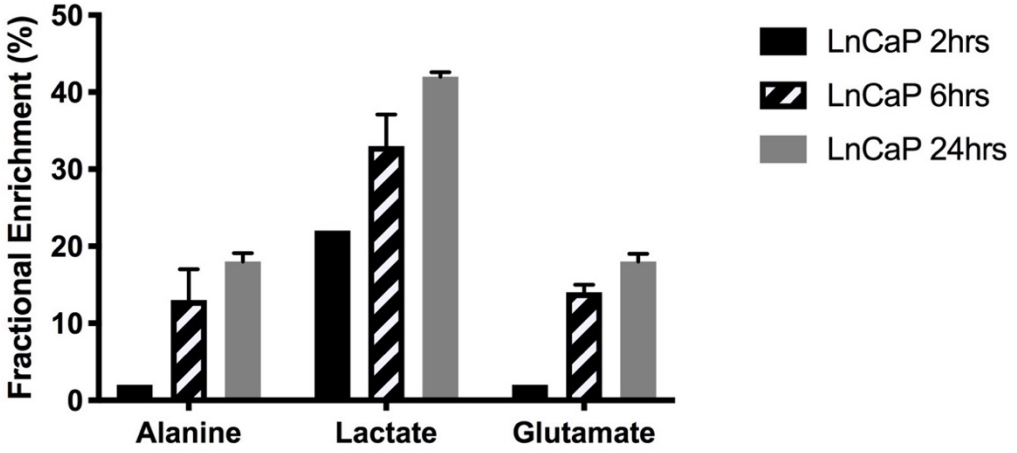

Figure 2.2. Changes in metabolite fractional enrichment over 24 hours in [1,6-$^{13}C_2$]glucose-labeled LNCaP cells. LNCaP cells labeled with [1,6-$^{13}C_2$]glucose for 2 hours (N=1) had the lowest alanine FE, lactate FE, and glutamate FE. No significant difference in %FE was observed between 6 hours (N=3) and 24 hours (N=4) of labeling. This suggests that steady-state isotopic labeling of [1,6-$^{13}C_2$]glucose was achieved after 6 hours. Significance was determined using Student's t-test. Data is presented as average ± standard error.

which can measure high-abundance metabolites such as glutamate and aspartate, but not small-abundance metabolites such as the intermediates of the TCA cycle.

For *in vitro* tracer studies using cell lines, stable isotope labeling can be performed by replacing the standard growth medium with a medium containing a ^{13}C-labeled compound of interest during the exponential growth phase of the cells. The ^{13}C-labeling time is dependent on metabolic rate of the cells, which can be estimated based on the cell population doubling time, and the relative rates of the metabolic pathways. For fast processes such as glycolysis and oxidative metabolism, cells must be incubated with the ^{13}C-enriched medium for a minimum of 6 hours for labeling of metabolites with ^{13}C-glucose and ^{13}C-glutamine to reach steady-state isotopic labeling[47,48], while slower pathways such as lipid synthesis require up to 96 hours of labeling. Here, LnCaP-FGC cells (doubling time of 36 hours) reached isotopic steady-state by 6 hours of labeling as evidenced by the plateauing of FE of downstream metabolites (**Figure 2.2)**.

If the culture medium needs to be supplemented with L-glutamine, it is recommended to use L-glutamine instead of GlutaMAX™ for metabolic studies. GlutaMAX™ is a dipeptide of alanine and glutamate that is used as a less toxic alternative to L-glutamine to prevent buildup of ammonia in the medium. Cells cleave the dipeptide bond in order to release the glutamine. However, this results in a large excess of alanine in the medium that alters the metabolic phenotype of the cells, since alanine can be metabolized via glycolysis, gluconeogenesis, and the TCA cycle. For these reasons, L-glutamine is preferred for metabolic studies.

For *in vivo* tracer studies, the method of administering stable isotope tracers is critical since metabolism can be altered due to anesthesia, physical trauma, and stress, which may confound the observed tumor metabolic signature. To reduce these effects, methods were adapted from Lane et al. (2015)[49]. In short, mice were briefly placed under anesthesia for bolus

injection via tail vein of either 80 μL of 25%wt/vol [U-^{13}C]glucose or 200 μL of 35.7 mg/mL [U-^{13}C]glutamine at 15 minute intervals over a total infusion time of 45 minutes.

2.2.2. Preclinical models of prostate cancer and renal cell carcinoma

Preclinical models that accurately reflect human tumor biology, disease progression, and therapeutic response are essential to drug development and biomarker discovery. Cell models are ideal for high-throughput drug screening and metabolomic studies since they can be grown in sufficient quantities and enable accurate assessment of specific tumor phenotypes due to their cellular homogeneity. However, patient tumors are typically heterogeneous which is one of the primary causes for therapeutic resistance and eventual failure. Prostate cancer is a heterogeneous disease in patients, often presenting with multiple foci of adenocarcinomas of varying pathologic Gleason grade within a single prostate gland[50] and, in the case of advanced disease, presence of small cell neuroendocrine as well as adenocarcinoma phenotypes. This results in spatial heterogeneity of genetic[50], transcriptomic[51,52], and metabolic[53] alterations. Similarly, intratumoral heterogeneity in renal cancer patients results in genetic[54,55], transcriptomic[56], and metabolic[57] variability and is one of the primary causes for therapeutic resistance and eventual lethality[54,55,58]. Therefore, it is critical to use preclinical murine models, such as xenograft and transgenic models, that more accurately depict the tumor heterogeneity and microenvironment observed in patients.

The tumor microenvironment also plays an important role in metabolism for mouse xenograft models[59-61], and is dependent on the graft site of the tumor. Previous studies using prostate PDX tumors have shown that the subrenal capsule (SRC) is highly vascular and more supportive of engraftment than subcutaneous (SubQ) sites[62]. The SRC is also a favorable site for

RCC xenograft models since the kidney is the orthotopic site. To determine whether tumor metabolism changes based on the graft site, stable isotope labeling studies using [U-^{13}C]glucose were performed to compare metabolism between SubQ and SRC xenografts derived from NCI-H660 cells (a preclinical model of SCNC) (**Figure 2.3**). SubQ and SRC tumors had similar lactate FE, indicating that the microenvironments of these graft sites had similar glycolytic activity. Tumors implanted in the SRC had higher aspartate FE and glutamate FE, indicating an increasing trend in pyruvate metabolism through the TCA cycle compared to SubQ tumors. This is most likely because the highly vascularized SRC site allows for fast delivery of oxygen and nutrients to the tumor. Thus, the SRC graft site is preferred for ^{13}C labeling studies of the TCA cycle.

PDX models often retain cellular heterogeneity and microenvironment observed in patients and may have a different metabolic phenotype than xenografts established from cell lines. More details on the metabolic alterations associated with microenvironment and growth conditions using patient-derived RCC models will be discussed in Chapter 5, which will compare PDX tumors, PDX-derived cell cultures, and *ex vivo* cultures of PDX-derived tissues.

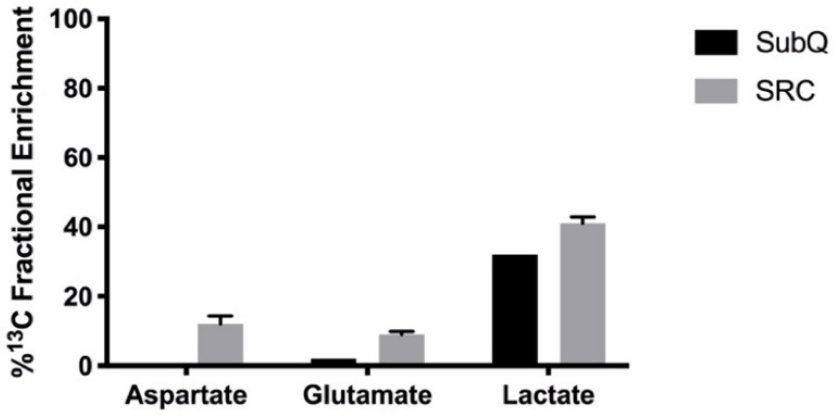

Figure 2.3. Metabolic comparison of [U-^{13}C]glucose-labeled NCI-H660 xenografts in subcutaneous and subrenal capsule sites. Metabolite fractional enrichments of subcutaneous (SubQ) (N=1) and subrenal capsule (SRC) (N=3) NCI-H660 tumors after [U-^{13}C]glucose labeling. Data is presented as average ± standard error (N=3 per group).

2.3. Crude cell and tissue extraction methods

2.3.1. Quenching and harvesting of cells and tissues

Rapid quenching of metabolism and harvesting of cells or tissues are essential to inactivate intracellular enzymes, halt metabolism, and avoid metabolite degradation and *ex vivo* alteration of the metabolic composition of the sample. In conventional quenching methods for *in vitro* ^{13}C-labeling studies, adherent cell lines are first detached using trypsin prior to quenching with solvents such as methanol. However, cells can undergo many metabolic changes during trypsinization, which occurs while cells are metabolically active at 37°C. Trypsin degrades membrane proteins that interact with intracellular metabolic enzymes, and the buffering solution in which trypsin is solubilized lacks essential nutrients required to maintain basal metabolism[63]. The labeling medium and culture medium should be saved if tracer consumption and extracellular metabolites that are exported into the medium need to be analyzed. After steady-state isotopic labeling has been reached, the cell culture dishes should be kept over ice to slow residual cellular activity. Cells should be rinsed with ice cold PBS to minimize contamination of metabolites originating from the culture medium. Optimal recovery of metabolites was obtained by directly quenching metabolism with cold methanol and then scraping cells off the surface of the cell culture dish. Based on protein quantification, scraping cells grown in tissue culture dishes results in higher recovery of cells than cells grown in tissue culture flasks, likely due to better access to the cells.

The speed of tissue collection and the temperature of sample storage can affect the measured metabolic profile[64]. For *in vivo* ^{13}C-labeling studies, tumor tissue is quickly harvested after euthanization of mice and either flash-frozen in liquid nitrogen for metabolic and biochemical studies or fixed with formalin, embedded in paraffin and sectioned for

immunohistochemical staining. Freezing of tissue should be prioritized over formalin-fixation since tissues remain metabolically active after euthanasia. To minimize metabolic perturbations associated with sample handling time and hypoxia, rapid freezing can be achieved by either freezing small amount of tissue (~30 mg) or using cryogenic tissue clamps, which quickly freezes tissue in thin (1-2 mm) sections. Freezing of bulk tissue sections is not recommended since the core of the tissue freezes at a slower rate than the surface of the tissue and will therefore remain metabolically active until complete freezing has occurred.

2.3.2. Homogenization of cells and tissue

The method of tissue homogenization plays an important role in the quality, efficiency, and reproducibility of metabolomic and fluxomic studies, biochemical assays, and gene expression analyses. Several homogenization techniques exist, including shearing methods (e.g., Dounce homogenizer, Potter-Elvehjem with PTFE pestle, rotor-stator homogenizer) and beating methods such as high-throughput homogenizers like the TissueLyser LT[65]. The Dounce homogenizer and Potter-Elvehjem with PTFE pestle require the most manual labor and have poor lysing efficiency for solid tissues since membrane fragments and organelles are oftentimes left intact. The rotor-stator homogenizer is one of the more popular methods and has similar lysing efficiency as the Dounce homogenizer and Potter-Elvehjem with PTFE pestle. However, this method is limited by the difficulty of cleaning the rotor, which increases the risk of cross-contamination, and heat generated during the lysing process[65]. In this dissertation, the Tissuelyser LT was used for almost all studies due to its high efficiency of lysis, minimal sample loss and cross-contamination, high-throughput, and ease of cleaning. To minimize heating during

the lysis process, cold reagents should be used and the homogenizer should be kept cool either by pre-cooling the insert or placing the entire setup in a cold room.

2.3.3. Extraction of cells and tissue for metabolomics

Cell and tissue extraction methods that remove macromolecules such as lipids and proteins are crucial for obtaining high-quality NMR and MS data. These macromolecules contribute to background signal or large peaks that may contaminate signals from the metabolites of interest. Extraction methods typically fall under two categories: (1) strong acid or base extraction methods using trichloroacetic acid and perchloric acid that denature and precipitate proteins, and (2) two-phase methods such as the Folch method[66] using mixtures of methanol, water, and chloroform to simultaneously separate aqueous and nonpolar metabolites and denature proteins which accumulate at the solvent interface[67]. Certain metabolites may be extracted preferentially depending on the specific method. For example, perchloric acid extraction results in higher concentrations of glutamate and other metabolites[68], while trichloroacetic acid extraction can degrade metabolites such as glutamine due to its highly acidic endpoint[69].

To determine which extraction method to use, perchloric acid and m/c/w extraction methods were compared using tumor tissue from the TRAMP model. No significant differences in metabolite concentrations were observed. However, the m/c/w extract had better solvent suppression, with a single water peak at 4.7ppm that was fully suppressed using presaturation pulses, while the perchloric acid extract had two large peaks at 4.7ppm and 4.9ppm (**Figure 2.4**). As a result, the perchloric acid extract had reduced spectral quality since the presaturation pulse was unable to fully suppress both peaks. The perchloric acid method was also not as high-

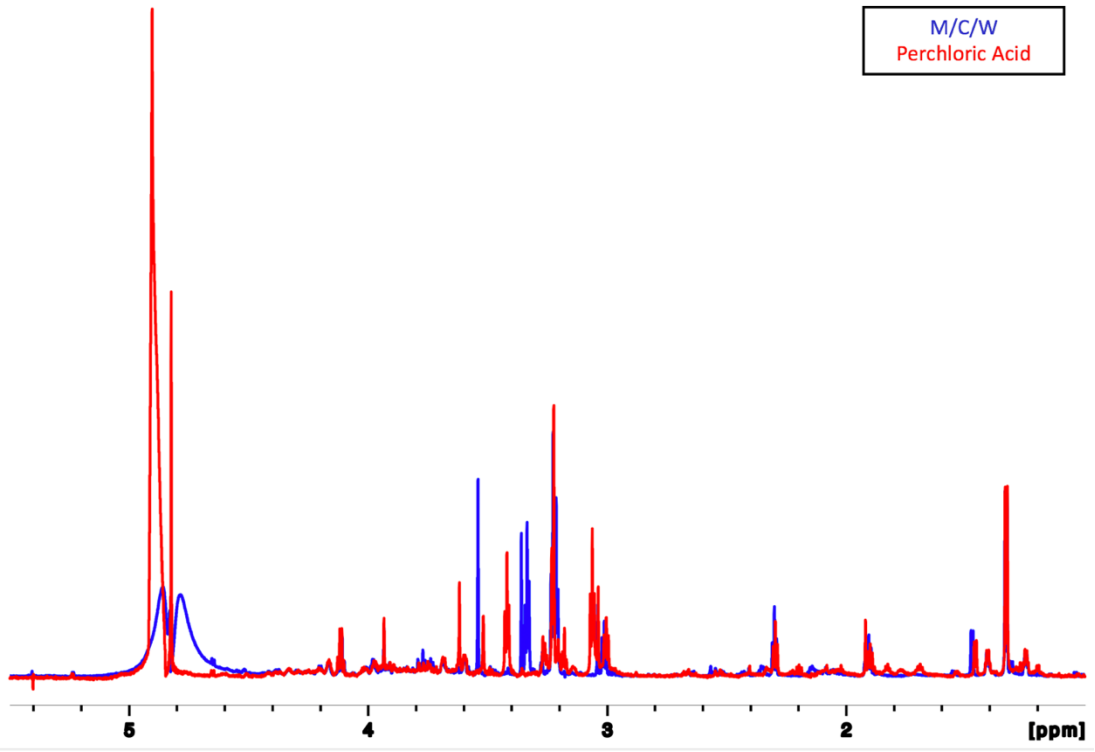

Figure 2.4. Effects of tissue extraction methods on spectral quality of 1D proton NMR. [U-^{13}C]glucose-labeled TRAMP tumor tissue was extracted using (blue) 1:1:1 methanol:chloroform:water (m/c/w) or (red) 8% perchloric acid. 1D proton spectra were acquired at 800 MHz and normalized to wet tissue weight. Some peaks have different chemical shifts due to differences in pH.

throughput due to the steps required (e.g., manual titration of potassium carbonate, removal of the sodium perchlorate precipitate, and pH adjustment) to neutralize and purify each sample. For the reasons listed above, the m/c/w extraction method was used in all subsequent cell and tissue studies.

An additional concern is the salinity of the sample after resuspension of the lyophilized extract, particularly for studies using >30 million cells, in the small volumes of solvent (200-600 µL) used for NMR. The high isotonicity of these extracts not only affects the quality of NMR acquisition but also the stability of the extract over time. The higher electrical conductivity of high salt concentrations can make it impossible to properly tune and match particularly for

cryogenic probes with low tolerance to salt. High salt samples also require longer ^{1}H 90° pulse durations and higher radiofrequency (RF) power for broadband ^{13}C-decoupling, resulting in sample heating, line broadening, dephasing artifacts, and possible damage to the probe. Together this results in lower signal-to-noise ratio (SNR) due to the reduced Q-factor of the probe and additional spectral noise introduced by the salt. The high salt content also affects the stability of the extract. White particulates precipitated out of solution after the lyophilized extract was solubilized, and the quality of the NMR spectra visibly deteriorated over time. The salinity of the cell extracts can be reduced by resuspending the lyophilized extract in subsequently smaller volumes of ice-cold water. This creates a supersaturated solution in which the excess salt remains crystallized and can be easily removed. For example, if the original extract was resuspended in 100 mL of water, it would be repeatedly lyophilized and resuspended in 10-fold smaller volumes of water (10 mL, 1 mL, 100 µL). For the final resuspension, approximately 20 µL of deuterated water (D_2O) was added to the lyophilized powder and the supernatant was then collected and diluted to a final volume of 600 µL with D_2O for NMR analysis.

2.3.4. Solvent considerations for NMR

For aqueous metabolites, D_2O was found to give the best lock signal and stability over time. For lipid quantification, deuterated chloroform ($CDCl_3$) was ideal for ^{1}H spectroscopy since it has a strong lock signal and stability over time. If ^{31}P NMR is of interest to detect phosphorylated lipids, then the lipid fraction should be resuspended in a buffered solvent such as a 2:1 mixture of $CDCl_3$ and 40 mM methanolic Cs-EDTA (200 mM EDTA in D_2O adjusted to pH 6.0 with CsOH, and further diluted five-fold with MeOH-d_3)[70]. Cation chelators such as Cs-EDTA can greatly

decrease NMR peak linewidths by removing metal cations such as magnesium and calcium that would otherwise cause peak broadening.

In order to quantify metabolite concentrations using NMR, an internal reference standard of 4,4-dimethyl-4-silapentane-1-sulfonic acid (DSS), tetramethylsilane (TMS), or 3-(trimethylsilyl)propionic (TSP) is typically used for biological samples. However, DSS and TSP can bind to proteins, nucleic acids and other macromolecules, which can affect quantification accuracy if these macromolecules are present. To prevent this, an external standard can be used by placing a coaxial insert (2.52 mm O.D. x 1.5 mm I.D.) filled with the standard inside a standard 5mm NMR sample tube to prevent mixing with the analyte. Standardless methods such as ERETIC (electronic reference to access in vivo concentrations)[71] or PULCON (pulse length based concentration determination)[72] can also be used to quantify metabolite concentrations with high accuracy and reproducibility.

2.4. High-resolution NMR acquisition of cell and tissue extracts

2.4.1. Advantages of high-field NMR for metabolomics and fluxomics

Crude extracts of cells and tissues are mixtures of small-molecule metabolites (<1500 Da), with over 40,000 metabolites identified in the Human Metabolome Database (HMDB)[73]. As such, the number of resolvable metabolite peaks that can be quantified using NMR is heavily limited by spectral crowding and sensitivity (detection limit is ~100 μM).

Metabolomic ^{1}H and ^{13}C NMR studies are typically conducted using spectrometers with magnetic field strengths ranging from 9.4T to 14.1T, with proton frequencies ranging from 400 MHz to 600 MHz. As shown in **Table 2.1**, spectral resolution, sensitivity, and quality can be improved by using high field spectrometers, inverse probes, cold preamps, and cryogenic probes.

Table 2.1. High-field NMR spectrometers available at the University of California, San Francisco.

	600 MHz Bruker AvanceIII	500 MHz Bruker AvanceDRX	800 MHz Bruker AvanceI
Field Strength	14.1 T	11.7 T	18.8 T
Probe	Double-resonance BBFO SmartProbe	Quad-resonance QCI cryoprobe	Triple-resonance TXI cryoprobe
Coil	Direct, Warm	Inverse, Cold	Inverse, Cold
$^{1}H/^{13}C$ Preamp	Warm/Warm	Cold/Cold	Cold/Warm
^{1}H SNR	875:1*	3800:1*	7000:1*
^{13}C SNR	235:1**	700:1**	700:1**

* ^{1}H SNR was measured using 1%Ethylbenzene in Chloroform-d
** ^{13}C SNR was measured using 40% Dioxane in Benzede-d6

Here, the spectral quality of one-dimensional (1D) ^{1}H and 1D ^{13}C spectroscopy was compared between two NMR systems equipped with cryoprobes: the 500 MHz Bruker AvanceDRX and the 800 MHz Bruker AvanceI. The 800 MHz spectrometer had superior spectral resolution and quality due to higher field strength and better water suppression. While the ^{13}C sensitivity was similar in both systems, the 800 MHz spectrometer was better at resolving complex ^{13}C isotopomer patterns due to the improved resolution at higher magnetic field strengths (**Figure 2.5**). For the reasons listed above, the 800 MHz spectrometer was used for all studies presented in this dissertation.

2.4.2. Quantitative ^{1}H NMR of ^{13}C-labeled cell and tissue extracts

Conventional NMR-based metabolic profiling relies on 1D ^{1}H water presaturation pulse and acquire spectroscopy to quantify metabolite concentrations in crude cell and tissue extracts,

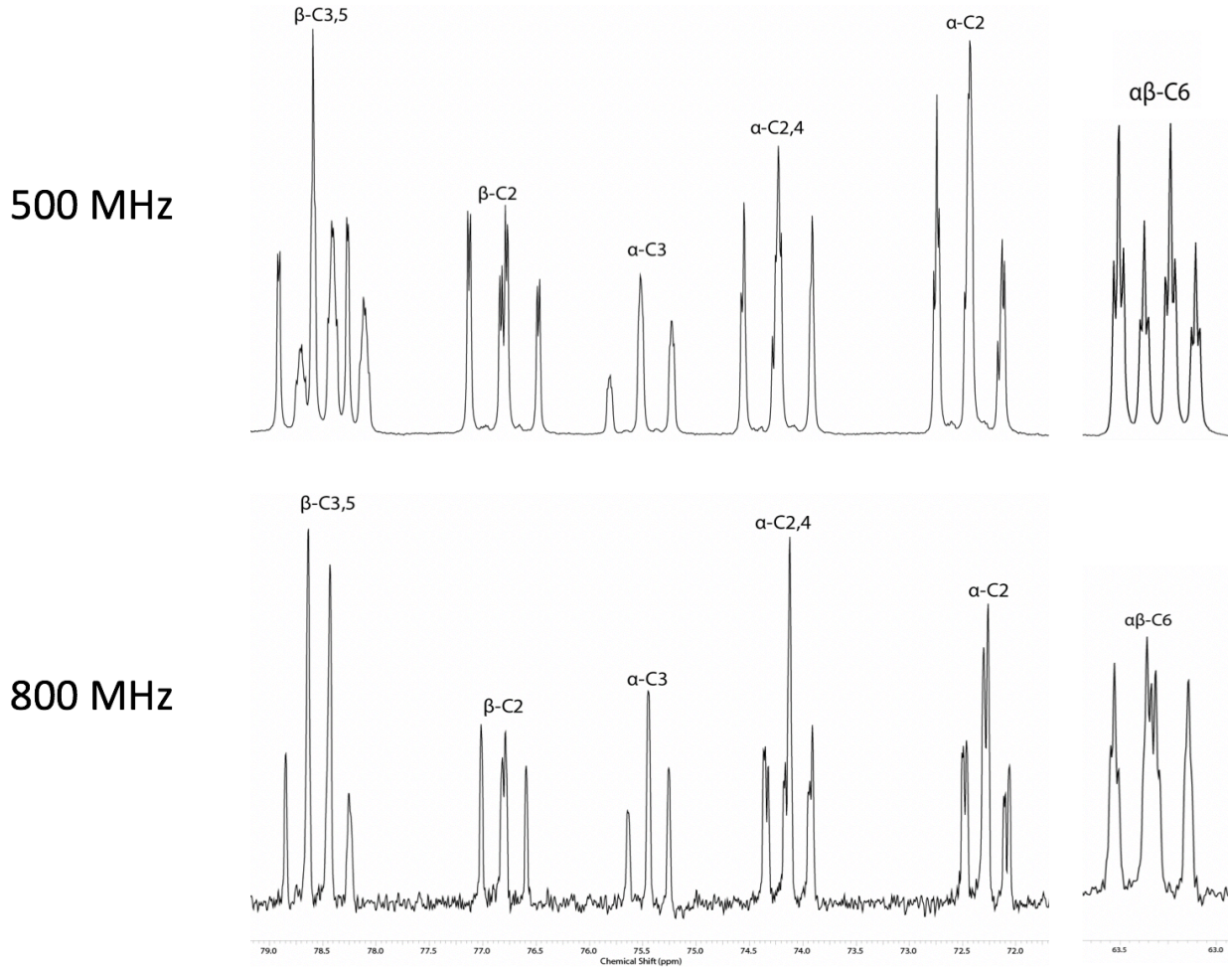

Figure 2.5. Representative 1D carbon spectra of [U-^{13}C]glucose acquired at 500 MHz and 800 MHz**.** 1D ^{13}C spectra of 25 mM [U-^{13}C]glucose in D_2O was acquired at (top) 500 MHz Bruker DRX equipped with quad-resonance QCI cryoprobe with cold ^{1}H and ^{13}C preamps and (bottom) 800 MHz Bruker AvanceI equipped with a triple-resonance TXI cryoprobe. The spectrum collected at 500 MHz has higher SNR than the spectrum collected at 800 MHz because more averages were collected.

which are complex mixtures that can contain thousands to millions of different small-molecule metabolites. This technique allows for high-throughput studies due to its short acquisition time and high sensitivity, with a detection limit in the μM range. Metabolite concentrations can be quantified based on an internal reference (Ref) standard using **Equation 2.1**[74]:

$$Moles_{Met} = \frac{Area_{Met}}{Area_{Ref}} * \frac{N_{1H,Ref}}{N_{1H,Met}} * Moles_{Ref} \qquad \textbf{(Equation 2.1)}$$

where $Area_{Met}$ and $Area_{Ref}$ are the fitted peak areas in the ^{1}H spectrum for the metabolite of interest (Met) and the reference (Ref) compound, respectively; $N_{1H,Met}$ and $N_{1H,Ref}$ are the number of equivalent protons in Met and Ref; $Moles_{Ref}$ is the number of moles of the reference compound. For 1D NMR, electronic standards such as ERETIC or PULCON can also be used to represent the $Moles_{Ref}$.

However, the low spectral resolution along the ^{1}H frequency dimension limits the accuracy of quantification and the number of quantifiable metabolites. This is further complicated for NMR-based ^{13}C isotopomer analysis, which requires quantification of the ^{13}C FE by dividing the area of the ^{13}C-^{1}H satellites (split based on the J_{CH} couplings) by the sum of the unlabeled and satellite peaks (**Equation 2.2**).

$$FE = \frac{Moles_{13C}}{Moles_{12C}+Moles_{13C}} \qquad \textbf{(Equation 2.2)}$$

This requires that the unlabeled and satellite peaks are resolvable. Extracts labeled with [U-^{13}C]glutamine are particularly challenging, in that the labeled and unlabeled glutamate, glutamine, and glutathione peaks have significant overlap with one another (**Figure 2.5**).

To more accurately quantify the total metabolite pool sizes, ^{13}C-decoupled ^{1}H water presaturation pulse and acquire spectra were acquired by applying adiabatic broadband ^{13}C-decoupling using a frequency-modulated compressed high intensity radiated pulse (CHIRP) with a 54kHz bandwidth (equivalent to 200ppm @ 800 MHz) and a shaped pulse power level of +2dB with respect to the power level determined for ^{13}C-GARP (globally-optimized alternating-phase, rectangular pulse). It was critical to cover the entire carbon bandwidth since long-range ^{13}C-^{1}H coupling was observed between carbonyl carbons and methyl protons in the beta-carbon position (i.e., lactate $^{13}C_1$ with lactate $^{13}C_3$ methyl protons). This collapses the ^{13}C-satellites to the central peak corresponding to unlabeled ^{12}C-^{1}H signal and enables quantification of overcrowded

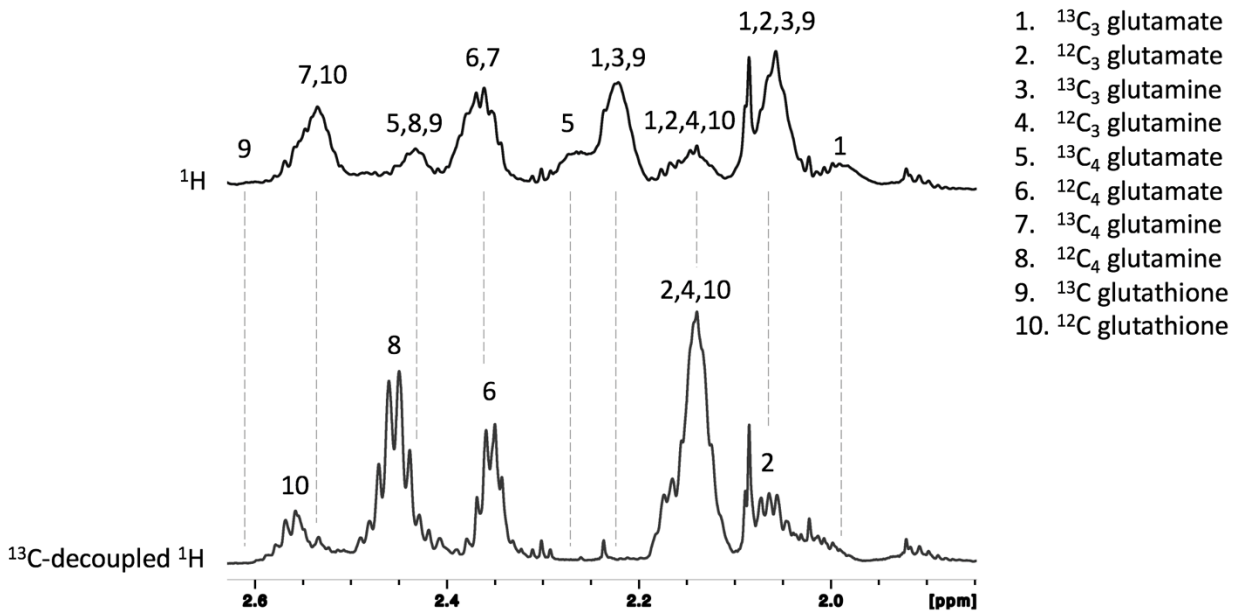

Figure 2.6. Representative 1D proton spectra with and without ^{13}C-decoupling of a [U-^{13}C]glutamine-labeled cell extract. Identification of ^{13}C-labeled and unlabeled glutamine, glutamate, and glutathione peaks in (top) ^{1}H spectra and (bottom) ^{13}C-decoupled ^{1}H spectra of 70 million PC-3 cells labeled with [U-^{13}C]glutamine for 24 hours.

regions such as glutamate, glutamine, and glutathione multiplets at ~2.4 ppm that are otherwise unresolvable (**Figure 2.6**). To minimize sample heating, an optimal acquisition time of 0.5 seconds with a repetition time of 12 seconds was found to maximize sensitivity without affecting spectral quality.

Interestingly the ^{13}C-satellites are not perfectly centered on the central peak corresponding to the unlabeled metabolite chemical shift because of the ^{13}C isotope effects on ^{1}H chemical shifts. This effect is typically not an issue since isotope shifts on ^{1}H are small (1-2ppb) and the natural abundance of ^{13}C nuclei is ~1.1%. However, the ^{13}C isotope shift is more noticeable in ^{13}C-enriched samples at high magnetic field strengths and can affect the accuracy of metabolite quantification, particularly for methods involving subtraction of ^{1}H spectra with and without ^{13}C-decoupling. Experimentally, the collapsed ^{13}C satellites for lactate (-CH_3) and

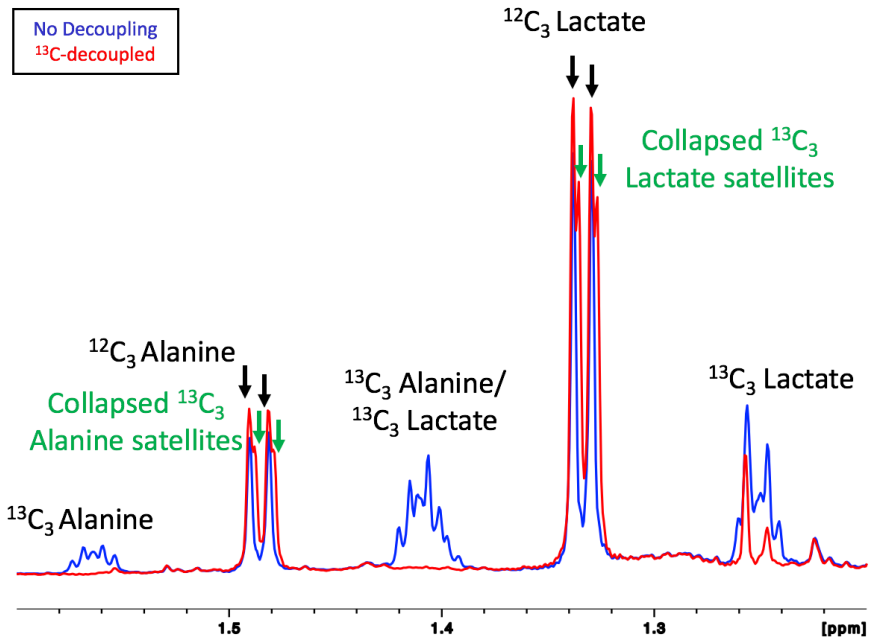

Figure 2.7. 1D proton spectra of [U-^{13}C]glucose-labeled tissue extract demonstrate ^{13}C isotope effects on ^{1}H chemical shifts. ^{13}C-decoupling collapses ^{13}C-^{1}H satellite peaks ~2 Hz upfield of the unlabeled ^{12}C-^{1}H peaks of alanine and lactate from LuCaP145.1 PDX tumor labeled with [U-^{13}C]glucose.

alanine (-CH_3) were ~2 Hz upfield of the central unlabeled ^{12}C-^{1}H chemical shifts (**Figure 2.7**), similar to literature findings[75].

Quantification of nonpolar lipids also provides essential and complimentary information on cellular metabolism. Conventionally this is extensively done using MS due to its high sensitivity and ability to distinguish individual molecular species of lipids. The main advantage of NMR-based methods is that metabolites are easily and reproducibly identified and quantified[76,77]. Representative 1D ^{1}H spectrum of the lipid phase is shown in **Figure 2.8**.

2.4.3. 1D and 2D NMR methods for ^{13}C isotopomer analysis

Isotopomer analysis is required to determine flux through complex metabolic pathways such as the TCA cycle, which recycles downstream metabolites and further complicates ^{13}C isotopomer

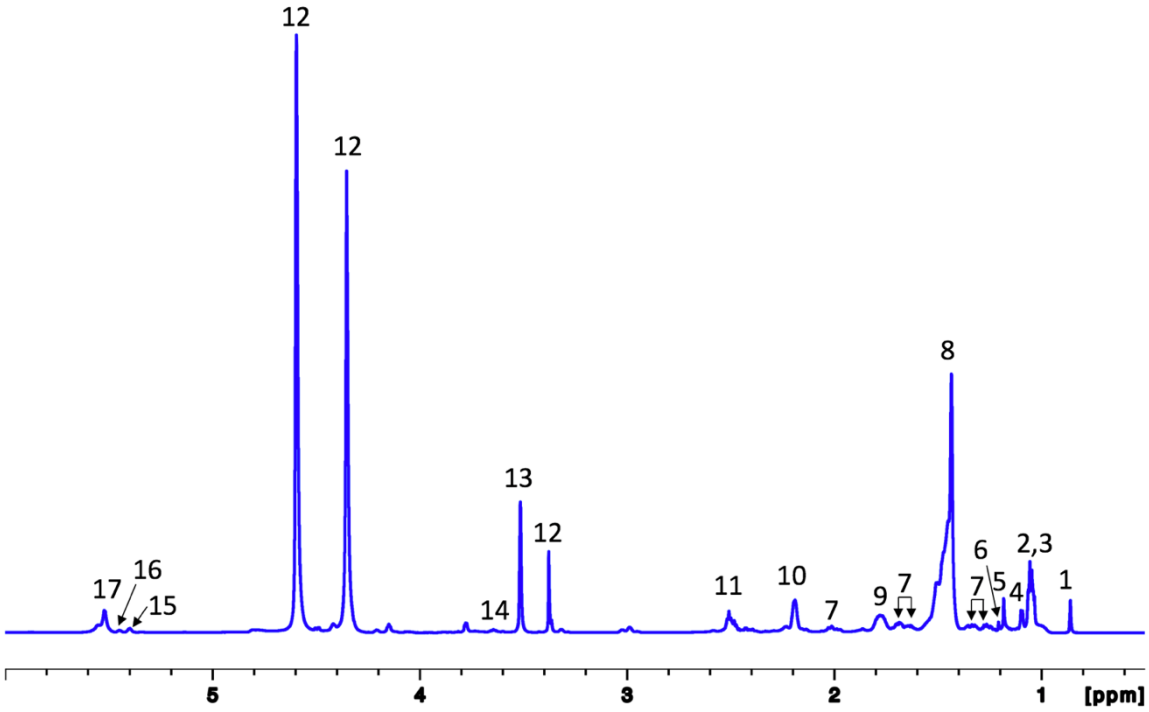

Figure 2.8. Representative 1D proton spectrum of the lipid fraction of LNCaP cells. The lipid fraction was isolated using m/c/w extraction. Peaks were assigned based on previous publications[76,77]: 1. Total cholesterol (C18 **H$_3$**), 2. Lipid (-C**H$_3$**), 3. Total cholesterol (C26 **H$_3$**/C27 **H$_3$**), 4. Total cholesterol (C21 **H$_3$**), 5. Free cholesterol (C19 **H$_3$**), 6. Esterified cholesterol (C19 **H$_3$**), 7. Multiple cholesterol protons, 8. Lipid (-CH$_2$-C**H$_2$**-CH$_2$-)$_n$, 9. Lipid (-CH$_2$-C**H$_2$**-CO), 10. Lipid (-CH$_2$-C**H$_2$**=CH), 11. Lipid (=CH-C**H$_2$**=CH), 12. Phosphatidylcholine, 13. Methanol, 14. Free cholesterol (C3 **H$_3$**), 15. Glycerophospholipid backbone, 16. Glycerol backbone, 17. Lipid (-**H**C=C**H**-).

patterns (**Figure 2.9**). Isotopomer peaks for ^{13}C-labeled metabolites have J_{CC} coupling constants that are unique to each metabolite (**Table 2.2**). Since NMR is not sensitive enough to detect the isotopomers of TCA cycle intermediates, NMR-based isotopomer analysis relies on modeling of the glutamate and aspartate isotopomers to model flux through glutaminolysis and the TCA cycle since (1) glutamate is found at high intracellular concentrations due to its compartmentalization in both the mitochondria and cytosol, (2) glutamate and aspartate multiplets are well resolved from other metabolites, (3) glutamate is assumed to be in rapid exchange with α-ketoglutarate, and (4) aspartate is assumed to be in rapid exchange with oxaloacetate.

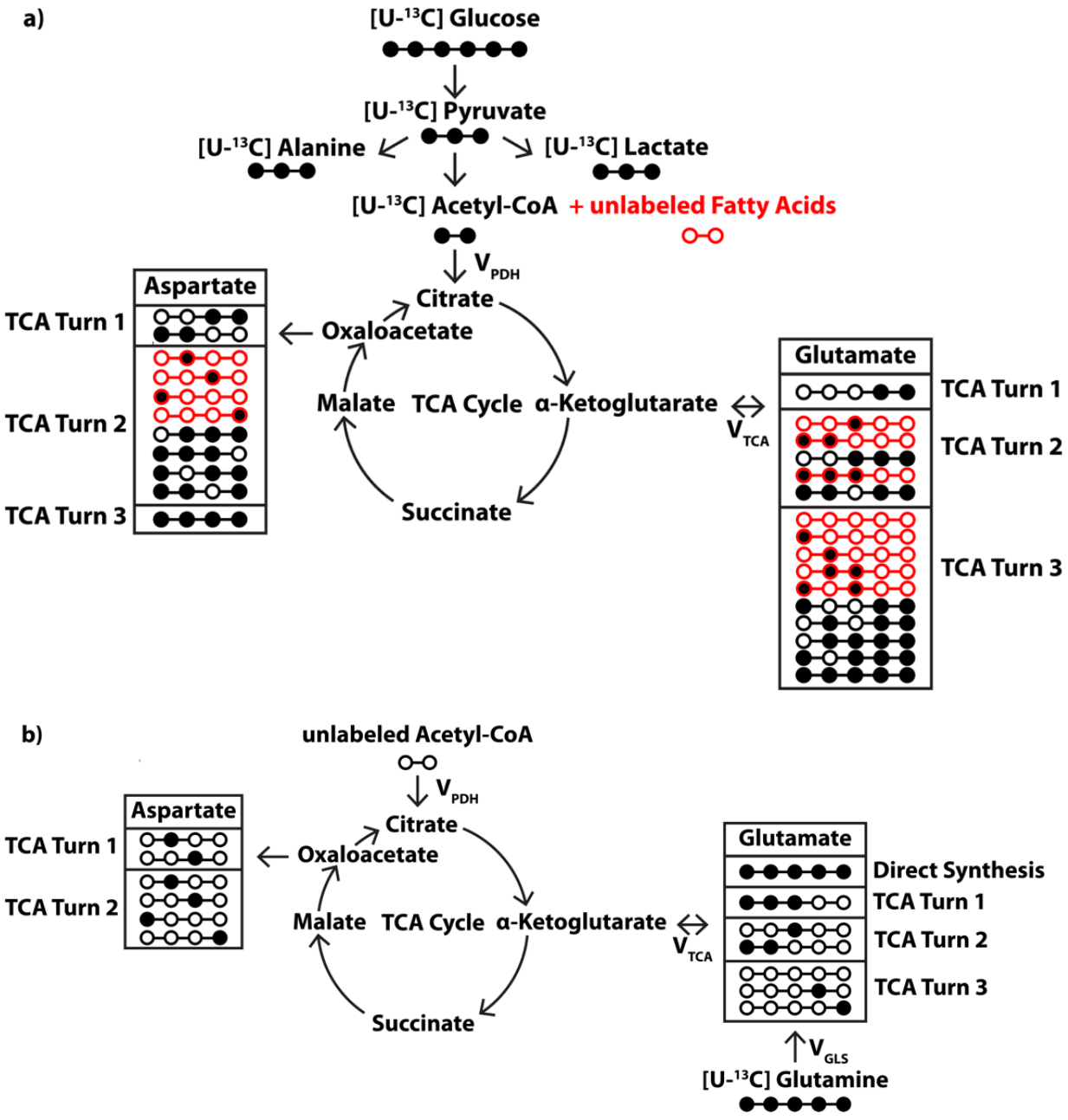

Figure 2.9. Schematic of possible ^{13}C isotopomer patterns resulting from metabolism of (a) [U-^{13}C]glucose and (b) [U-^{13}C]glutamine into the TCA cycle. Isotopomer patterns resulting from other anaplerotic pathways (e.g., pyruvate to oxaloacetate conversion via pyruvate carboxylase and reverse reactions (e.g., backconversion of α-ketoglutarate to citrate via IDH2) Reoccurring isotopomer patterns in subsequent turns of the TCA cycle are not shown. Solid circle=^{13}C-labeled carbon, open circle=unlabeled carbon.

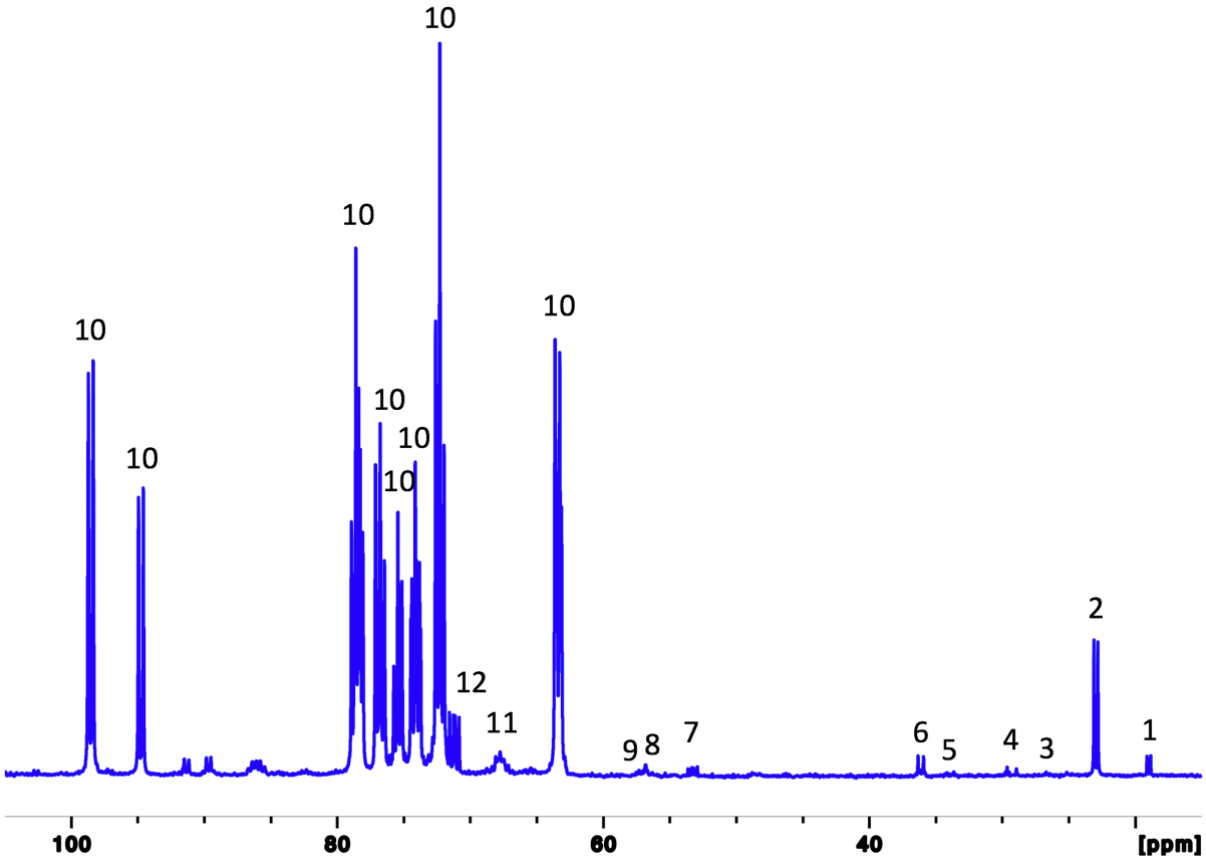

Figure 2.10. Representative 1D carbon spectra of a [U-^{13}C]glucose-labeled cell extract. Direct detect ^{1}H-decoupled ^{13}C spectra (6 hour acquisition) of 70 million PC-3 cells labeled with [U-^{13}C]glucose acquired using an 800 MHz spectrometer equipped with a cryoprobe. Peaks were assigned as: 1. Alanine C3, 2. Lactate C3, 3. Glutamine C3, 4. Glutamate C3, 5. Glutamine C4, 6. Glutamate C4, 7. Alanine C2, 8. Glutamine C2, 9. Glutamate C2, 10. Glucose, 11. Lactate C2, 12. Malate C2

NMR-based isotopomer analysis has conventionally used direct detect ^{13}C (**Figure 2.10**) to quantify ^{13}C-labeled metabolite concentrations and their relative ^{13}C isotopomer areas (Fan and Lane, 2016; Sherry and Malloy, 2002). The main advantage of direct detect ^{13}C NMR is that it is quantitative and can easily meet the resolution required to fully resolve all ^{13}C isotopomer peaks. For example, a digital resolution of at least 2 Hz is required to resolve the 7 Hz separation between glutamate C2 isotopomer peaks 2D12 and 2D23 (**Figure 2.11**). However, direct detect

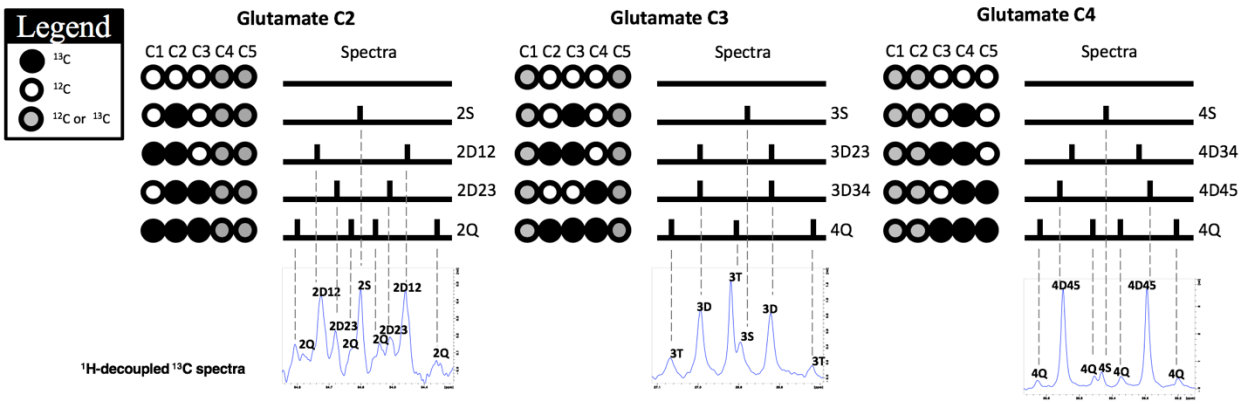

Figure 2.11. Schematic of NMR-detectable glutamate isotopomer patterns and representative 1D carbon spectra of a [U-^{13}C]glucose-labeled cell extract. Glutamate isotopomer patterns resulting from 60 million PC-3 cells labeled with [U-^{13}C]glucose were detected using ^{1}H-decoupled ^{13}C NMR with 6 hour scan time using an 800 MHz spectrometer.

^{13}C NMR requires large samples (~100 million cells) and high metabolite concentrations (>250 µmol) in order to obtain sufficient SNR (>10:1) within a reasonable scan time (< 24 hours). In this dissertation, several 1D and tw-dimensional (2D) NMR methods were developed on a high field 800 MHz NMR spectrometer equipped with a cryoprobe (**Table 2.1**) to reduce spectral overlap in overcrowded regions, improve quantification of the total metabolite pool sizes, and improve detection sensitivity of ^{13}C-labeled metabolites.

To measure isotopomers from low-concentration metabolites and small tissue samples, 2D indirect detection methods were optimized. 2D NMR spectroscopy has several advantages over 1D NMR spectroscopy that greatly benefit metabolomic and fluxomic applications[43]. The biggest advantage of 2D NMR for metabolomic analyses is its ability to resolve overlapping

Table 2.2. J_{CC} coupling constants for glutamate and aspartate

Metabolite	J_{12}	J_{23}	J_{34}	J_{45}
Aspartate	53 Hz	37 Hz	50 Hz	–
Glutamate	54 Hz	34 Hz	34 Hz	52 Hz

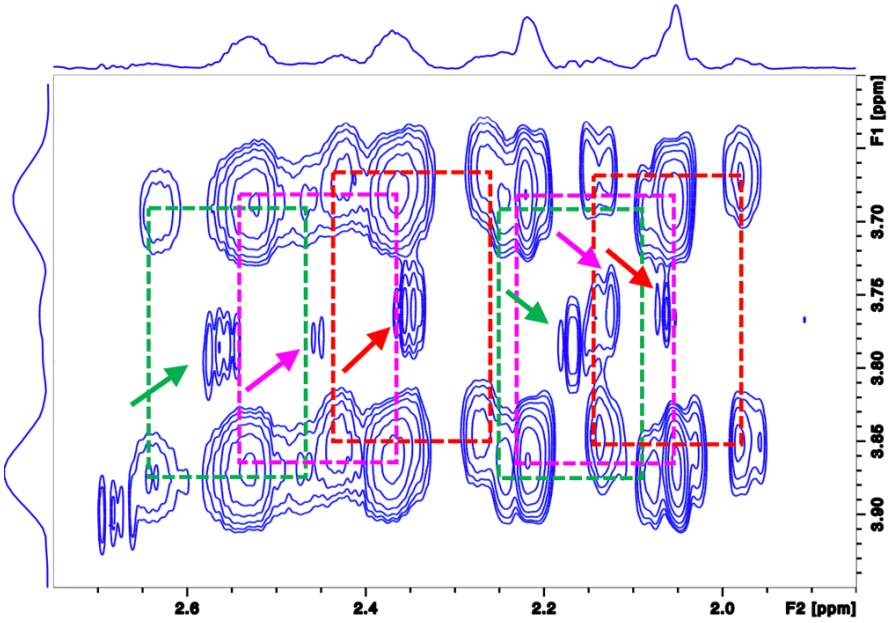

Figure 2.12. 2D ^{1}H -^{1}H TOCSY spectra of a [U-^{13}C]glutamine-labeled cell extract. Spectrum was acquired from 60 million PC-3 cells labeled with [U-^{13}C]glucose using an 800 MHz spectrometer. Acquisition time was 2 hours 45 minutes. Identification of ^{13}C-labeled satellites (dotted lines) and unlabeled central metabolite peaks (arrows) of glutamate (red), glutamine (magenta), and glutathione (green).

resonances in the direct dimension (i.e., ^{1}H) by allowing chemical shifts and coupling constants to develop across the indirect dimension (i.e., ^{1}H, ^{13}C). However, quantification of metabolite concentrations using 2D peak volumes is challenging since the magnetization transfer efficiency for each 2D cross-peak is non-uniformly influenced by several factors such as non-uniform excitation, non-uniform relaxation, evolution times, and mixing times.

2D TOCSY is commonly used to confirm metabolite identity and resolve overlapping resonances. The advantage of TOCSY is its potential to quantify more metabolites than 1D ^{1}H spectroscopy, which is limited by spectral overlap. Furthermore, the ^{13}C fractional enrichment can also be accurately quantified using TOCSY since each isotopomer has a unique cross peak pattern[78]. This makes TOCSY an attractive method for metabolomics and fluxomics. Absolute quantification of ^{1}H-^{12}C and ^{1}H-^{13}C peak volumes is challenging without calibration using

metabolite standards of known concentration due to the non-uniform factors influencing magnetization transfer efficiency. However, FE is quantifiable using TOCSY since the unlabeled and ^{13}C-labeled peaks of the same resonance are similarly influenced. As shown in **Figure 2.12**, TOCSY is particularly useful for the quantification of glutathione FE, since glutathione is not easily quantifiable using 1D ^{1}H spectroscopy due to spectral overlap and unresolvable isotopomer multiplets, particularly in samples labeled with [U-^{13}C]glutamine. Since the majority of metabolites have small spin systems (3-6 carbons) in crude extracts, a mixing time of 60 milliseconds was used for all ^{1}H -^{1}H TOCSY studies presented in this dissertation.

As HSQC is one of the most widely used 2D pulses, several variants exist. The most basic HSQC sequence on Bruker NMR spectrometers (hsqcgpph) is limited because (1) there is signal loss at the edges of the spectrum due to the inversion profile to transfer magnetization

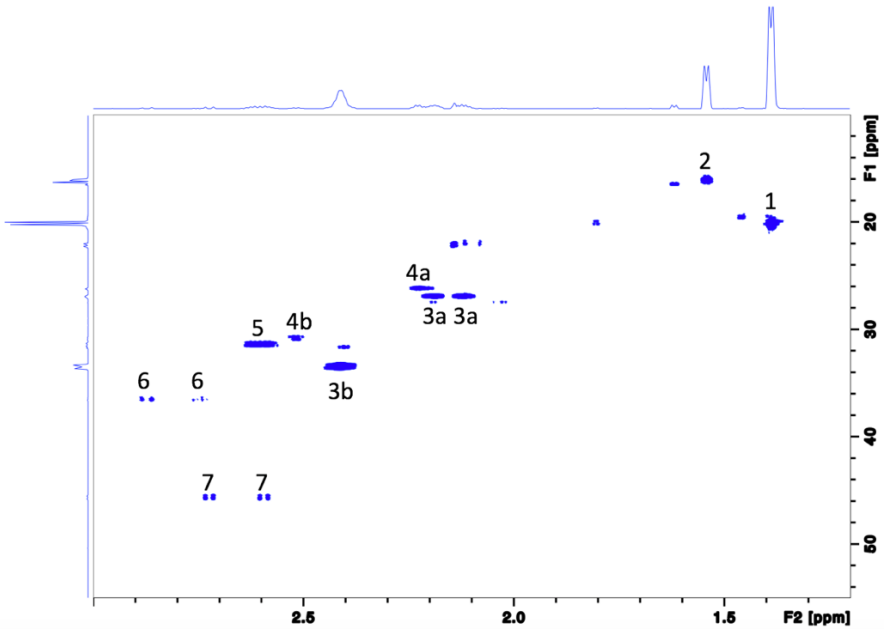

Figure 2.13. 2D ^{1}H-^{13}C HSQC spectrum of a [U-^{13}C]glucose-labeled cell extract. Spectrum was acquired from 60 million PC-3 cells labeled with [U-^{13}C]glucose using an 800 MHz spectrometer. Acquisition time was 4 hours. ^{13}C-labeled metabolites related to glycolysis, glutaminolysis and the TCA cycle were assigned as follows: 1. Lactate C3 **H$_3$**, 2. Alanine C3 **H$_3$**, 3a. Glutamate C3 **H$_2$**, 3b. Glutamate C4 **H$_2$**, 4a. Glutamine C3 **H$_2$**, 4b. Glutamine C4 **H$_2$**, 5. Glutathione C6 **H$_2$**, 6. Aspartate C3 **H$_2$**, 7. Malate C3 **H$_2$**.

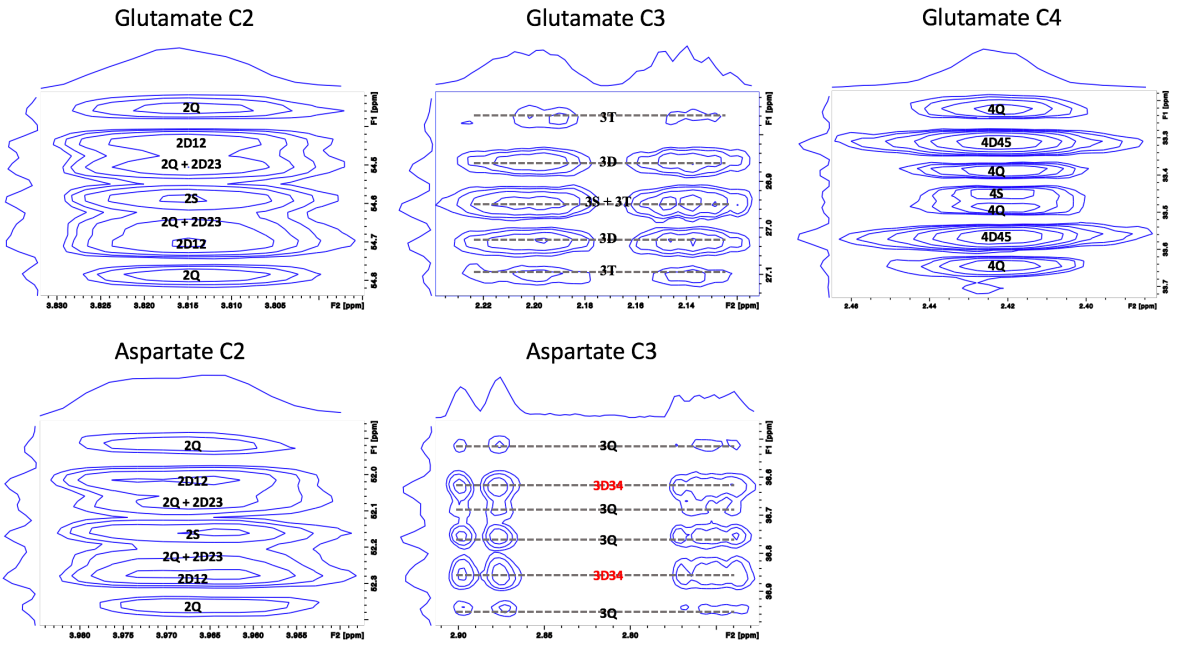

Figure 2.14. ^{13}C-glutamate and ^{13}C-asparate isotopomer regions from ^{1}H-^{13}C HSQC spectrum of a [U-^{13}C]glucose-labeled cell extract. Spectrum was acquired from 60 million PC-3 cells labeled with [U-^{13}C]glucose using an 800 MHz spectrometer. Acquisition time was 4 hours.

Table 2.3. J_{CH} constants of key metabolites.

Metabolite	**Carbon position**	**J_{CH} (Hz)**
Alanine	C3	130[74]
Aspartate	C2	144[79]
	C3	129,130[74,79]
Glutamate	C2	145[79]
	C3	130[74,79]
	C4	127[74,79]
Glutamine	C2	145[79]
	C3	131[79]
	C4	128[79]
Glutathione	C8 (Glutamate C2)	143.5
	C7 (Glutamate C3)	132
	C6 (Glutamate C4)	130
Lactate	C3	128[74]
Glucose	C1α	169[80]
	C1β	162[80]

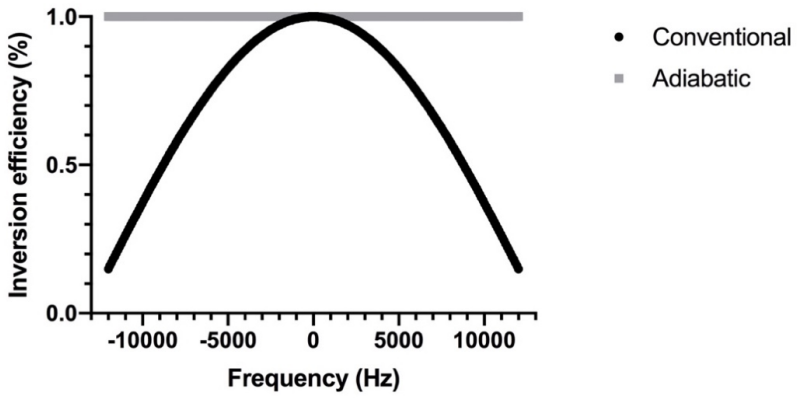

Figure 2.15. Inversion efficiency of conventional 180° pulses and adiabatic pulses. Intensity profile of HSQC acquired using (black) conventional 180° pulses shows reduced inversion efficiency for peaks further away from the frequency offset and (grey) adiabatic CHIRP pulses have consistent intensities within a typical ^{1}H sweep width of 6 ppm (4800 Hz at 800 MHz) and ^{13}C sweep width of 100 ppm (20,000 Hz at 800 MHz).

from the proton to carbon nuclei (**Figure 2.15**), (2) the SNR is lower than other HSQC sequences since the z-filter removes half the spins (antiecho), and (3) it has a long acquisition time due to the high resolution (<3 Hz for glutamate C2 isotopomers) and large ^{13}C spectral width required to detect and resolve ^{13}C multiplets for isotopomer analysis.

Here several HSQC sequences were compared to optimize SNR and minimize scan time (**Figure 2.16**). First, adiabatic inversion pulses allow for uniform transfer of magnetization across the sweep width, resulting in improved SNR for peaks such as lactate (58% higher lactate SNR) that are located further from the frequency offset compared to the conventional inversion pulse. Second, echo-antiecho gradient selection, which refocuses the antiecho spins, resulted in a two-fold boost in SNR for lactate (210% higher lactate SNR) compared to using a conventional z-filter gradient, which purges the antiecho spins. Though faster than traditional ^{13}C NMR, 2D NMR is still limited by its long acquisition time which makes it difficult to analyze large quantities of samples. Non-uniform sampling (NUS) was evaluated since NUS acquisition and processing is widely implemented in vendor-supplied software and easy to customize. While the

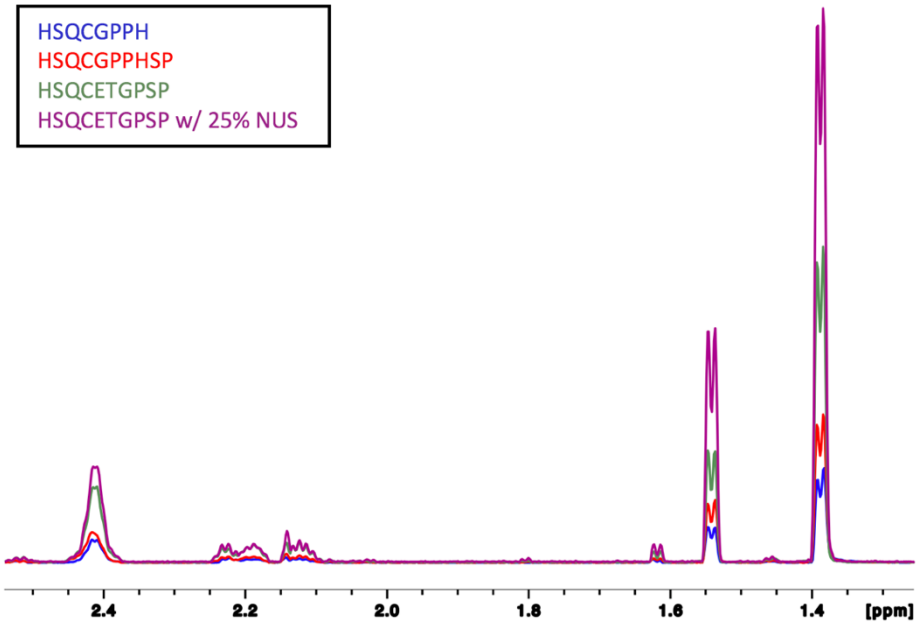

Figure 2.16. 1D projections of ^{1}H-^{13}C HSQC pulse sequences. Comparison of positive projection of all 2048 rows of phase-sensitive, gradient-enhanced HSQC acquisition with a JXH of 135 Hz (based on an average JCH of 127, 130, and 145 Hz for glutamate C2, C3, and C4, respectively) using (blue) HSQCGPPH (z-filter and selection before t1), (red) HSQCGPPHSP (z-filter and selection before t1, and adiabatic pulses for inversion), (green) HSQCETGPSP (echo-antiecho with adiabatic pulses for inversion), and (purple) HSQCETGPSP with 25% Non-Uniform Sampling (NUS) of a [U-^{13}C]glucose-labeled PC-3 cell extract.

SNR of HSQC acquired with NUS is not directly comparable with conventional HSQC, HSQC acquired with 25% sparsity resulted in enhanced sensitivity (175% increase in lactate SNR) with the same scan time. While NUS may be useful for other metabolomic applications, it is unsuitable for ^{13}C isotopomer analysis which requires high resolution in the indirect dimension to resolve ^{13}C isotopomer patterns. Together, implementation of these pulse parameters greatly improved sensitivity and throughput of 2D HSQC for metabolomic studies.

Traditionally, quantification of 2D HSQC peak volumes has relied on analytical approaches that require a reference standard and calibration using metabolite standards of known concentrations[74,81]. Standardless methods such as the ERETIC can also be used for 2D NMR[82].

Table 2.4. Comparison of ^{13}C-metabolite quantification using 1D ^{1}H with presaturation versus 2D ^{1}H-^{13}C HSQC.

	Concentration (nmol/million cells)	
	^{1}H	^{1}H-^{13}C HSQC
^{13}C-Aspartate	0.29	.306
^{13}C-Glutamate	4.86	4.92
^{13}C-Lactate	8.00	8.10

Several acquisition approaches such as quantitative HSQC (Q-HSQC)[83], quick quantitative HSQC (QQ-HSQC)[84], quantitative offset-compensated CPMG-adjusted HSQC (Q-OCCAHSQC)[85], extrapolated time-zero HSQC ($HSQC_0$)[86], and perfect-HSQC[87] have been proposed for highly accurate quantification of metabolite concentrations using 2D HSQC. Here, an analytical approach was used to quantify ^{13}C-labeled metabolites from 2D HSQC with [2-^{13}C]glycine as an internal reference standard. Peak volumes were corrected for JCH filtering, inversion efficiency, and number of equivalent protons, using **Equation 2.3,** adapted from Heikkinen et al. (2003)[83]:

$$Moles_{Met} = \frac{Vol_{Met}}{Vol_{Ref}} * \frac{N_{1H,Ref}}{N_{1H,Met}} * \frac{1}{\sin^2\left(\frac{\pi J_{CH,Met}}{2J_{CH,HSQC}}\right)} * \frac{1}{(IE_{\nu,Met})^2} * Moles_{Ref} \quad \textbf{(Equation 2.3)}$$

where Vol_{Met} and Vol_{Ref} are the peak volumes in the HSQC spectrum for the metabolite of interest (Met) and the reference (Ref), respectively; $N_{1H,Met}$ and $N_{1H,ref}$ are the number of equivalent protons for Met and Ref; $J_{CH,Met}$ and $J_{CH,HSQC}$ are the J-coupling in hertz for Met and for the HSQC experiment; $IE_{\nu,Met}$ is the inversion efficiency of at the resonance frequency (ν) of Met.

The enhanced sensitivity and resolution of 2D ^{1}H-^{13}C HSQC enables quantification of ^{13}C-metabolite concentrations of mass-limited samples. Experimentally, conventional ^{1}H-^{13}C HSQC (hsqcgpph) had a sensitivity gain of 24-fold (theoretical $(\gamma_{1H}/\gamma_{13C})^{5/2}$ = 32-fold sensitivity gain) compared to conventional ^{13}C direct detection. ^{13}C glutamate isotopomers were resolvable

using both direct detect ^{13}C (**Figure 2.11**) and ^{1}H-^{13}C HSQC with no ^{13}C decoupling during acquisition (**Figure 2.14**). Quantification using 2D ^{1}H-^{13}C HSQC produced similar concentrations of ^{13}C-aspartate, ^{13}C-glutamate, and ^{13}C-lactate as quantification using 1D ^{1}H presaturation with and without ^{13}C-decoupling (**Table 2.4**).

2.5. NMR-based ^{13}C isotopomer analysis

Isotopomer analysis can measure flux through intricate pathways such as the TCA cycle, which can give complex isotopomer patterns due to substrate recycling and multiple entry points[88,89]. Several ^{13}C isotopomer models exist, including TCACALC[88,90,91], 13CFLUX2[92], INCA[93], FiatFlux[94], NMR2Flux+[95], Metran[96], and OpenFlux[97]. As seen in **Table 2.5**, the isotopomer models that have been developed are diverse, encompassing various types of mathematical models, programming languages, statistics, and biological models. Some models such as tcaCALC[90] and 13CFLUX[98] solve the isotopomer balance equations using individual isotopomers. However, it can be difficult to solve the nonlinear isotopomer balance equations using this method if a large number of isotopomers and metabolic pathways are being studied. To address this, several methods have been used to reduce the number of variables, including cumomers[99], bondomers[95], and elementary metabolite units (EMU)[100]. This makes the isotopomer analysis heavily dependent on the model and makes it difficult to validate multiple models or adapt models to include new pathways such as glutaminolysis.

In this dissertation, ^{13}C isotopomer analysis was performed using TCACALC, which uses algebraic equations to describe the ^{13}C isotopomer patterns based on the metabolic (pathway map) and experimental (FE of the ^{13}C tracer and relative isotopomer areas) parameters. This model was originally validated for liver and cardiac metabolism, so the assumptions and allowed pathways in the model must be carefully considered when using it for cancer metabolism.

Table 2.5. Existing ^{13}C isotopomer models for NMR and MS. GC=gas chromatography, EMU=elementary metabolite

Isotopomer Model	Program	Modality	Isotopomer Balancing Technique	Optimization Algorithm	Statistical Method	Biological model?	Customizable model?
tcaCALC	DOS	NMR, MS	Isotopomer	Nonlinear-Least Squares	One-way ANOVA, Monte Carlo simulation	Mammalian (Liver, Cardiac, Muscle)	No
13CFLUX2	C++, Java, Python	NMR, GC/MS	Cumomer, EMU	Sequential quadratic programming, nonlinear programming	Linearized statistics, Bootstrap Monte Carlo simulations	Micro-organisms (Bacteria, Yeast), Plant embryos, Mammalian (Cancer, Immune cells)	Yes
FiatFlux	Matlab	GC/MS	Algebraic equations	Nonlinear Least Squares	Experimental error from the Jacobian matrix of the output function	Micro-organism (Bacteria, Yeast)	No
NMR2Flux+	C	NMR	Cumomer, Bondomer	Simulated annealing	Bootstrap Monte Carlo simulations	Plant embryos	Yes
Metran	Matlab	MS	EMU	sequential quadratic programming	Custom model	Mammalian (Cancer, Liver, Immune cells), Micro-organisms (Bacteria, Yeast)	Yes
OpenFLUX	Matlab	NMR, MS	EMU	Matlab toolbox	Same model as Metran	Micro-organisms (Bacteria, Yeast)	Yes

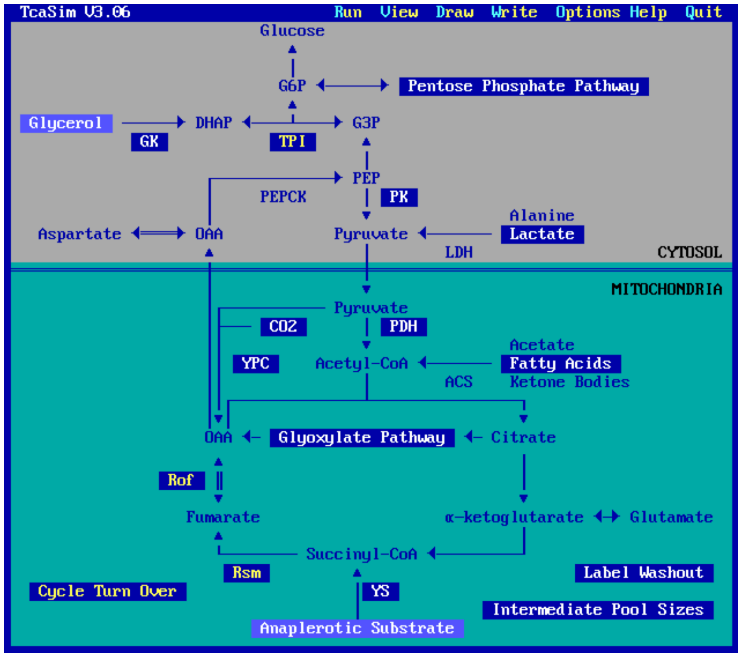

Figure 2.17. TCACALC GUI interface

As seen in **Figure 2.17**, glucose can only be used as an output variable since gluconeogenesis of glycogen or lactate is a key pathway in liver metabolism. Therefore, for ^{13}C-glucose labeling studies, the ^{13}C-glucose tracer entered via the "lactate" input variable in the model. The model that gave the best fit to the experimental isotopomer data was calculated based on (1) experimentally-derived relative isotopomer ratios of glutamate C2, C3, and C4 quantified using high-resolution 2D ^{1}H-^{13}C HSQC, (2) relative fluxes through PDH, (3) anaplerosis leading to succinyl-CoA relative to citrate synthase (YS)[101,102], (4) enrichments of the ^{13}C-glucose tracer, (5) unlabeled "fatty acids" to represent all metabolites that convert to acetyl-CoA other than glucose (such as acetate and other ketone bodies), and (6) unlabeled "anaplerotic substrate".

To validate the model, the metrics that must be assessed include: (1) statistical fit of individual parameters, (2) statistical fit of the overall pathway model, and (3) the measured and simulated relative isotopomer areas should not be significantly different from each other. The most basic pathway should be modeled first, and additional pathways can then be added

iteratively. Additional pathways should only be kept in the model if the model fit improves significantly.

2.6. Oxygen consumption rate of cells and tissues

Oxygen consumption is an important marker of energy metabolism and indirectly assesses mitochondrial oxidative phosphorylation function and activity. While the TCA cycle does not directly require oxygen, it does rely on byproducts of the electron transport chain, which requires oxygen. Therefore, for ^{13}C isotopomer studies, oxygen consumption is required to calculate absolute pathway flux and determine how many turns of the TCA cycle were completed during the ^{13}C-labeling timeframe. In this section, three different systems are described: a custom in-house bioreactor adapted from previously published setups[103-106] and equipped with a fluorescence-based fiber optics oxygen sensor (Ocean Optics), a Clark-type oxygen electrode Oxygraph+ (Hansatech Instruments), and the Seahorse XFe24 Extracellular Flux Analyzer (Agilent).

The fluorescence-based fiber optics oxygen sensor can measure the partial pressure of dissolved or gaseous oxygen in gas or aqueous solutions continuously without consuming oxygen. It is insensitive to changes caused by pH, ionic strength, and salinity, making it ideal for measuring oxygen in cell culture growth media. However, this system is sensitive to temperature fluctuations and requires time (>30 min) to reach equilibrium. To use this system, cells must be electrostatically encapsulated in 3.5% alginate microspheres (300-450 uL diameter) at a density of 100 million cells/mL into a 150 mM $CaCl_2$ bath as previously described[107]. The cell microspheres are then placed into the sample chamber of the bioreactor and oxygen consumption rates are measured by the fiber optics oxygen sensor as depicted in **Figure 2.18**.

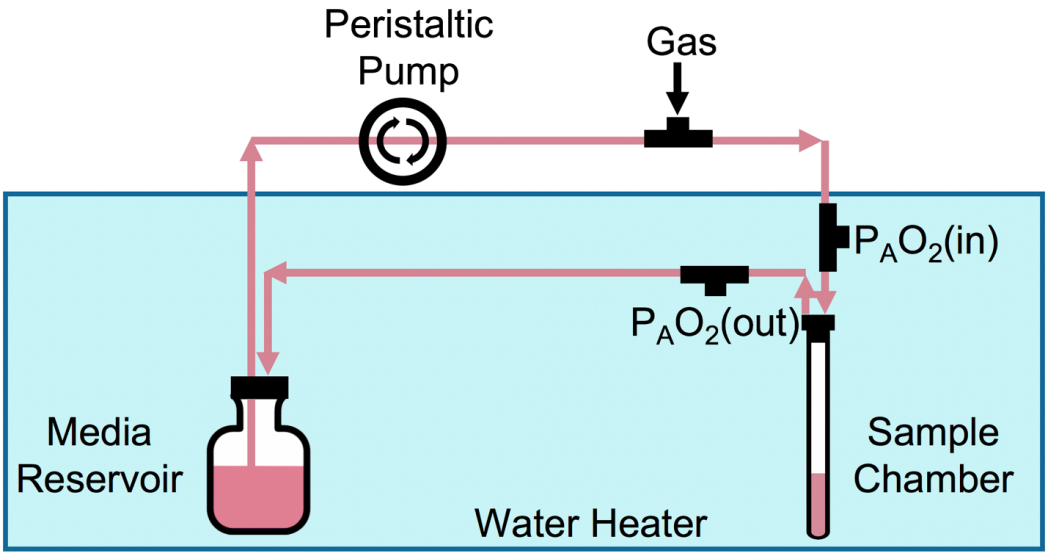

Figure 2.18. Bioreactor schematic for oxygen consumption rate measurements of living cells and tissue in real time. P_AO_2(in) and P_AO_2(out) indicate measurements of partial pressure of dissolved oxygen.

A flow rate of 0.25 mL/min gave the highest oxygen consumption rate (OCR) for cells encapsulated in alginate (not shown), which indicates that this flow rate may be optimal for cell viability and maintenance of representative metabolic activity.

A Clark-type oxygen electrode is the traditional method to measure oxygen. These systems are sealed during the measurement of OCR so that the decay of oxygen within the chamber is directly related to biological oxygen consumption. Cheap and easy-to-use, the Oxygraph+ allows OCR of cells and tissues to be measured in any growth medium and only requires small amounts of specimen to obtain robust, reproducible results. Cells can be loaded into the sample chamber within the Oxygraph+ in suspension. While sensitive, the Oxygraph+ system can only measure one sample at a time. Furthermore the electrode itself consumes a small amount of oxygen during the measurement, so it is critical to measure the background OCR particularly for mass-limited samples with low OCR.

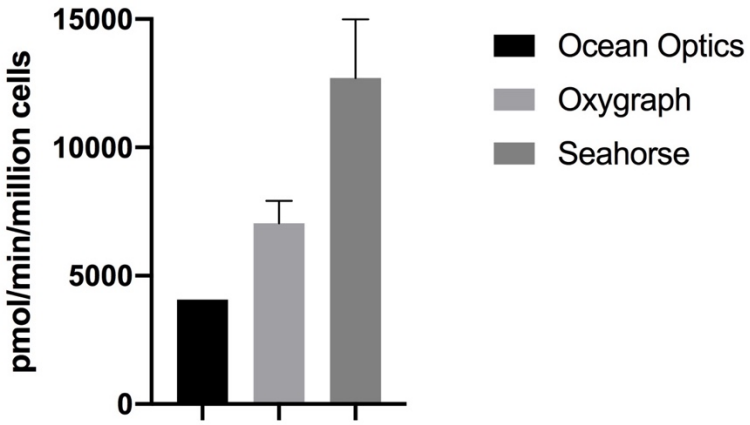

Figure 2.19. Oxygen consumption rate measurements using fiber optics oxygen sensors, Oxygraph+, and Seahorse XFe24. LNCaP oxygen consumption rate was measured using a homebuilt bioreactor system equipped with a fiber optics oxygen sensor (n=1), Oxygraph+ (n=3), and the Seahorse XFe24 Extracellular Flux Analyzer (n=17).

The Seahorse XFe24 Extracellular Flux Analyzer is a sensitive, high-throughput system that can simultaneously measure OCR and extracellular pH to assess metabolic perturbations. This system has a semi-closed design such that the sample chamber is temporarily sealed during the OCR measurement. However, oxygen can slowly diffuse into the sample chamber during the OCR measurement since the sample chamber is not tightly sealed off from the rest of the fluid space and the plate material is not impervious to oxygen[108]. In order to assess OCR, cells must remain adhered to the microplate throughout the entire study. Due to the weak adherence of LNCaP cells, which were easily dislodged by turbulence from gentle pipetting and mixing, several adherence substrates were tested, including Cell-Tak, 10 ug/mL fibronectin, 10 ug/mL collagen, combination of fibronectin and collagen at 10 ug/mL each, and 50 mg/mL 3,4-dihydroxy-L-phenylalanine (L-DOPA). While the Seahorse manual recommends Cell-Tak to improve adherence, it did not improve adherence for LNCaP cells. The L-DOPA coating was the only method that resulted in robust adherence and allowed cells to withstand gentle pipetting and mixing throughout the Seahorse protocol.

Here the OCR of LNCaP cells was measured using the fluorescence-based fiber optics oxygen sensor, Oxygraph+, and Seahorse XFe24 (**Figure 2.19**). The variability in OCR provided by each system may be due to the sensitivity of each technique, the growth phase of the cells during assessment, and the solvent volume in the sample chamber. The low OCR measurement from the fiber optics oxygen sensors may be due to the large solvent volume (~5-10 mL between sensors) within the bioreactor. The encapsulation of the cells in alginate microspheres may also affect perfusion of nutrients and oxygen. Furthermore, the fiber optics bioreactor setup requires a long time to reach temperature equilibrium, making it unreasonable to compare its OCR measurement to the Oxygraph or Seahorse which are closed systems that can measure OCR within seconds to minutes of sealing off the sample chamber. For the Seahorse measurement, cells were seeded 24 hours prior to the OCR measurement so it is possible that the higher OCR may be due to differences in cell survival and proliferation. The adherent state of the cells in the Seahorse assay may also contribute to metabolic differences compared to the other two techniques, which require the cells to be in suspension.

2.7. Hyperpolarized ^{13}C NMR and MRI of cell, tissue, and murine models

HP ^{13}C MRI is a new noninvasive molecular imaging technique that enables real-time surveillance of pathway-specific metabolic and physiologic processes that are central to a variety of diseases, including cancer, cardiovascular disease, and metabolic diseases of the liver and kidney[26,109]. This technique is currently undergoing clinical translation[26].

Hyperpolarization via dynamic nuclear polarization (DNP)[110], can be achieved via microwave irradiation of ^{13}C-labeled compounds with a radical at high-magnetic field strengths (3.35T - 5T) and cold temperatures (1 - 1.6°K). The resulting signal enhancement of >10,000-

fold enables noninvasive imaging of ^{13}C-labeled biomolecules that are endogenous, nontoxic, and nonradioactive. For biological and clinical studies, dissolution DNP (dDNP) is essential in order to adjust the hyperpolarized solution to physiological pH and temperature. The detected signal of downstream metabolites is dependent on several factors described in **Equation 2.4**[111]:

$$Signal = \%\ Polarization \times Pool\ Size \times Fractional\ Enrichment \quad \textbf{(Equation 2.4)}$$

In addition to these parameters, the transport rate of the tracer also plays an important role in signal sensitivity. This is because HP ^{13}C is limited by the short T_1 of the ^{13}C nuclei, which ranges between 45-90 sec for carbonyl carbons (i.e., [1-^{13}C]pyruvate).

The simplest HP ^{13}C studies can be performed on cell slurries. Conventionally, cells are placed in cold phosphate-buffered saline (PBS) prior to the study, then immediately placed into an NMR spectrometer upon injection of HP solution. However this method suppressed that cellular metabolism of HP [1-^{13}C]pyruvate since cells are metabolically inactive at 4°C and PBS is nutrient-free. To study biologically-relevant metabolism of HP ^{13}C pyruvate, cells were resuspended in cold serum-free DMEM medium and then warmed to 37°C during the dissolution step (~1-2 min) prior to injection of the HP solution and subsequent data acquisition. This allowed cells to recover to a metabolically active state in nutrient-rich medium.

A more clinically-relevant method to assess metabolism of cells or tissues is the use of an NMR-compatible bioreactor that maintains physiologically-relevant conditions by circulating medium at 37°C with 95%air/5%CO_2 using a gas exchanger[103,107,112-115]. The advantage of bioreactors over slurries is better control over the effects of cell density, oxygen, temperature, and flow rate (i.e., delivery of the HP ^{13}C probe) that may otherwise complicate the observed metabolic activity. For cell-based bioreactor studies, cells must be immobilized in 3D-substrates to prevent them from flowing out of the sensitive region of the NMR probe. This can be done via

electrostatic encapsulation in alginate or conjugation to polystyrene beads. Similarly, tissue slices also need to be immobilized using 3D-printed scaffolds. ^{13}C data is acquired using 1D ^{13}C NMR. Use of an NMR-compatible bioreactor for HP ^{13}C studies of PDX-derived RCC tissue will be discussed in Chapter 5.

Finally, *in vivo* HP ^{13}C MRI studies can be performed on animal models. In these models, HP solution is injected via tail vein catheter into anesthetized mice and the HP probe and its metabolites can be observed via spectroscopic or frequency-specific imaging approaches[109,116]. Several imaging sequences have been developed such as 1D slice-selective spectroscopy[117-119], 2D CSI[120], 3D GRASE[121,122], echo-planar spectroscopic imaging[123-125], echo planar imaging[121,126], compressed sensing[24], steady-state free procession[127,128], and spiral imaging with real-time calibration[129] to provide sufficient spatial resolution and coverage, and temporal resolution for *in vivo* metabolic flux measurements.

CHAPTER THREE

Resistance to Androgen Deprivation Therapy Leads to Altered Metabolism in Human Prostate Cancer Cell and Murine Models

3.1. Abstract

Androgen deprivation therapy (ADT) is the cornerstone of treatment for patients with advanced prostate cancer. However, almost all patients will eventually stop responding to ADT and develop castration-resistant prostate cancer (CRPC). Currently there are no clinical or imaging methods that can reliably predict the development of CRPC. Hyperpolarized (HP) ^{13}C magnetic resonance imaging (MRI) is a new metabolic imaging method that could provide a non-invasive means to image the emergence of CRPC based on early metabolic changes. In this study, 1D and 2D high-field NMR metabolomic approaches were used to determine the metabolic flux of [U-^{13}C]glucose and [U-^{13}C]glutamine through glycolysis, tricarboxylic acid (TCA) cycle, glutaminolysis, and glutathione synthesis, initially using human prostate cancer cell lines that are androgen-dependent (LNCaP) and castration-resistant (PC-3), and then using the TRAMP murine model in order to establish the metabolic phenotype of CRPC. Steady-state metabolite concentrations and fractional enrichment measurements demonstrated that CRPC was associated with upregulation of glycolysis, TCA metabolism of pyruvate and glutamine, glutaminolysis, and glutathione synthesis in castration-resistant PC-3 cells and in treatment-driven CRPC TRAMP tumors. These findings are further supported by (1) ^{13}C isotopomer modeling using TCACALC showing increased flux through pyruvate dehydrogenase (PDH) and anaplerosis, (2) enzymatic assays showing increased lactate dehydrogenase (LDH) activity, PDH activity, and glutaminase (GLS) activity, (3) oxygen consumption measurements showing increased dependence on anaplerotic fuel sources for mitochondrial respiration correlating with resistance to catration, and (4) gene set enrichment analysis of glycolysis, oxidative phosphorylation (OXPHOS), and lipid synthesis. These results support the use of hyperpolarized [1-^{13}C]pyruvate to assess glycolysis, [2-^{13}C]pyruvate to assess TCA metabolism, [5-

^{13}C]glutamine to assess glutaminolysis, and [1-^{13}C]dehydroascorbate to assess glutathione redox potential as non-invasive imaging biomarkers of CRPC in future *in vivo* studies.

3.2. Introduction

Primary androgen deprivation therapy (ADT), which lowers serum testosterone to castration level, is the cornerstone of treatment for patients with advanced recurrent or metastatic prostate cancer. However, almost all patients will eventually stop responding to androgen deprivation and develop castration-resistant prostate cancer (CRPC)[27]. Clinical diagnosis of CRPC is based on a significant increase in tumor burden or metastasis detected using CT or MRI and/or rising serum prostate-specific antigen (PSA) levels[130]. Advances in the understanding of the biology of CRPC have led to the development of new second-line androgen pathway inhibitors (API), enzalutamide, apalutamide and abiraterone, that bind to androgen receptor (AR) with much higher affinity than the clinically used first-line antiandrogens, such as bicalutamide, thereby effectively retarding the growth of CRPC[30]. Once a patient develops CRPC, the current sequence of treatment is to start with an API and move to chemotherapy, which is often combined with a targeted biologic agent[27]. Currently no reliable clinical or non-invasive imaging methods can predict the development of CRPC, which is critical in guiding treatment decisions in men with advanced prostate cancer.

Hyperpolarized ^{13}C MRI (HP ^{13}C MRI) is a powerful new metabolic imaging method that can be used to image metabolic fluxes through key pathways associated with cancer progression and therapeutic response in patients[125]. Genomic analysis of prostate cancer cell lines has shown that the AR is still active in CRPC[131,132] despite castration levels of testosterone and that its binding profile changes with disease progression to CRPC[133]. Expression of AR-regulated genes

such as those involved in glucose uptake and glycolysis, glutaminolysis, and anabolic metabolism have been shown to be altered in CRPC[133,134]. Furthermore, AR binding sites found only in CRPC tissue were enriched for MYC[133], which has been shown to regulate glycolysis and glutaminolysis[135]. Together these findings suggest that glucose and glutamine metabolism should be altered in CRPC. Previous preclinical HP ^{13}C MRI studies have shown that glycolytic activity, as measured by the pyruvate-to-lactate ratio and the rate of conversion of ^{13}C pyruvate to ^{13}C lactate (k_{pl}), increases as prostate tumors become more aggressive[21,24]. Additionally, a patient study demonstrated an early reduction in k_{PL} after effective ADT[25]. While initial preclinical and patient studies focused on using [1-^{13}C]pyruvate to investigate changes in glycolysis, HP probes that provide insight into other metabolic pathways, such as [2-^{13}C]pyruvate, [5-^{13}C]glutamine, and [1-^{13}C]dehydroascorbate, are being investigated and clinical translation of these probes is in progress. However, to date, the metabolic phenotype of CRPC has not been fully defined.

To determine the metabolic phenotype of CRPC, an appropriate model must be used. *In vitro* models are useful for identifying the predictors of treatment response and resistance due to their fast growth rate and robustness. The most commonly studied prostate cancer cell lines are the androgen-dependent LNCaP[136] and castration-resistant PC-3[137]. Here, LNCaP and PC-3 cells were used to optimize experimental parameters and fully characterize the metabolic alterations associated with resistance to castration.

Although cell lines are easy to grow and study, they lack the cellular heterogeneity observed in patient tumors and often do not fully reflect human disease. The development and progression of the transgenic adenocarcinoma of the mouse prostate (TRAMP) model from an androgen-dependent to castration-resistant state closely mimics disease pathogenesis and metabolism observed in patients[138-141]Similar to human prostate cancer, TRAMP tumors are

initially androgen-dependent and progress to CRPC upon resistance to orchiectomy, which is equivalent to chemically-induced primary ADT used in the clinic[142,143]. These features make TRAMP an ideal model to use for this study.

3.3. Materials and Methods

Cell Culture and ^{13}C-labeling

LNCaP (clone FGC, ATCC CRL-1740) and PC-3 (ATCC CRL-1435) cells were obtained from American Type Culture Collection (ATCC) and grown to 70-80% confluency in a 37°C incubator with 95% air/5% CO_2. For steady-state metabolism studies, LNCaP cells were cultured in RPMI-1640 medium supplemented with 10% fetal bovine serum (FBS) and 1% penicillin-streptomycin for 6 hours, and PC-3 cells were cultured in Ham's F-12K medium supplemented with 10% FBS and 1% penicillin-streptomycin for 6 hours. For ^{13}C-glucose labeling studies, media was replaced with RPMI supplemented with 25 mM [U-^{13}C]glucose, 10 mM glutamine, 10% FBS, and 1% penicillin-streptomycin for 6 hours. For ^{13}C-glutamine labeling studies, media was replaced with RPMI supplemented with 10 mM [U-^{13}C]glutamine, 25 mM glucose, 10% FBS, and 1% penicillin-streptomycin for 24 hours. Cultured media was collected after labeling was completed in order to quantify glucose consumption rate, glutamine consumption rate, and lactate export rate.

Treatment of TRAMP Mice

Adult male transgenic adenocarcinoma of the mouse prostate (TRAMP) mice were obtained from Roswell Park Cancer Institute. Mice with a solid tumor mass between 0.1 – 1 cc underwent orchiectomy. Mice with <25% increase in tumor volume one-week post-orchiectomy

were defined as androgen-dependent prostate cancer (ADPC), and mice with ≥25% increase in tumor volume were defined as CRPC. An additional cohort of CRPC TRAMP that underwent daily treatment with apalutamide (ARN-509) at 30 mg/kg/day administered via oral gavage[144] for seven days were defined as CRPC+ARN. Tumor volume was monitored using T_2-weighted spin echo MRI prior to orchiectomy, one-week post-orchiectomy, and one-week post-ARN-509.

^{13}C Labeling of TRAMP Mice

Either 80 µL of 25%wt/vol [U-^{13}C]glucose or 200 µL of 35.73 mg/mL [U-^{13}C]glutamine were injected in the tail vein every 15 minutes for a total labeling time of 45 minutes[49]. To minimize the effects of stress and anesthesia on metabolism, mice were briefly anesthetized using isoflurane for 2-3 minutes to perform ^{13}C-injection, then allowed to wake in between injections. Tissue was collected immediately upon euthanasia and flash-frozen in liquid nitrogen for metabolomic analysis.

Extraction of Prostate Cells

Prior to extraction, cells were rinsed with cold PBS. Cellular metabolism was quenched by direct addition of cold methanol, and intracellular metabolites were extracted using cold 1:1:1 methanol:water:chloroform[68]. The aqueous fraction was isolated, lyophilized, and resuspended in 600 µL D_2O with TSP for NMR analysis. The lipid fraction was isolated, evaporated and resuspended in 400 µL of a 2:1 mixture of $CDCl_3$ and 40 mM methanolic Cs-EDTA (200 mM EDTA in D_2O adjusted to pH 6.0 with CsOH, and further diluted five-fold with MeOH-d_3)[70]. For lipid samples, an external standard of TSP in D_2O in a 1.5 mm NMR tube was used for quantification.

Extraction of TRAMP Tumors

Frozen tissue was homogenized using a Tissuelyser LT in 400 µL cold methanol at 4°C. Intracellular metabolites were extracted using cold 1:1:1 methanol:water:chloroform[68]. The aqueous fraction was isolated, lyophilized, and resuspended in 400 µL D_2O for NMR analysis. For aqueous samples, an external standard of TSP and [2-^{13}C]glycine in a 1.5 mm NMR tube was used for quantification.

NMR Acquisition

NMR spectra were acquired on an 800 MHz Bruker AvanceI equipped with a 5 mm triple resonance TXI cryoprobe. *^{13}C-decoupled ^{1}H water presaturation*: α=90, TD=24k, SW=15 ppm, TR=12 seconds, AQ=0.5 seconds, NS=32. Solvent signal was suppressed using a presaturation pulse. Adiabatic decoupling was applied during acquisition using a CHIRP pulse with 54 kHz sweep width (equivalent to 200 ppm @ 800 MHz), and shaped pulse power level of +2 dB with respect to the power level determined for ^{13}C-GARP. Total scan time was 6 minutes. *^{1}H-^{1}H TOCSY*: 2D TOCSY with water presaturation was used with the following parameters: TD=4096x512, SW=12x12 ppm, TR=2 seconds, AQ=0.239 seconds, NS=8, t_{mix}=60 milliseconds. Total scan time was 2 hours and 45 minutes. Data was zero-filled in both dimensions to a final digital resolution of 9.4 Hz/point in the F2 dimension. *^{1}H-^{13}C HSQC*: A phase-sensitive 2D HSQC (hsqcgpph) with no ^{13}C decoupling during acquisition was used with the following parameters: TD=2048x4096, SW=6x120 ppm, TR=1.5 seconds, AQ = 0.297 seconds, NS=2, J_{CH} = 135 Hz (average J_{CH} of 127, 130, and 145 Hz for glutamate C2, C3, and

C4). Data was zero-filled in both dimensions to a final digital resolution of 2.9 Hz/point in the F2 dimension. Total scan time was 4 hours.

NMR Quantification

1D NMR datasets were processed using ACD/1D NMR Processor (version 9). The 1D datasets were zero-padded by a factor of 2, apodized with a 0.5 Hz exponential filter, and manually phased and baseline corrected. Peaks of interest were automatically fit using a Lorentzian-Gaussian shape function. 2D NMR datasets were processed using TopSpin (version 3.5). 2D datasets were zero-padded by a factor of 2, manually phased, and peak volumes were integrated.

For cells, intracellular and extracellular metabolite concentrations were quantified from ^{1}H water presaturation 1D spectra of unlabeled cell extracts and media respectively. For tissues, total metabolite concentrations were quantified from ^{13}C-decoupled ^{1}H water presaturation 1D spectra of ^{13}C-labeled tissue extracts.

Fractional enrichment (FE) was quantified as [^{13}C-labeled metabolite]$_{HSQC}$/[total metabolite]$_{\{13C\}1H}$. Total metabolite concentration for all other metabolites was quantified using ^{13}C-decoupled ^{1}H spectra by manually fitting peaks of interest using a Lorentzian-Gaussian shape. The concentration of ^{13}C-labeled metabolites was quantified using ^{1}H-^{13}C HSQC by integrating the volumes of the cross-peaks and correcting for polarization transfer efficiency using **Equation 2.3** as previously described in Chapter 2. Glutathione FE from [U-^{13}C]glutamine labeling studies was quantified using ^{1}H-^{1}H TOCSY by integrating the peak volumes of the ^{13}C-satellites and the central unlabeled peak.

^{13}C Isotopomer modeling

For [U-^{13}C]glucose-labeled cell extracts, relative peak volumes of glutamate C3 and glutamate C4 isotopomer multiplets were quantified from high resolution 2D ^{1}H-^{13}C HSQC spectra using Topspin (version 4.0.6). Glutamate C2 was not included since it has the lowest SNR and its doublets (2D12 and 2D23) were not fully resolved. Data was then analyzed using TCACALC[90,145,146]. Parameters examined include relative fluxes through glycolysis (LDH), pyruvate dehydrogenase (PDH), pyruvate carboxylase (YPC), acetyl-CoA synthase (ACS), and anaplerosis leading to succinyl-CoA relative to citrate synthase (YS). The model that gave the best fit to our NMR data included the following parameters: LDH, PDH, YS, isotopic enrichment of the ^{13}C-tracer, unlabeled "fatty acids" pool to represent all metabolites that convert to acetyl-CoA other than glucose (such as acetate and other ketone bodies), and unlabeled "anaplerotic substrate". The isotopomer model was validated using the following metrics: (1) statistical fit of individual parameters, (2) statistical fit of the overall pathway model, and (3) comparison of measured and simulated relative isotopomer areas.

LDH Activity Assay

Cells and tissues were homogenized using a Tissuelyser LT in cell lysis buffer (Cell Signaling). LDH activity of cell and tissue lysates was measured spectrophotometrically by quantifying the linear decrease in NADH absorbance at varying pyruvate concentrations at 339 nm using a microplate reader. The maximum velocity (v_{max}) and the Michaelis–Menten constant (K_m) were estimated using the Lineweaver–Burk plot.

PDH Activity Assay

PDH activity of cell and tissue lysates was measured spectrophotometrically using the PDH enzyme activity microplate assay kit (Abcam) according to manufacturer's instructions. In brief, cells and tissues were homogenized using a Dounce homogenizer in PBS containing protease inhibitor cocktail (Abcam) and 20 mM NaF to preserve endogenous PDH phosphorylation state and activity. PDH enzyme was immunocaptured in the microplate supplied by the kit, and activity was determined by quantifying the reduced reporter dye at 450 nm using a microplate reader.

GLS Activity Assay

GLS activity of cell lysates was measured fluorometrically using the PicoProbe^{TM} glutaminase activity assay kit (Biovision) according to manufacturer's instructions. In brief, cells were homogenized using a Tissuelyser LT in lysis buffer provided by the kit. GLS activity was determined by fluorometrically at Ex/Em 535nm/587nm with a glutamic acid standard curve using a microplate reader.

ATP Quantification

ATP content of cell lysates was measured using the CellTiter-Glo® luminescent cell viability assay kit (Promega) according to manufacturer's instructions. Luminescence of the luciferase reaction with ATP was measured using a luminometer.

NAD/NADH Assay

NAD/NADH ratio of cell lysates was measured spectrophotometrically using the NAD/NADH assay kit (Biovision) according to manufacturer's instructions. Cells were homogenized in lysis buffer provided by the kit using a Tissuelyser LT. NAD, NADH, and their ratio were determined by measuring the reaction of reporter dye with NADH at 450 nm using a microplate reader.

NADP/NADPH Assay

NADP/NADPH ratio of cell lysates was measured spectrophotometrically using the NADP/NADPH assay kit (Abcam) according to manufacturer's instructions. Cells were homogenized using a Tissuelyser LT in lysis buffer provided by the kit. NADP, NADPH, and their ratio were determined by monitoring NADP formation fluorometrically at Ex/Em 540nm/590nm using a microplate reader.

Glutathione Assay

Reduced glutathione (GSH) and total glutathione of cell lysates were measured spectrophotometrically using the glutathione colorimetric assay kit (Biovision) according to manufacturer's instructions. Cells were lysed in buffer provided by the kit. GSH, total glutathione, and their ratio were determined by measuring reaction of reporter dye with GSH at 405 nm using a microplate reader.

Oxygen Consumption

Basal oxygen consumption rate (OCR) was measured using a Clark-type O_2 electrode (Oxygraph+, Hansatech Instruments). Cells or tissue were placed in a chamber with 1 mL serum-free DMEM medium at 37°C and respiration was assessed over 1 minute. Control traces using medium alone were acquired after each sample to assess oxygen consumption attributed by the electrochemistry of the Clark electrode.

Seahorse Analysis

OCR was measured using a Seahorse XFe24 Extracellular Flux Analyzer. Cells were seeded in Seahorse XFe24 microplates at ~60k cells/well and incubated overnight. Medium was then replaced with Seahorse XF Assay Medium, and cells were incubated in a CO_2-free incubator at 37°C for 1 hour prior to loading into the XFe24. The measurement protocol consisted of 3 minutes mix, 2 minutes wait, and 3 minute measurement cycles at 37°C, allowing for OCR measurements every 8 minutes. OCR measurements were normalized to protein concentration using the Bradford Assay. For the Mito Fuel Flex Kit, optimal concentrations of BPTES (3 μM), etomoxir (4 μM), and UK5099 (2 μM) were used.

Gene Set Enrichment Analysis

Raw RNA sequencing data (.fastq files) of LNCaP and PC-3 cells from GEO Accession GSE106305[147] were downloaded and aligned to the human reference genome (GRCh38.p12) using STAR v2.7.3. The, the DESeq2 R package was used to normalize read counts between samples and perform differential gene expression analysis between LNCaP and PC-3 cells. Ranked lists of genes that were enriched in either LNCaP cells or PC-3 cells were generated by

sorting the differential expression results by average log2foldchange. These ranked gene lists were imported into the gene set enrichment analysis (GSEA) software from the Broad Institute (version 4.0.1) and analyzed for Hallmark pathway gene set enrichment using the default settings (weighted enrichment statistic, 1000 permutations).

Statistics

Student's *t*-test was used to compare prostate cancer models using Prism version 8.3. For steady-state metabolite concentrations, statistical significance was corrected for multiple comparisons using the Holm-Sidak method. All statistics are reported as mean ± standard error. P values less than 0.05 (*p <0.05, **p <0.01 and ***p <0.001) were considered significant.

3.4. Results

The goal of this research was to metabolically assess the development of CRPC in order to identify hyperpolarized ^{13}C imaging probes that can be used to detect the presence of CRPC at an early time-point in order to better select subsequent treatment in individual patients. Two human prostate cancer cell lines, LNCaP (androgen-dependent) and PC-3 (androgen-independent), were studied to identify metabolic changes associated with resistance to castration. To accomplish this, NMR-based metabolomic approaches were used to determine the flux of [U-^{13}C]glucose and [U-^{13}C]glutamine through glycolysis, TCA cycle, glutaminolysis, and glutathione synthesis. Metabolic alterations associated with the development of CRPC were characterized initially using human prostate cancer cell lines that are androgen-dependent (LNCaP)[136] and androgen-independent (PC-3)[137], and then using a treatment-driven TRAMP model that is known to develop CRPC[138].

3.4.1. Glycolysis, TCA cycle metabolism, glutaminolysis and redox capacity is increased in PC-3 versus LNCaP cells

Representative 1D ^{1}H with water presaturation NMR spectra (**Figure 3.1A**) clearly highlight the differences arising from the ^{13}C flux of metabolites between the two human prostate cancer cell lines, LNCaP (androgen-dependent) and PC-3 (castration-resistant). Total metabolite concentrations and ^{13}C-labeled metabolite concentrations were quantified using ^{13}C-decoupled ^{1}H spectroscopy (**Figure 3.1B**) and 2D ^{1}H-^{13}C HSQC (**Figure 3.1C**), respectively. Glutathione FE was quantified using 2D ^{1}H-^{1}H TOCSY (**Figure 3.1D**). A combination of steady-state metabolite concentrations, fractional enrichment (FE), and enzymatic activity was used to assess metabolic fluxes through key pathways.

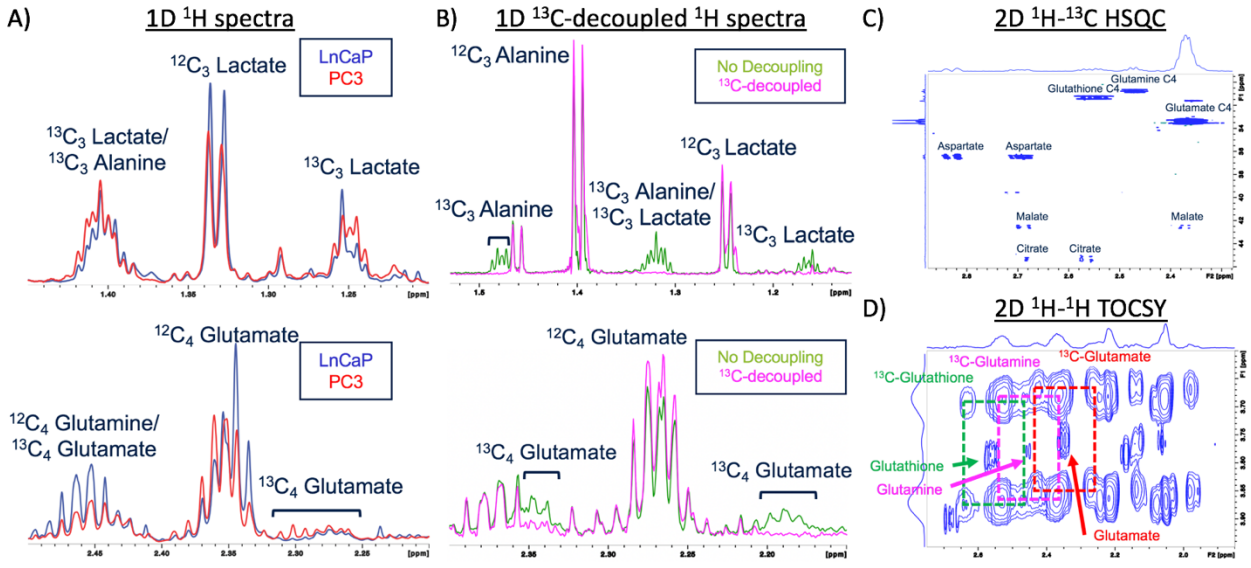

Figure 3.1. High-resolution NMR spectra of LNCaP and PC-3 cell extracts. (A) Comparison of lactate and glutamate regions using conventional 1D ^{1}H presaturation in extracts labeled with [U-^{13}C]glucose. (B) Comparison of lactate and glutamate regions using ^{1}H presaturation with and without ^{13}C-decoupling in extracts labeled with [U-^{13}C]glucose. (C) High resolution 2D ^{1}H-^{13}C HSQC of extracts labeled with [U-^{13}C]glucose for quantification of ^{13}C-labeled metabolites that are typically found in overcrowded ^{1}H regions, such as glutamate, glutamine, and glutathione, as well as low concentration metabolites such as aspartate and malate, and (D) 2D ^{1}H-^{1}H TOCSY of extracts labeled with [U-^{13}C]glutamine with unlabeled metabolite center peak and ^{13}C-satellites of glutamate, glutamine, and glutathione.

Table 3.1. Steady-state intracellular metabolite concentrations (nmol/million cells) of unlabeled LNCaP and PC-3 cell extracts (N=4).

	LNCaP			PC-3				
Metabolite	Average		SE	Average		SE	Raw p-value	Adjusted p-value
Acetate	7.6	±	1.2	4.1	±	1.4	0.1167	0.4377
Alanine	24.5	±	1.9	29.6	±	0.3	0.0365	0.2452
Aspartate	18.9	±	1.3	31.5	±	0.5	< 0.0001	**0.0016**
Choline	2.2	±	0.3	2.3	±	0.1	0.7080	0.9061
Citrate	22.3	±	1.0	3.5	±	0.2	< 0.0001	**< 0.0001**
Creatine	23.0	±	1.0	5.2	±	0.2	< 0.0001	**< 0.0001**
Creatine phosphate	31.5	±	1.9	7.3	±	0.4	< 0.0001	**0.0003**
Glucose	19.6	±	1.1	10.5	±	1.3	0.0021	**0.0234**
Glutamate	62.3	±	3.0	82.2	±	1.0	0.0007	**0.0105**
Glutamine	65.1	±	2.9	60.6	±	3.7	0.3760	0.7570
Glutathione	16.2	±	1.2	30.2	±	4.0	0.0155	0.1448
Glycine	31.7	±	2.0	16.0	±	5.3	0.0326	0.2452
Lactate	11.2	±	0.3	18.7	±	1.4	0.0017	**0.0203**
Phosphocholine	40.8	±	2.0	60.7	±	1.6	0.0002	**0.0030**
Pyruvate	3.1	±	0.1	2.3	±	0.4	0.0763	0.3789
Succinate	1.0	±	0.1	1.6	±	0.3	0.1087	0.4377
Threonine	7.8	±	0.4	6.9	±	2.1	0.6935	0.9061
myo-Inositol	11.7	±	1.9	84.8	±	1.1	< 0.0001	**< 0.0001**
Glycerophosphocholine	17.8	±	1.5	23.9	±	1.6	0.0307	0.2452
Total Choline*	60.8	±	3.2	86.9	±	3.0	0.0009	**0.0126**

*Total choline was defined as the summed concentrations of choline, phosphocholine, and glycerophosphocholine.

***Glycolysis*:** Glucose consumption was not significantly different between the two cell lines (**Figure 3.2A**). Steady-state metabolite concentrations indicated that PC-3 cells had a significantly higher lactate concentration (18.7±1.4 vs 11.2±0.3 mmol/million cells, N=4, $p<0.05$) (**Table 3.1**) and lactate efflux (197±20 vs 81±13 nmol/hr/million cells, N=4, $p<0.01$) (**Figure 3.2B**) compared to LNCaP cells. In [U-^{13}C]glucose labeling studies, PC-3 cells had

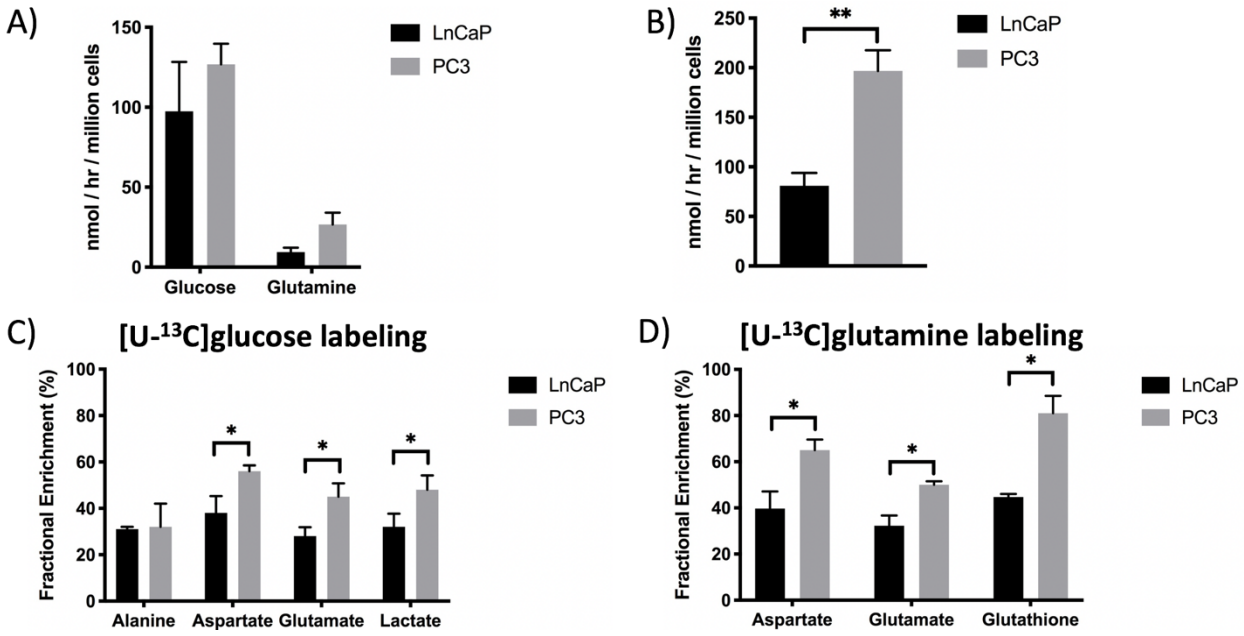

Figure 3.2. Metabolic comparison of LNCaP and PC-3 cells. (A) Steady-state consumption rates of [U-^{13}C]glucose and [U-^{13}C]glutamine, (B) lactate export rate, and (C, D) steady-state fractional enrichment of downstream metabolites associated with glycolysis, TCA metabolism, and glutaminolysis of LNCaP and PC-3 cells labeled with (C) [U-^{13}C]glucose or (D) [U-^{13}C]glutamine.

significantly increased lactate FE compared to LNCaP cells (48±6.2 vs 32±5.7, N=3, $p<0.05$), indicating increased glucose flux through glycolysis (**Figure 3.2C**). This finding was supported by the significantly elevated LDH activity (12500±2880 vs 6300±974 mM NADH/min/million cells, N=9, $p<0.05$) in PC-3 cells compared to LNCaP cells (**Figure 3.3A**). Together, these data indicate that glucose flux through glycolysis is upregulated in PC-3 cells relative to LNCaP cells.

***TCA cycle activity*:** The TCA cycle plays an important role in prostate metabolism. Traditionally the healthy prostate gland is responsible for producing large amounts of citrate, which is then secreted into prostatic fluids. While this effect is drastically reduced in prostate cancer, citrate is an intermediate of the TCA cycle that is a precursor for lipid synthesis. In this study, LNCaP cells had a significantly higher steady-state intracellular concentration of citrate (22.3±1 vs

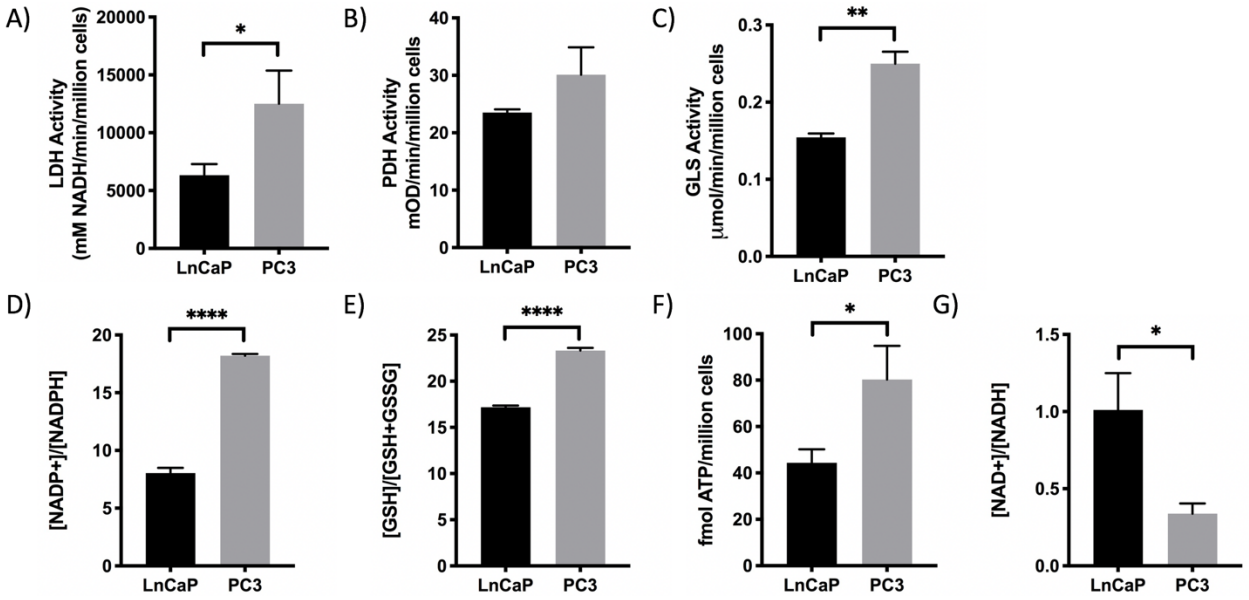

Figure 3.3. Key enzymes and associated cofactors were assessed in LNCaP and PC-3 cells using biochemical assays. Enzymatic activity of (A) LDH, (B) PDH, and (C) GLS were normalized to cell count. Glutathione redox balance was assessed based on (D) intracellular NADP+/NADPH and (E) ratio of reduced glutathione relative to total glutathione. Cellular bioenergetics of LNCaP and PC-3 cells was assessed based on (F) ATP content and (G) intracellular NAD+/NADH.

3.5±0.2 mmol/million cells, N=4, $p<0.0001$) compared to PC-3 cells. In contrast, PC-3 cells compared to LNCaP cells have significantly higher concentrations of aspartate (31.5±0.5 vs 18.9±1.3 mmol/million cells, N=4, $p<0.01$) and glutamate (82.2±1 vs 62.3±3 mmol/million cells, N=4, $p<0.05$), both of which are in fast exchange with α-ketoglutarate and oxaloacetate and inform on TCA activity downstream of citrate. This suggests that LNCaP cells favor a truncated TCA cycle in order to use intermediates of the TCA cycle for macromolecule synthesis, while PC-3 cells prefer a fully functional TCA cycle in order to maximize energy production. This is further strengthened by the [U-^{13}C]glucose labeling results, which revealed that PC-3 cells compared to LNCaP cells had increased glutamate FE (45±5.8 vs 28±3.9, N=3, $p<0.05$) and aspartate FE (56±2.5 vs 38±7.3, N=3, $p<0.05$), suggesting increased glucose utilization through

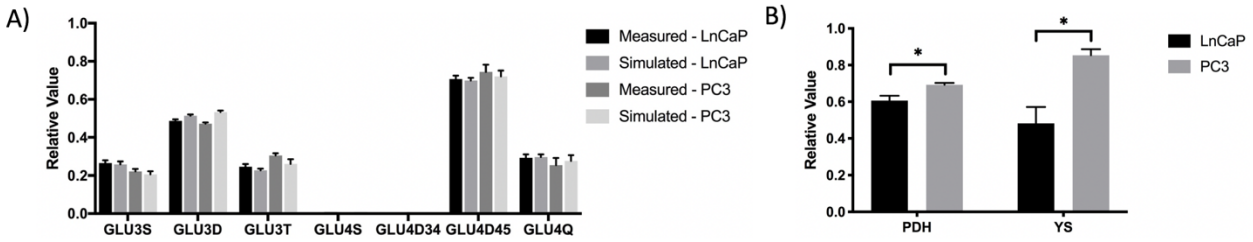

Figure 3.4. ^{13}C Isotopomer modeling of [U-^{13}C]glucose-labeled LNCaP and PC-3 cells using TCACALC. (A) Measured and simulated relative ^{13}C isotopomer areas of the glutamate C3 and C4 multiplets. (B) Calculated values for relative ^{13}C-glucose flux into TCA cycle (PDH) and the relative anaplerotic contribution per glucose (YS).

the TCA cycle. PC-3 cells also had higher PDH activity (29.5±3.8 vs 24.8±1.0 OD/min/million cells, N=3) than LNCaP cells (**Figure 3.3B**). To corroborate these findings, ^{13}C isotopomer modeling was performed on cell extracts labeled with [U-^{13}C]glucose using TCACALC. A good model fit was observed as reflected by the simulated isotopomer ratios closely matching experimental values (**Figure 3.4A**). ^{13}C isotopomer modeling of [U-^{13}C]glucose labeled cell extracts indicated significantly upregulated PDH flux in PC-3 cells (**Figure 3.4B**). These results clearly illustrate that glucose flux through the TCA cycle is upregulated in PC-3 cells.

***Glutaminolysis*:** PC3 cells had elevated glutamine consumption (27±7 vs 9±3 nmol/hr/million cells, N=4, p=0.056) compared to LnCaP cells (**Figure 3.2A**). As mentioned in the previous paragraph, PC-3 cells compared to LNCaP cells have significantly higher concentrations of glutamate, which is generated from glutamine via fast exchange with α-ketoglutarate and oxaloacetate and informs on TCA activity downstream of citrate. In [U-^{13}C]glutamine labeling studies, PC-3 cells had a significant increase in aspartate FE (65±4.6 vs 40±7.4, N=3, $p<0.05$), and glutamate FE (50±1.5 vs 32±4.4, N=3, $p<0.05$) compared to LNCaP cells, suggesting increased glutamine flux through glutaminolysis and anaplerosis into the TCA cycle (**Figure 3.2D**). Correspondingly, PC-3 cells also had significantly increased GLS activity compared to

LNCaP cells (250±15 vs. 154±5pmol/min/cell, N=3, $p<0.05$) (**Figure 3.3C**), in accord with the significantly increased activity through glutaminolysis observed after [U-^{13}C]glutamine labeling. This was corroborated by ^{13}C isotopomer modeling which indicated that PC-3 cells had significantly higher relative anaplerotic flux compared to LNCaP cells (**Figure 3.4B**). Together, these results indicate that glutaminolysis and glutamate anaplerosis are upregulated in PC-3 cells.

***Redox capacity*:** Interestingly glutathione redox balance was significantly different between LNCaP and PC-3 cells. PC-3 cells had significantly higher levels of glutathione (30.2±4 vs 16.2±1.2 mmol/million cells, N=4, $p<0.05$) than LNCaP cells. Furthermore, [U-^{13}C]glutamine labeling studies revealed that PC-3 cells had significantly increased glutathione FE (81±7.5 vs 45±1.3, N=3, $p<0.05$) compared to LNCaP cells, suggesting increased glutamine flux through glutathione synthesis to support redox balance (**Figure 3.2D**). This also correlates with the significantly increased NADP+/NADPH ratio in PC-3 compared to LNCaP cells (18.2±0.1 vs 8.0±0.4, N=3, $p<0.0001$) (**Figure 3.3E**) and significantly increased ratio of reduced glutathione relative to total glutathione (23.3±0.3 vs 17.1±0.2, N=3, $p<0.0001$) (**Figure 3.3F**), which supports previous observations in CRPC cell models[148]. Taken together, these results suggest that PC-3 cells have increased glutathione redox capacity compared to LNCaP cells.

Differential lipid composition between the PC-3 and LNCaP cells

Lipid metabolite concentrations quantified from 800 MHz ^{1}H NMR of the lipid extract fraction (**Figure 3.5**) are listed in **Table 3.2**. PC-3 cells had significantly lower concentrations of total esterified cholesterol (0.008±0.001 vs 0.21±0.002, N=4, $p<0.05$), indicating less lipid for fatty acid oxidation, compared to LNCaP cells (**Table 3.2**). PC-3 cells had significantly elevated

levels of phosphocholines (60.7±1.6 vs 40.8±2.0, N=4, p<0.05) (**Table 3.1**), which is an intermediate of phosphatidylcholine metabolism, compared to LNCaP cells. While PC-3 cells had a higher phosphatidylcholine concentration than LNCaP cells (**Table 3.2**), it was not significantly different between the two cell lines. PC-3 cells had significantly elevated levels of glycerophospholipids (0.082±0.017 vs 0.017±0.009, N=4, p<0.05), (**Table 3.2**) suggesting higher phospholipid membrane turnover and proliferation compared to LNCaP cells. This finding is supported by the faster doubling time of PC3 cells compared to LNCaP cells (24 vs 36 hours). These results suggest that lipid metabolism and composition are different between the androgen-dependent LNCaP cells and castration-resistant PC-3 cells.

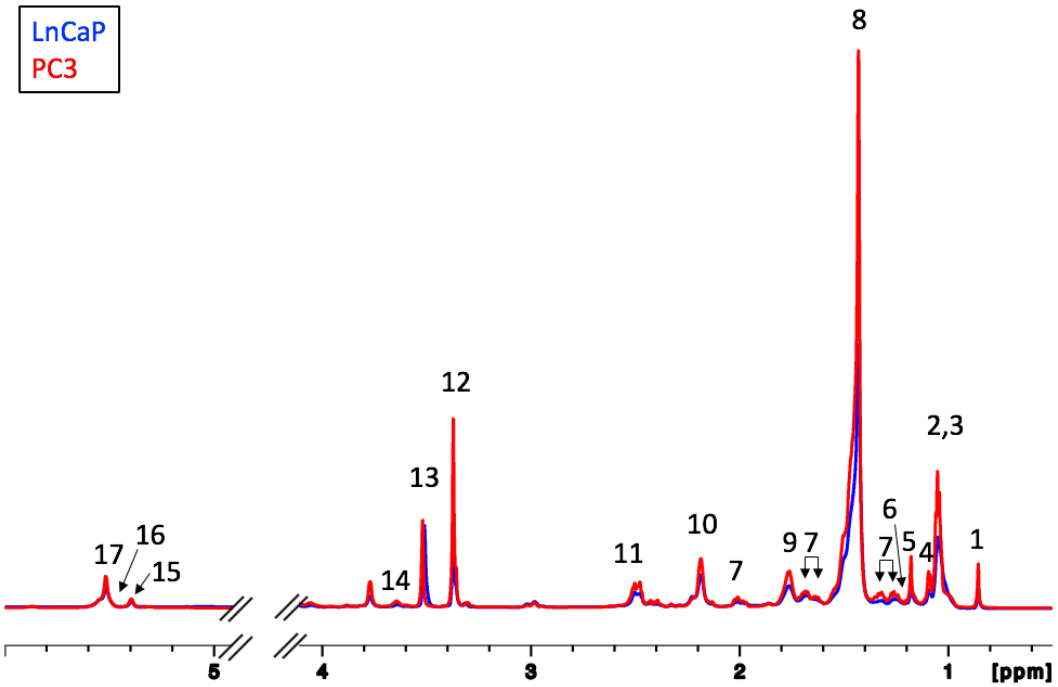

Figure 3.5. 1D ^{1}H spectrum of the lipid fraction of LNCaP (blue) and PC-3 (red) cell extracts. Peaks were assigned based on previous publications[76,77]: 1. Total cholesterol (C18 **H$_3$**), 2. Lipid (-C**H$_3$**), 3. Total cholesterol (C26 **H$_3$**/C27 **H$_3$**), 4. Total cholesterol (C21 **H$_3$**), 5. Free cholesterol (C19 **H$_3$**), 6. Esterified cholesterol (C19 **H$_3$**), 7. Multiple cholesterol protons, 8. Lipid (-CH$_2$-C**H$_2$**-CH$_2$-)$_n$, 9. Lipid (-CH$_2$-C**H$_2$**-CO), 10. Lipid (-CH$_2$-C**H$_2$**=CH), 11. Lipid (=CH-C**H$_2$**=CH), 12. Phosphatidylcholine, 13. Methanol, 14. Free cholesterol (C3 **H$_3$**), 15. Glycerophospholipid backbone, 16. Glycerol backbone, 17. Lipid (-**H**C=C**H**-).

Table 3.2. Steady-state lipid concentrations (nmol/million cells) of unlabeled LNCaP and PC-3 cell extracts (N=4).

	LNCaP			PC-3				
Metabolite	Average		SE	Average		SE	Raw p-value	Adjusted p-value
Total Cholesterol	0.256	±	0.056	0.345	±	0.045	0.263	0.913
Free Cholesterol	0.225	±	0.056	0.386	±	0.052	0.080	0.633
Esterified Cholesterol	0.021	±	0.002	0.008	±	0.001	0.003	0.043
Multiple Cholesterol Protons	1.559	±	0.373	2.625	±	0.444	0.116	0.741
Lipid(-CH3)	1.309	±	0.354	2.536	±	1.017	0.298	0.916
Lipid (-CH2-CH2-CH2-)	8.551	±	2.194	10.614	±	1.548	0.471	0.946
Lipid (-CH2-CH2-CO-)	0.814	±	0.217	1.271	±	0.470	0.411	0.946
Lipid (-CH2-CH2=CH-)	0.968	±	0.260	1.243	±	0.211	0.443	0.946
Lipid (-CH=CH2=CH-)	0.570	±	0.156	0.696	±	0.085	0.504	0.946
Lipid (-HC=CH-)	1.396	±	0.381	1.888	±	0.361	0.386	0.946
Total Lipid	13.609	±	3.544	18.248	±	3.502	0.388	0.946
Phosphatidylcholine	1.453	±	0.486	2.487	±	0.367	0.140	0.779
Glycerophospholipid Backbone	0.017	±	0.009	0.082	±	0.011	0.016	**0.043**
Glycerol Backbone	0.198	±	0.065	0.316	±	0.054	0.212	0.882

Differential Substrate Utilization of LNCaP and PC-3 cells

To better understand the relative utilization of glucose, long-chain fatty acids, and glutamine in the TCA cycle, OCR was measured using the Oxygraph+, and substrate preferences were assessed using the Seahorse XFe24 Extracellular Flux Analyzer. LNCaP cells displayed higher basal OCR compared to PC-3 cells (**Figure 3.6A**), suggesting that LNCaP cells have overall higher TCA activity compared to PC-3 cells. This is in line with the observation of higher contribution of OXPHOS of glucose in LNCaP cells (**Figure 3.6B**). This highlights the contribution of other substrates (besides glucose and glutamine) to the TCA activity. While glucose was the primary fuel source for OXPHOS in both cell lines when measured using the

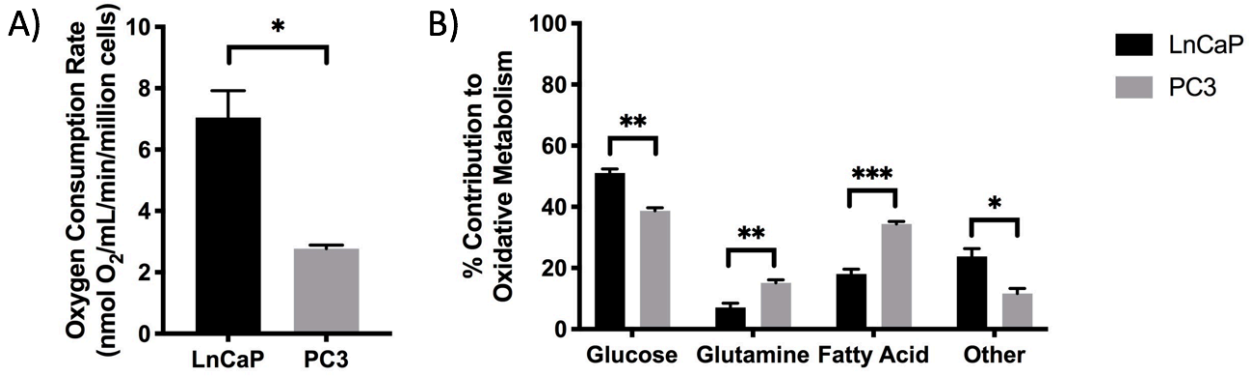

Figure 3.6. Oxygen consumption rate and relative substrate utilization for TCA metabolism of LNCaP and PC-3 cells. (A) Oxygen consumption rate of LNCaP and PC-3 cells was measured using a Clark-type O_2 electrode. (B) The relative contributions of glucose, long-chain fatty acid, and glutamine to the TCA cycle in prostate cancer cells was assessed using the Seahorse XFe24 Mito Fuel Flex assay.

Seahorse Mito Fuel Flex kit, PC-3 cells had significantly higher net anaplerosis (61±1 vs 49±1, N=3, $p<0.01$) than LNCaP cells (**Figure 3.6B**). PC-3 cells relied more on glutamine (15±1 vs 7±1, N=3, $p<0.01$) and long-chain fatty acids (34±1 vs 18±1, N=3, $p<0.001$) as anaplerotic fuel sources compared to LNCaP cells. Alternatively, LNCaP cells relied more on other anaplerotic contributors to mitochondrial respiration (23.8±2 vs 11±2, N=3, $p<0.05$) than PC-3 cells. This encompasses other anaplerotic substrates such as: short and medium chain fatty acids (e.g., proprionate, butyrate, octanoate), amino acids that enter through oxaloacetate (e.g., aspartate, asparagine), and branched-chain amino acids that enter through succinyl-CoA (e.g., leucine, isoleucine, and valine)[149].

Cellular bioenergetics were also assessed to understand the differential upregulation of glycolysis and the TCA cycle to meet the energy needs of LNCaP and PC-3 cells. PC-3 cells had significantly higher total ATP content (80±8 fmol/million cells vs 44±3 fmol/million cells, N=3, $p<0.05$) than LNCaP cells, suggesting that PC-3 cells have a higher energy capacity (**Figure 3.3F**) and supporting the observed upregulation of both glycolysis and the TCA cycle.

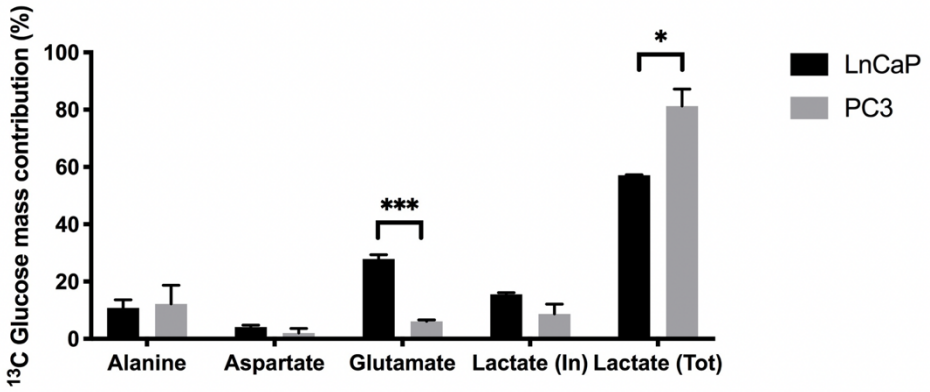

Figure 3.7. Relative mass contribution of ^{13}C-glucose to downstream metabolites.

Furthermore, PC-3 cells had a significantly lower NAD+/NADH ratio (0.33±0.07 vs 1.0±0.2, N=3, $p<0.05$) compared to LNCaP cells (**Figure 3.3G**), which is consistent with the significantly upregulated glycolysis in PC-3 cells[150-152]. This is further supported by the mass balance analysis of ^{13}C-glucose-labeled metabolites, which demonstrated that PC-3 cells utilized the majority of glucose consumed to produce lactate (**Figure 3.7**).

Gene set enrichment analysis supports correlation of altered metabolic pathways in PC-3 and LNCaP cell lines

Gene set enrichment analysis (GSEA) on LNCaP and PC-3 cells grown under normoxic conditions was assessed using publicly available RNAseq data[147]. PC-3 cells had positive enrichment of glycolysis pathway genes compared to LNCaP using the MsigDB Hallmark pathway gene sets, consistent with the metabolic findings of this study (**Figure 3.8A**). Inconsistent with metabolic findings which indicated a truncation of the TCA cycle and OXPHOS, LNCaP cells had greater enrichment of genes involved in OXPHOS (**Figure 3.8B**) and fatty acid metabolism (**Figure 3.8C**) compared to PC-3 cells.

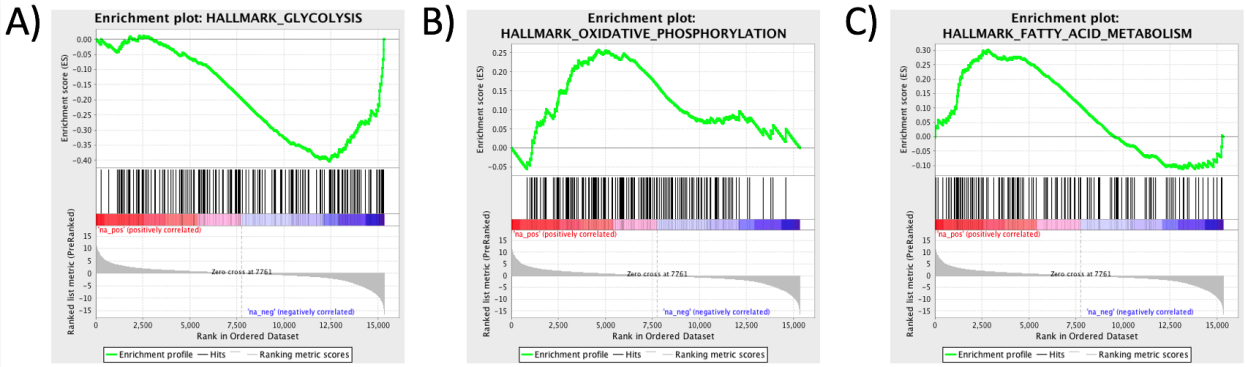

Figure 3.8. Gene expression pathway analysis of LNCaP (red) and PC-3 cells (blue). RNA sequencing data of LNCaP and PC-3 cells was acquired from GEO Accession GSE106305. Hallmark metabolic pathways of (A) glycolysis, (B), oxidative phosphorylation (i.e., TCA metabolism) and (C) fatty acid metabolism were assessed.

3.4.2. Changes in glucose and glutamine metabolism in the TRAMP model in response to primary androgen deprivation therapy

To verify that the metabolic alterations occurring in castration-resistant PC-3 cells versus androgen-dependent LNCaP cells are recapitulated *in vivo* in a murine model mimicking the development of CRPC in patients, metabolic changes were assessed after ADT in the TRAMP murine model. In this study TRAMP mice received orchiectomy, which significantly reduces serum testosterone levels and is equivalent to chemically-induced ADT in patients (**Figure 3.9A**). Response or resistance to ADT was based on changes in tumor volume one-week post-orchiectomy, in which mice with <25% increase in tumor volume were defined as androgen-dependent prostate cancer (ADPC), and mice with ≥25% increase in tumor volume were defined as CRPC (**Figure 3.9B**) similar to the clinical RECIST criteria[153]. Representative NMR spectra shown in **Figure 3.10** highlight the differences arising from the ^{13}C flux of metabolites between ADPC and CRPC in the TRAMP mice.

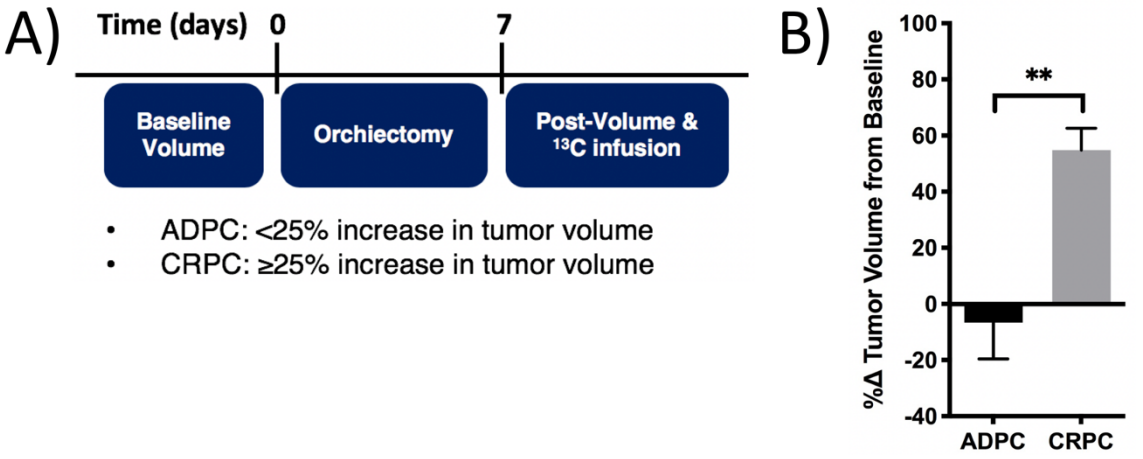

Figure 3.9. TRAMP treatment timeline and tumor volume changes in response to orchiectomy. (A) Treatment and study timeline for TRAMP mice. (B) Therapeutic response was determined based on tumor volume changes one-week post-orchiectomy (N=6 per group).

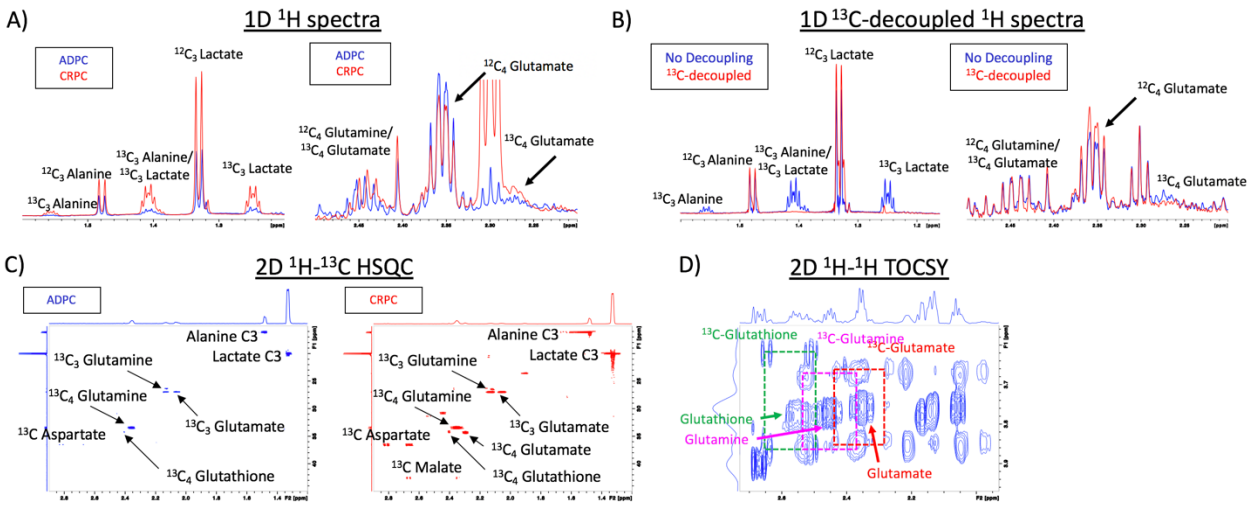

Figure 3.10. High-resolution NMR spectra of TRAMP tumor extracts. NMR spectra were acquired from of [U-^{13}C]glucose-labeled TRAMP tumor extracts using (A) conventional 1D proton, (B) 1D ^{13}C-decoupling ^{1}H, and (C) 2D ^{1}H-^{13}C HSQC. (D) 2D ^{1}H-^{1}H TOCSY was used to quantify glutathione FE in TRAMP tumor extracts labeled with [U-^{13}C]glutamine.

Table 3.3. Steady-state aqueous metabolite concentrations (nmol/mg wet tissue) of androgen-dependent and castration-resistant TRAMP tumors (N=3).

	ADPC			CRPC			
Metabolite	Average		SE	Average		SE	p-value
Acetate	5.6	±	3.7	2.6	±	0.6	0.4666
Alanine	12.8	±	7.1	16.2	±	1.3	0.6587
Aspartate	7.2	±	2.0	4.9	±	0.3	0.3377
Choline	1.6	±	0.1	2.5	±	1.7	0.6141
Citrate	2.6	±	0.2	1.4	±	0.3	0.0268
Creatine	20.7	±	1.2	11.3	±	2.2	**0.0198**
Creatine phosphate	1.9	±	0.7	1.0	±	0.3	0.2664
Glucose	21.1	±	1.1	10.9	±	4.0	0.0714
Glutamate	26.0	±	11.6	21.1	±	1.4	0.6936
Glutamine	7.3	±	3.3	5.2	±	0.6	0.5800
Glutathione	5.0	±	0.5	6.8	±	0.7	0.0969
Lactate	30.7	±	9.3	77.8	±	2.0	**0.0078**
Phosphocholine	13.3	±	2.7	10.2	±	2.3	0.4379
Glycerophosphocholine	11.9	±	2.9	13.2	±	4.1	0.8028
Myo-Inositol	14.7	±	5.4	3.7	±	0.3	0.1120
Total Choline*	26.8	±	5.5	26.0	±	7.8	0.9356

*Total choline was defined as the summed concentrations of choline, phosphocholine, and glycerophosphocholine.

***Glycolysis*:** The TRAMP model of progression from ADPC to CRPC demonstrated similar trends in steady-state metabolite concentrations to that observed in the cell models, such as decreased creatine, creatine phosphate, and citrate in CRPC compared to ADPC (**Table 3.3**). CRPC TRAMP tumors had significantly elevated levels of lactate (77.8±2 vs 30.7±9.3 nmol/mg tissue, N=3, $p<0.01$) compared to ADPC TRAMP tumors. In [U-^{13}C]glucose-labeling studies, CRPC TRAMP tumors also had a significant increase in lactate FE (81±4 vs 46±8, N=3, $p<0.05$) (**Figure 3.11A**), indicating increased flux through glycolysis compared to ADPC TRAMP tumors. CRPC TRAMP tumors had significantly elevated LDH activity (7.7±1.2 vs 2.0±0.6 μM NADH/min/μg protein, N=3, $p<0.05$) compared to ADPC TRAMP tumors (**Figure 3.12A**). Together this indicates that glycolysis is upregulated in treatment-driven CRPC TRAMP tumors.

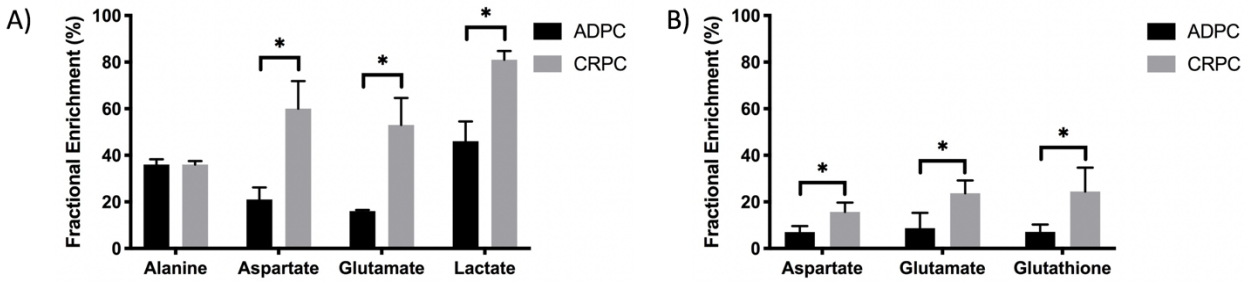

Figure 3.11. Fractional enrichment profiles of TRAMP tumors labeled with (A) [U-^{13}C]glucose (N=3) or (B) [U-^{13}C]glutamine (N=3).

***TCA Cycle Activity*:** CRPC TRAMP tumors had increased glutamate FE (53±12 vs 16±0.5, N=3, $p<0.05$) and aspartate FE (60±12 vs 21±5, N=3, $p<0.05$) compared to ADPC TRAMP tumors, suggesting increased pyruvate flux through TCA metabolism (**Figure 3.11A**). CRPC TRAMP tumors also had higher PDH activity (4.24 vs 2.28 μOD/min/μg protein) compared to ADPC TRAMP tumors (**Figure 3.12B)**. Together these findings suggest that CRPC TRAMP tumors have elevated TCA metabolism of glucose compared to ADPC TRAMP tumors.

***Glutaminolysis*:** Glutamine-dependent pathways such as glutaminolysis, anaplerosis into TCA cycle, and glutathione redox balance were then assessed using the TRAMP model. While the steady-state concentrations of aspartate and glutamate were not significantly different between ADPC and CRPC TRAMP tumors, [U-^{13}C]glutamine studies revealed that CRPC TRAMP tumors had significantly increased aspartate FE (16±2.3 vs 7±1.5, N=3, $p<0.05$) and glutamate FE (24±3.2 vs 9±3.8, N=3, $p<0.05$) compared to ADPC tumors, demonstrating increased flux through glutaminolysis and increased anaplerosis into the TCA cycle (**Figure 3.11B**). The upregulation of glutaminolysis is further supported by significantly higher GLS activity (6.4±0.4 vs 4.9±0.1 pmol/min/ug protein, N=3, $p<0.05$) observed in CRPC versus ADPC TRAMP tumors (**Figure 3.12C**).

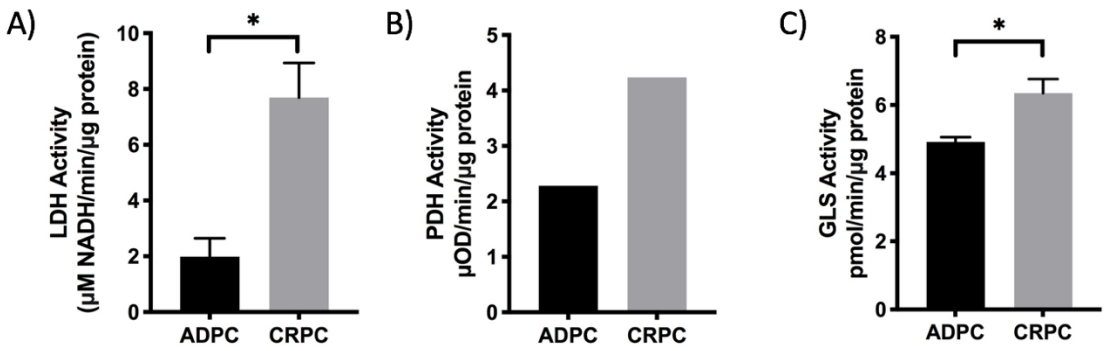

Figure 3.12. Key enzymes were assessed in TRAMP tumors using enzymatic assays. (A) LDH activity (N=3), (B) PDH activity (N=1) and (C) GLS activity (N=3) was determined from TRAMP tumors after orchiectomy.

***Redox Capacity*:** [U-^{13}C]glutamine-labeling studies also showed that CRPC TRAMP tumors had significantly elevated glutathione FE (24±6 vs 7±1.8, N=3, $p<0.05$) compared to ADPC tumors, suggesting increased flux through glutathione synthesis to support redox balance (**Figure 3.10B**). Together, these results indicate that CRPC TRAMP tumors have significantly increased glucose and glutamine flux through glycolysis, TCA metabolism, glutaminolysis, and glutathione redox potential. Future work will assess NADP/NADPH ratio and ratio of reduced glutathione (GSH) relative to total glutathione (GSH+GSSG) in the TRAMP model to corroborate our metabolic findings.

3.5. Discussion

In this study, the metabolic flux of [U-^{13}C]glucose and [U-^{13}C]glutamine through glycolysis, TCA metabolism, and glutaminolysis was characterized, initially using androgen-dependent (LNCaP) and castration-resistant (PC-3) human cell lines, and then using the TRAMP murine model to assess the metabolic changes associated with the development of CRPC

.(**Figure 3.13**). Steady-state metabolite concentrations and FE were measured using high-resolution 1D and 2D NMR techniques, which revealed that CRPC was associated with

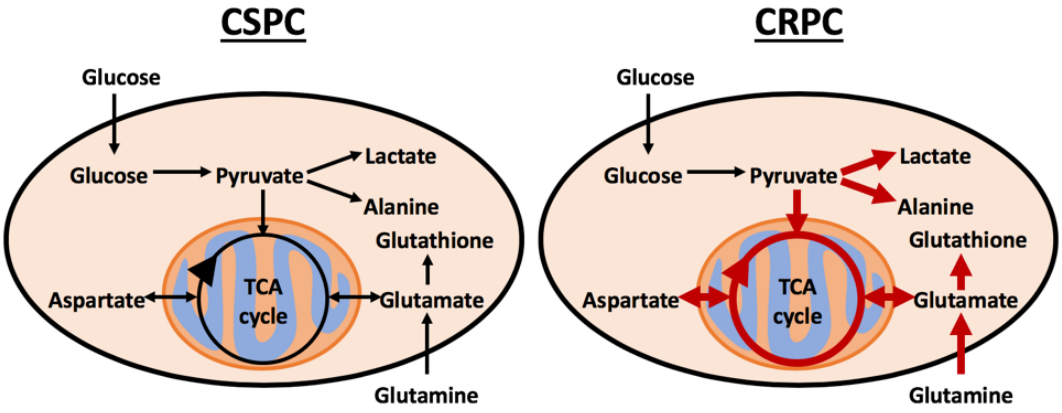

Figure 3.13. Schematic detailing the metabolic alterations observed between ADPC and CRPC.

increased flux through glycolysis, TCA metabolism of pyruvate and glutamine, glutaminolysis, and glutathione synthesis in both the prostate cell line and TRAMP models. These findings were further supported by (1) ^{13}C isotopomer modeling using TCACALC showing increased PDH and anaplerosis, (2) enzymatic assays showing increased LDH activity, PDH activity, GLS activity, (3) measurements of OCR showing increased dependence on anaplerotic fuel sources for mitochondrial respiration correlating with androgen-independence, and (4) gene set enrichment analysis of glycolysis, OXPHOS, and lipid synthesis.

Overall, our findings using human and mouse models are consistent with our hypothesis that castration-resistant growth would alter the behavior of AR-regulated metabolic pathways, including upregulation of glycolysis, glutaminolysis, TCA metabolism, and glutathione redox capacity. Results from studies of prostate cancer cell lines showed that both LNCaP and PC-3 cells have similarly high rates of glucose consumption, in accordance with other studies that showed upregulation of glycolysis despite no significant difference in glucose consumption in castration-resistant cell models[154-158] and mouse xenograft models[158].

The traditional 'Warburg effect' proposed that cancer cells highly favored glycolysis and reduced mitochondrial OXPHOS for generation of ATP for energy[159]. As discussed by Zheng (2012)[160], this occurs for several reasons. Rapidly proliferating tissues favor glycolysis to meet energetic demands since glycolysis generates ATP faster than OXPHOS. Furthermore, the intermediates of glycolysis and a truncated TCA cycle can provide nucleic acids, lipids, and amino acids required for cancer growth and proliferation[160]. Warburg concluded that the observed upregulation of glycolysis and downregulation of OXPHOS was due to mitochondrial dysfunction[161]. However, OXPHOS has been shown to reactivate in aggressive, metastatic cancers in order to support higher proliferation rates and the higher nutrient and energy demands of advanced prostate cancer[160]. This is evidenced by the key signaling pathways commonly upregulated in patients with aggressive prostate cancer, including the LKB1-AMPK-p53 and PI3K-Akt-mTOR pathways, as well as MYC-mediated glutaminolysis[162]. The shift in glycolysis to reactivation of OXHPHOS has also been evidenced in cancers as they adapt and differentiate into new subtypes. Studies have also shown that rapidly proliferating tissues rely more on glycolysis for ATP production while tissues that are undergoing differentiation rely primarily on OXPHOS for energy production[160].

Interestingly, PC-3 cells had lower OCR and lower enrichment of OXPHOS pathway genes than LNCaP cells despite having higher PDH activity. This matches published studies[154,155], which concluded that LNCaP cells rely mainly on OXPHOS for ATP generation while PC-3 cells rely mainly on glycolysis. Previous studies have shown that AR signaling promotes a truncated TCA cycle by stimulating anabolism of glucose to citrate, resulting in significantly higher citrate levels but no change in succinate levels[134]. This is supported by the significantly higher citrate concentration but no change in aspartate or glutamate concentration

observed in castration-resistant PC-3 and TRAMP CRPC tumors compared to the androgen-dependent LNCaP and TRAMP ADPC tumors. Glucose flux to citrate production could not be observed in this study due to the low concentration of citrate and its associated ^{13}C-labeled counterpart. Future studies using mass spectrometry, which is more sensitive than NMR, to quantify ^{13}C isotopologue enrichments would further elucidate this phenomenon. Studies have also shown that the mitochondrial PDH complex provides cytosolic citrate for lipid synthesis to sustain anabolism required for tumorigenesis[163]. Further studies should be performed to dissect how post-transcriptional regulation of TCA metabolism is altered as prostate cancer transitions from an androgen-dependent to a castration-resistant phenotype.

Although glutamine consumption was not significantly different between PC-3 and LNCaP cells, the [U-^{13}C]glutamine-labeling showed that the castration-resistant PC-3 cells had increased glutamine utilization through glutaminolysis, anaplerosis through the TCA cycle, and glutathione synthesis compared to LNCaP cells. This supports other studies showing that several proteins involved in glutamine metabolism were upregulated in castration-resistant cell lines[164], and further demonstrates the importance of glutaminolysis in cancer growth and therapeutic resistance. Studies have shown that increased glutaminolysis is required for activation of the mTORC1 signaling pathway, which upregulates metabolism of glucose, glutamine and other amino acids, and lipids[165].

Interestingly, glutathione synthesis was significantly upregulated in both castration-resistant PC-3 cells and treatment-emergent CRPC mouse models. Several studies have shown that CRPC has higher redox capacity based on increased expression of glutathione-related antioxidant genes such as glutathione peroxidase (GPX2) and glutathione synthase (GSS)[148,166]. This may be a critical step in the development of CRPC since glutathione prevents apoptosis by

neutralizing free-radicals and reactive oxygen species (ROS) that would otherwise cause oxidative damage to DNA, proteins, and lipids[167].

Limitations of this study include the inherent insensitivity of NMR, which prevents characterization of low-concentration intermediates of glycolysis, TCA cycle, and fatty acid metabolism. Another limitation is the lack of NMR-based ^{13}C isotopomer models that can model metabolic fluxes of [U-^{13}C]glutamine through glutaminolysis and the TCA cycle. Furthermore, many ^{13}C isotopomer models require that ^{13}C-labeling reaches steady-state, as determined by stable fractional enrichments over time. While this was achieved in our cell labeling studies, the TRAMP labeling study does not meet this criterion and would require non-steady state models. Future work will focus on using mass spectrometry to address both of these concerns and validate our initial NMR-based findings.

In conclusion, unique metabolic alterations in glucose and glutamine metabolism were associated with progression to CRPC. Specifically, glycolysis, TCA metabolism of pyruvate and glutamine, glutaminolysis, and glutathione synthesis are upregulated in castration-resistant human prostate cancer cells and in treatment-driven CRPC TRAMP tumors. These results support the use of hyperpolarized [1-^{13}C]pyruvate to assess glycolysis, [2-^{13}C]pyruvate to assess TCA metabolism, [5-^{13}C]glutamine to assess glutaminolysis, and [1-^{13}C]dehydroascorbate to assess glutathione redox potential as non-invasive imaging biomarkers. These pathways may also serve as candidate drug targets for the treatment of CRPC in patients. Future work will focus on correlating our metabolic findings with gene expression of key transporters and enzymes involved in glycolysis, glutaminolysis, TCA metabolism, and lipid metabolism. Characterizing fatty acid oxidation would also compliment this work since this is considered to be a dominant bioenergetic pathway in prostate cancer[168].

3.6. Future Directions

Early metabolic response to apalutamide (ARN-509), a second-line androgen pathway inhibitor

Treatment options for men with CRPC start with hormonal therapies that target the androgen receptor pathway followed by chemotherapy, which is often combined with a targeted biologic agent[27]. Second-line androgen pathway inhibitors (API) such as enzalutamide, apalutamide and abiraterone, have been shown to bind to AR with much higher affinity than first-line antiandrogens such as bicalutamide, thereby effectively retarding the growth of CRPC[30]. Currently no reliable clinical or noninvasive imaging methods can predict the therapeutic response to API, which is critical in guiding treatment decisions for patients with CRPC.

In order to identify biomarkers that can monitor therapeutic response in individual patients, the early metabolic response of CRPC TRAMP tumors to apalutamide (ARN-509), a second-line API, was assessed. CRPC TRAMP that underwent daily treatment with apalutamide (ARN-509) at 30 mg/kg/day administered via oral gavage[144] for seven days were defined as CRPC+ARN. No significant difference in tumor growth rate was observed between CRPC TRAMP and CRPC+ARN TRAMP (**Figure 3.14**).

An early metabolic response was observed in CRPC TRAMP tumors after ARN-509 treatment. CRPC+ARN TRAMP tumors had lower levels of choline metabolites (choline, phosphocholine, glycerophosphocholine, and total choline), indicating reduced proliferation

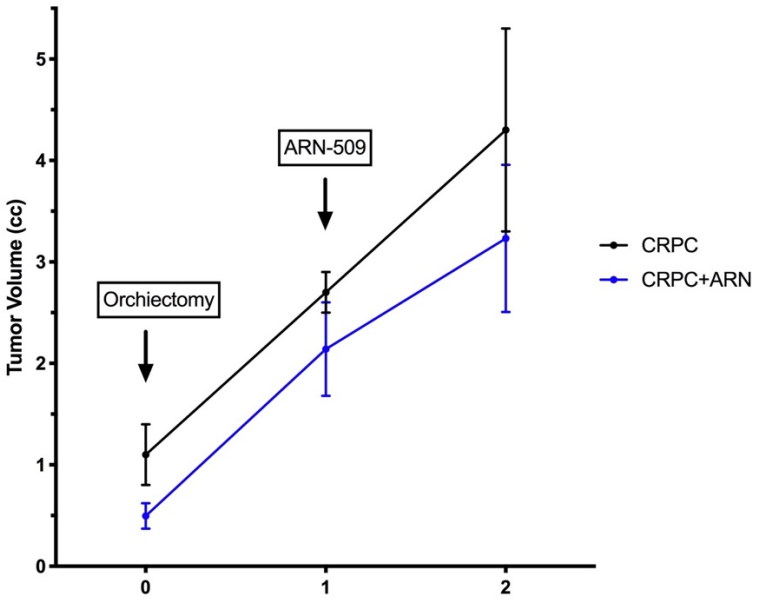

Figure 3.14. Tumor growth rate of CRPC TRAMP tumors treated with apalutamide. TRAMP tumors that grew ≥ 25% in tumor volume one-week after orchiectomy were defined as CRPC. An additional cohort of CRPC TRAMP that underwent one week of daily apalutamide (ARN-509) treatment was defined as CRPC+ARN. Data is presented as average ± standard error (N=3 per group).

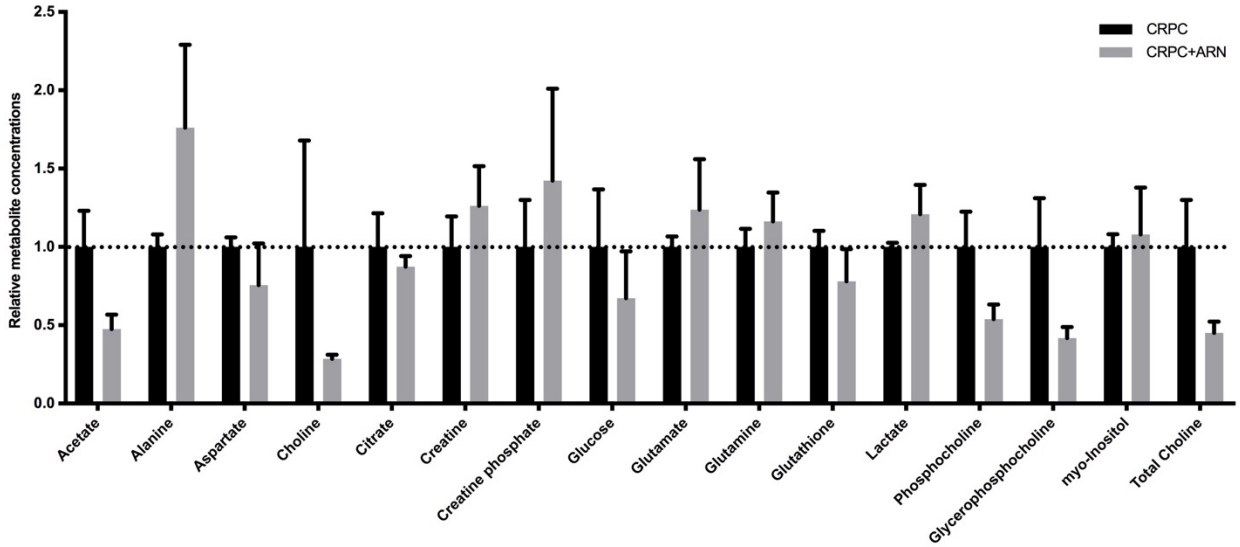

Figure 3.15. Relative changes in metabolite concentration in CRPC TRAMP tumors treated with apalutamide. Relative metabolite concentrations are presented as average ± standard error (N=3) after normalization to wet tissue weight. Total choline was defined as the summed concentrations of choline, phosphocholine, and glycerophosphocholine.

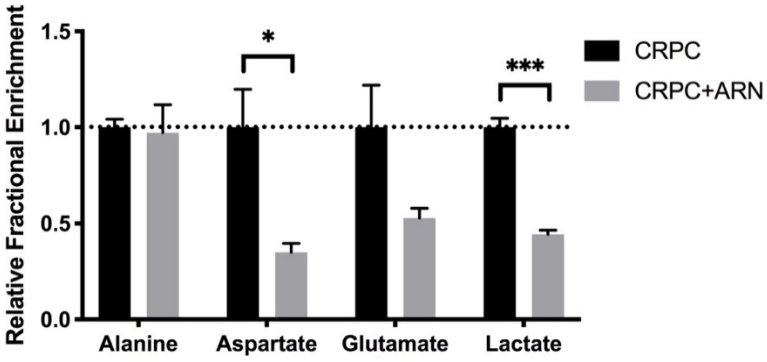

Figure 3.16. Relative changes in fractional enrichment of [U-^{13}C]glucose-labeled CRPC TRAMP tumors treated apalutamide. Bar graph is presented as average ± standard error (N=3).

compared to CRPC TRAMP (**Figure 3.15**). No significant changes in steady-state concentrations were observed for the other metabolites listed in **Figure 3.15**.

[U-^{13}C]glucose labeling studies showed a drastic reduction in glycolysis and glucose contribution to TCA metabolism in CRPC TRAMP tumors after API treatment. CRPC+ARN TRAMP tumors had 56% lower lactate FE ($p<0.001$, N=3), indicating downregulation of glycolysis compared to CRPC TRAMP tumors (**Figure 3.16**). CRPC+ARN tumors also had 65% lower aspartate FE ($p<0.05$, N=3) and 47% lower glutamate FE ($p=0.10$, N=3), indicating downregulation of TCA metabolism compared to CRPC tumors (**Figure 3.16**). In fact, the FE levels of aspartate, glutamate, and lactate of CRPC+ARN TRAMP tumors had reverted back to FE levels observed in ADPC TRAMP tumors. No difference in alanine FE was observed between the two treatment groups.

In conclusion, glucose utilization through glycolysis and TCA cycle metabolism was downregulated in CRPC TRAMP tumors treated with ARN-509. This reduction in metabolism is consistent with what was observed in recently published hyperpolarized [1-^{13}C]pyruvate MR imaging studies of patients with prostate cancer after primary ADT[26]. As this metabolic response was observed prior to a decrease in tumor growth rate, biomarkers of these pathways could be

used to monitor therapeutic response in patients. These results support the use of hyperpolarized [1-^{13}C]pyruvate and FDG-PET to assess glycolysis and hyperpolarized [2-^{13}C]pyruvate to assess TCA metabolism. One caveat of this study is that the CRPC TRAMP tumors were collected one-week post-orchiectomy, while CRPC+ARN TRAMP tumors were collected two-weeks post-orchiectomy. The metabolic assessment of CRPC tumors two-weeks post-orchiectomy treated with vehicle as well as stable isotope labeling studies using [U-^{13}C]glutamine is currently ongoing. Future work will assess the long-term metabolic adaptations and tumor growth inhibition of prolonged API treatment using the TRAMP model.

CHAPTER FOUR

Metabolic Adaptations of Treatment-Emergent Small Cell Neuroendocrine Prostate Cancer using Patient-Derived Xenograft Models

4.1. Abstract

Treatment-emergent small cell neuroendocrine cancer (t-SCNC) is an increasingly prevalent and lethal subtype of castration-resistant prostate cancer (CRPC). There is an unmet clinical need to develop a non-invasive imaging technique to identify the presence of t-SCNC for improved treatment of metastatic CRPC patients. Hyperpolarized ^{13}C MRI (HP ^{13}C MRI) is a new metabolic imaging method that could provide a non-invasive means to image the presence of t-SCNC *in vivo*. The goal of this study was to identify metabolic differences between CRPC and t-SCNC patient-derived xenografts (PDXs) in order to identify HP ^{13}C MR probes that can discriminate between CRPC and t-SCNC in future patient studies. CRPC and t-SCNC PDXs labeled with either [U-^{13}C]glucose or [U-^{13}C]glutamine were differentiated with 95% confidence using untargeted principal component analysis. Fractional enrichment analysis of the same PDXs demonstrated that t-SCNC PDXs had significantly elevated flux of glucose through glycolysis and tricarboxylic acid (TCA) metabolism, as well as elevated flux of glutamine through glutaminolysis and TCA metabolism as compared to CRPC PDXs. This data suggests that a combination of HP ^{13}C]pyruvate, [2-^{13}C]pyruvate and [5-^{13}C]glutamine could distinguish t-SCNC from CRPC in future HP ^{13}C MRI patient exams for improved treatment selection for patients with metastatic CRPC.

4.2. Introduction

Treatment-emergent small cell neuroendocrine cancer (t-SCNC) is an increasingly prevalent, lethal subtype of castration-resistant prostate cancer (CRPC) that arises as an adaptive response to protracted treatment using primary androgen deprivation therapy (ADT) and second-generation potent androgen pathway inhibitors (APIs)[31,32]. Potent inhibitors of the androgen

receptor (AR), such as abiraterone, apalutamide and enzalutamide, have recently been approved for management of patients with metastatic CRPC (mCRPC). While these therapies have greatly improved progression-free survival and overall survival in patients with mCRPC[169,170], half of patients relapse within one year, and chronic AR inhibition by these therapies can lead to the outgrowth of t-SCNC, also known as aggressive variant and neuroendocrine prostate cancer (NEPC) in the literature.

Morphologically, t-SCNC is similar to *de nov*o small cell neuroendocrine prostate cancer (SCNC), a highly aggressive and lethal subtype found in less than 2% of treatment-naïve patients with prostate cancer at time of diagnosis[171]. The t-SCNC subtype is more lethal than CRPC and contributes to at least 25% of the 26,000 cases of lethal prostate cancer per year in the United States[33,34], with a median survival rate of only 7 months after diagnosis[34,172]. Significant heterogeneity underlies the biology of CRPC, with frequent admixture of adenocarcinoma (aCRPC) and small cell (t-SCNC) histology within and across CRPC patients.

New therapies are required to effectively treat t-SCNC. Patients with t-SCNC are expected to show poor response to second-generation APIs. For example, Xtandi® (enzalutamide), which costs up to $129,000 for a year of treatment, is expected to have up to a 50% initial failure rate in this patient population. Several therapies are currently available and being developed for t-SCNC, including platinum-based chemotherapy, inhibitors of glutamine metabolism (e.g., CB-839), and other MYC-directed treatment strategies (e.g., bromodomain inhibitors). However, there is currently no clear method to identify the presence of t-SCNC or monitor its response to treatment. Therefore there is an unmet need to develop a non-invasive imaging modality to identify the presence of t-SCNC and enable improved treatment selection for patients with metastatic CRPC[173,174].

The only definitive method to clinically diagnose t-SCNC is immunohistochemical (IHC) staining of tumor biopsies using neuroendocrine markers such as chromogranin A and synaptophysin[32]. However, intra-tumoral heterogeneity, sampling errors and the impracticality of serial sampling underscore the limitations of these biopsies. Neither blood tests (such as prostate-specific antigen or neuroendocrine markers) or standard imaging metrics (such as ^{1}H MRI and FDG PET) can reliably distinguish t-SCNC from aCRPC or monitor its response to therapy. Therefore, identifying metabolic biomarkers that reliably capture the heterogeneity of advanced prostate cancer, particularly the presence of SCNC, are of importance for selecting the appropriate therapy for individual patients and for the development of new therapeutic strategies.

Hyperpolarized ^{13}C MRI (HP ^{13}C MRI) is a powerful new imaging method that can be used to observe metabolic fluxes through key pathways associated with cancer progression and therapeutic response in patients[125]. Several studies have found significant overexpression and gene amplification of N-MYC in SCNC compared to prostate adenocarcinomas[171,175]. MYC overexpression may be an oncogenic driver leading to a t-SCNC phenotype in patients[175,176] and in immortalized human prostate cancer cell lines[176,177]. Overexpression and gene amplification of AURKA and N-MYC was found in 40% of patients with t-SCNC compared to only 5% of patients with pre-existing prostate adenocarcinoma[171]. Overamplification of N-MYC has been shown to be predictive of poor outcome in patients[178]. The MYC family of genes regulates transcription, nucleotide biosynthesis and lipid synthesis, glycolysis, and glutaminolysis[179,180]. Dysregulation of N-MYC is known to increase the expression of glucose and glutamine transporters, alter single-carbon metabolism, enhance anaplerosis, and increase expression of LDH, GLS and the lactate exporter MCT4. While the effects of MYC overexpression in t-SCNC are unknown, recent genomic and metabolomic data of neuroendocrine pancreatic[35] and lung[36]

tumors have shown that a combined upregulation of the PI3K/AKT pathway and MYC expression lead to elevated aerobic glycolysis and glutaminolysis[37]. Several therapies have been developed to target MYC and its downstream metabolic effects[181], including aurora kinase inhibitors[182] and CB-839, a potent and selective GLS inhibitor that is currently in several phase I/II trials for treating RCC, non-small cell lung cancer, and colorectal cancers[183]. Together this indicates that glucose and glutamine metabolism may be altered in t-SCNC and that characterization of the metabolic phenotype of t-SCNC may identify new biomarkers of t-SCNC and its response to therapy. While initial pre-clinical and patient studies have focused on using [1-^{13}C]pyruvate to investigate changes in glycolysis, HP probes that provide insight into other metabolic pathways, such as [2-^{13}C]pyruvate and [5-^{13}C]glutamate, have been investigated pre-clinically, and clinical translation of these probes is in progress. However, to date, the metabolic phenotype of t-SCNC has not been fully defined.

While several preclinical models of treatment-naïve prostate adenocarcinoma and aCRPC have been published, few preclinical models of SCNC exist. Patient-derived xenograft (PDX) models are considered the most representative biological model since they preserve the molecular and genetic features of the original patient disease. Several CRPC and t-SCNC PDXs have been established[184,185]. However, the metabolic features of these models have not been fully characterized. The goal of this study was to understand the metabolic differences between CRPC and t-SCNC PDXs in order to identify HP ^{13}C MR probes that can discriminate between CRPC and t-SCNC in future patient studies. To accomplish this goal, principal component analysis (PCA) and [U-^{13}C]glucose- and [U-^{13}C]glutamine- labeling methods were performed to characterize flux through glycolysis, the tricarboxcylic acid (TCA) cycle, alanine synthesis and glutaminolysis in CRPC and t-SCNC using PDX models.

4.3. Materials and Methods

PDX Models

Detailed information about the origin and generation of PDXs has previously been published[184,185]. PDXs were transplanted under the subrenal capsule of male NSG mice obtained from the Jackson Laboratory. All CRPC PDXs (LTL-313HR, LuCaP 77CR, **Table 4.1**) used in this study were experimentally-derived castration-resistant sublines. All t-SCNC PDXs (LTL-352, LTL-610, LuCaP 93, **Table 4.1**) were derived from patients who underwent prolonged androgen deprivation therapy.

In vivo ^{13}C-infusion

Mice with tumors were injected with a bolus of either 80 μL 25%wt/volume [U-^{13}C]glucose or 200 μL 35.73 mg/mL [U-^{13}C]glutamine via tail vein every 15 minutes for a total labeling time of 45 minutes[49]. To minimize the effects of stress and anesthesia on metabolism, mice were briefly anesthetized using isoflurane for 2-3 min to perform ^{13}C-injection and then allowed to wake in between injections. Tissue was collected immediately upon euthanasia and either flash-frozen in liquid nitrogen for metabolomic analysis or fixed in formalin for histological analysis.

Cell and tissue extraction

Cells and frozen tissue was homogenized in 600 μL cold methanol using a bead homogenizer at 4°C. Metabolites were extracted using cold 1:1:1 methanol:water:chloroform protocol[68]. Aqueous fractions were isolated, lyophilized, and resuspended in 600 μL D_2O for NMR analysis. An internal standard of TSP was used for quantification.

Table 4.1. List of CRPC and t-SCNC PDX lines used in this study.

PDX	Phenotype	Site of Origin	$N_{glucose}$	$N_{glutamine}$
LTL-313HR	CRPC	Primary AdenoPC	3	3
LuCaP 77CR	CRPC	Femur Metastasis	3	3
LTL-352	t-SCNC	Urethral Metastasis	3	3
LTL-610	t-SCNC	Primary t-SCNC	3	3
LuCaP 93	t-SCNC	Primary t-SCNC	3	3
LuCaP 145.1	t-SCNC	Liver Metastasis	3	3

NMR acquisition

High-resolution NMR spectra were acquired on an 800 MHz Bruker AvanceI equipped with a 5 mm triple resonance TXI cryoprobe. *^{13}C-decoupled ^{1}H presaturation pulse*: α=90, TD=24k, SW=15 ppm, TR=12 seconds, AQ=0.5 seconds, NS=32. Water signal was suppressed using a presaturation pulse. Adiabatic decoupling was applied during acquisition using a CHIRP pulse with 54 kHz sweep width (equivalent to 200 ppm @ 800 MHz), and shaped pulse power level of +2dB with respect to the power level determined for ^{13}C-GARP. Total scan time was 6 minutes. *^{1}H-^{13}C HSQC*: A phase-sensitive 2D HSQC using echo-antiecho, adiabatic inversion pulses (hsqcetgpsp) and no ^{13}C decoupling during acquisition was acquired with the following parameters: TD=2048x4096, SW=6x120 ppm, TR=1.5 seconds, AQ = 0.297 seconds, NS=2, J_{CH} = 135 Hz (average J_{CH} of 127, 130, and 145 Hz for glutamate C2, C3, and C4). Data was zero-filled in both dimensions to a final digital resolution of 2.9 Hz/point in the F2 dimension. Total scan time was 4 hours.

NMR quantification

1D NMR datasets were processed using MestreNova (version 12). The datasets were zero-padded by a factor of 2, apodized with a 0.5 Hz exponential filter, and manually phased and baselined. Peaks of interest were automatically fit using a Lorentzian-Gaussian shape function. 2D NMR datasets were processed using TopSpin (version 4.0.6). 2D datasets were zero-padded by a factor of 2, manually phased, and peak volumes were integrated.

Total metabolite concentrations were quantified from 1D ^{13}C-decoupled ^{1}H water presaturation spectra of ^{13}C-labeled tissue extracts. Fractional enrichment (FE) was quantified as $[^{13}\text{C-labeled metabolite}]_{HSQC}/[\text{total metabolite}]_{\{13C\}1H}$. Total metabolite concentrations for all other metabolites were quantified using ^{13}C-decoupled ^{1}H spectra by manually fitting peaks of interest using a Lorentzian-Gaussian shape. The concentration of ^{13}C-labeled metabolites was quantified using ^{1}H-^{13}C HSQC by integrating the volumes of the cross-peaks as previously described using **Equation 2.3**, and the lactate concentration quantified from 1D ^{13}C-decoupled ^{1}H water presaturation spectra was used as the reference compound.

Principal Component Analysis

Multivariate data analysis and principal component analysis (PCA) were performed on 1D ^{1}H spectra without ^{13}C-decoupling pre-processed in MestreNova as described above. The spectral regions corresponding to water (4.6–4.9 ppm) and TSP (0.00–0.70 ppm) peaks were excluded, and the remaining spectral regions were normalized using probabilistic quotient normalization (PQN) and subsequently divided into 0.03 ppm bins. The binning table contained the spectral region of 0.7 to 5.8 ppm. Classical PCA was performed with mean centering and Pareto scaling using the ChemoSpec R package (version 5.1.48)[186].

Statistics

Nested t-test was used to compare steady-state metabolite concentrations and fractional enrichment comparisons of aCRPC and t-SCNC using Prism. All statistics are reported as mean ± standard error. P-values less than 0.05 (*p <0.05, **p <0.01 and ***p <0.001) were considered significant.

4.4. Results

Steady-state lactate concentration significantly increased in t-SCNC versus aCRPC

Representative high-resolution NMR spectra of aCRPC and t-SCNC PDX tumor extracts shown in **Figure 4.1A** illustrate the similarity in metabolic profile and pool sizes between the two groups. Quantification of these metabolite pools indicated that only lactate concentration in t-SCNC compared to aCRPC tumors was significantly elevated (80±6 vs 44±6.5 nmol/mg tissue, N=4, p<0.01) (**Figure 4.1B**).

Untargeted PCA of 1D ^{1}H spectra of PDX tumors labeled with [U-^{13}C]glucose and [U-^{13}C]glutamine demonstrated metabolic changes between t-SCNC and aCRPC

Global changes in glucose and glutamine metabolism were initially assessed between aCRPC and t-SCNC using PCA followed by an in-depth analysis of 1D and 2D heteronuclear spectroscopic data. First, alterations in glucose metabolism of aCRPC and t-SCNC PDXs were assessed using [U-^{13}C]glucose -labeled tumor extracts by analyzing spectra with 1D ^{13}C-decoupled ^{1}H spectra. aCRPC and t-SCNC PDXs were differentiated with 95% confidence using

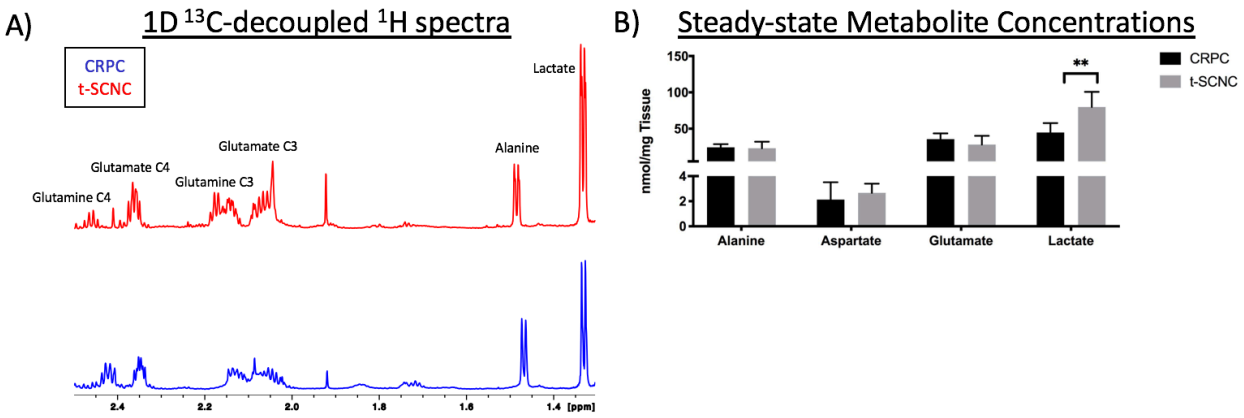

Figure 4.1. Quantification of aqueous metabolites in aCRPC and t-SCNC PDX tumor extracts using 1D ^{13}C-decoupled proton NMR. (A) Representative 1D proton spectra of aCRPC (LuCaP 77CR) and t-SCNC (LuCaP 145.1) PDX tumor extracts normalized to tissue weight. (B) Metabolite concentrations of aCRPC (LuCaP 77CR, LTL-313HR, N=6) and t-SCNC (LTL-352, LTL-610, LuCaP 93, LuCaP 145.1, N=12) extracts were quantified from 1D ^{13}C-decoupled ^{1}H spectra. Data are presented as mean ± standard error. **p<0.01.

PCA analysis of tumors labeled with [U-^{13}C]glucose (**Figure 4.2A**). PCA loading plots (**Figures 4.2B and 4.2E**) show the influence of each spectral bin in differentiating aCRPC and t-SCNC. The s-shaped loading plots indicated the top 10% spectral bins that contributed the most in differentiating the groups, starting from those with the greatest influence: 3.21, 3.24, 3.55, 3.22, 3.02, 1.33, 3.43, 3.74, 3.93, 1.30, 3.96, 4.18, 4.02, 1.93, 1.46, 2.33, 2.58, 1.58, and 5.38 ppm (**Figure 4.2C**). These spectral bins correspond to metabolites such as unlabeled lactate, ^{13}C-lactate, alanine, ^{13}C-alanine, glutamate and ^{13}C-glucose. aCRPC and t-SCNC groups were again differentiated with 95% confidence using PCA (**Figure 4.2C**) for PDX extracts labeled with [U-^{13}C]glutamine. Based on the PCA loading plots (**Figure 4.2E**) and s-shaped loading plots (**Figure 4.2F**), the top 10% spectral bins that had the greatest contribution in differentiating the tumor groups, starting from those with the greatest influence, were: 3.93, 3.27, 3.62, 3.05, 3.24, 3.55, 3.68, 2.15, 2.46, 3.30, 4.18, 4.02, 2.05, 2.30, 2.99, and 5.22 ppm (**Figure 4.2F**). These spectral bins include resonances from metabolites such as glutamate, ^{13}C-glutamate, glutamine,

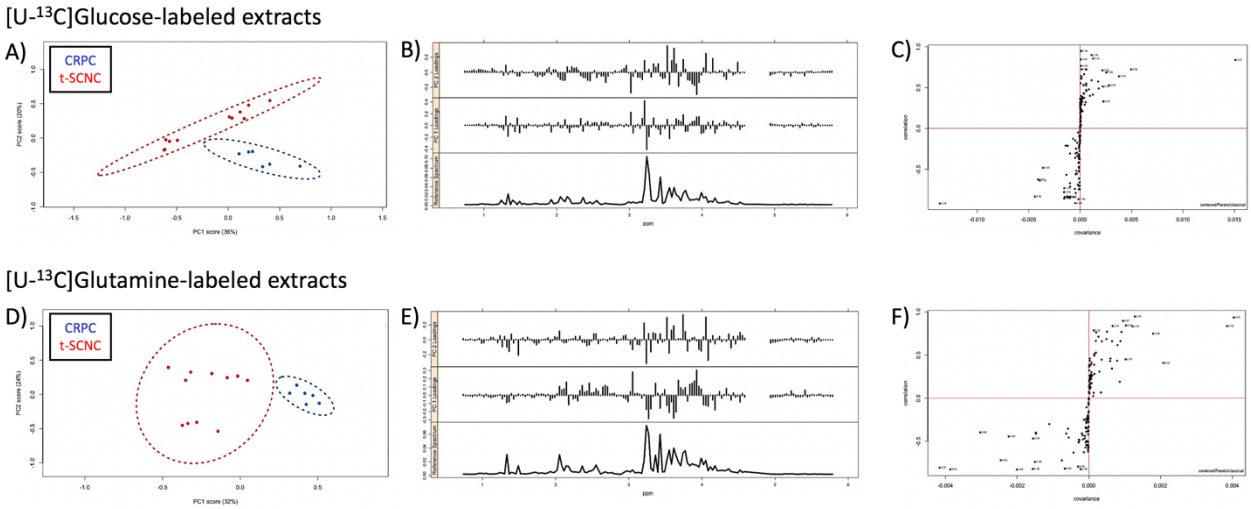

Figure 4.2. Principal Component Analysis performed on 1D proton spectra of aCRPC (LuCaP 77CR, LTL-313HR, N=6) and t-SCNC (LTL-352, LTL-610, LuCaP 93, LuCaP 145.1, N=12) extracts labeled with [U-^{13}C]glucose (top row: A,B,C) and [U-^{13}C]glutamine (bottom row: D,E,F). (A,D) PCA score plots with dotted ellipses indicate 95% confidence interval for classification, (B,E) PCA loadings score plots, and (C,F) PCA loading s-shaped plots.

^{13}C-glutamine, and glucose. Some of these spectral bins contained metabolites whose steady-state concentrations had been quantified in **Figure 4.1A**.

[U-^{13}C]glucose and [U-^{13}C]glutamine labeling studies demonstrate elevated glycolysis, TCA cycle metabolism, and glutaminolysis in t-SCNC compared to aCRPC

To understand which metabolic pathways were responsible for the PCA metabolic discrimination of aCRPC from t-SCNC, 2D ^{1}H-^{13}C HSQC spectra were acquired from **t-**SCNC versus aCRPC PDXs after [U-^{13}C]glucose- (**Figure 4.3A**) and [U-^{13}C]glutamine-labeling. The FE of glucose and glutamine metabolites was then calculated and summarized in **Figures 4.3B** and **4.3C,** respectively.

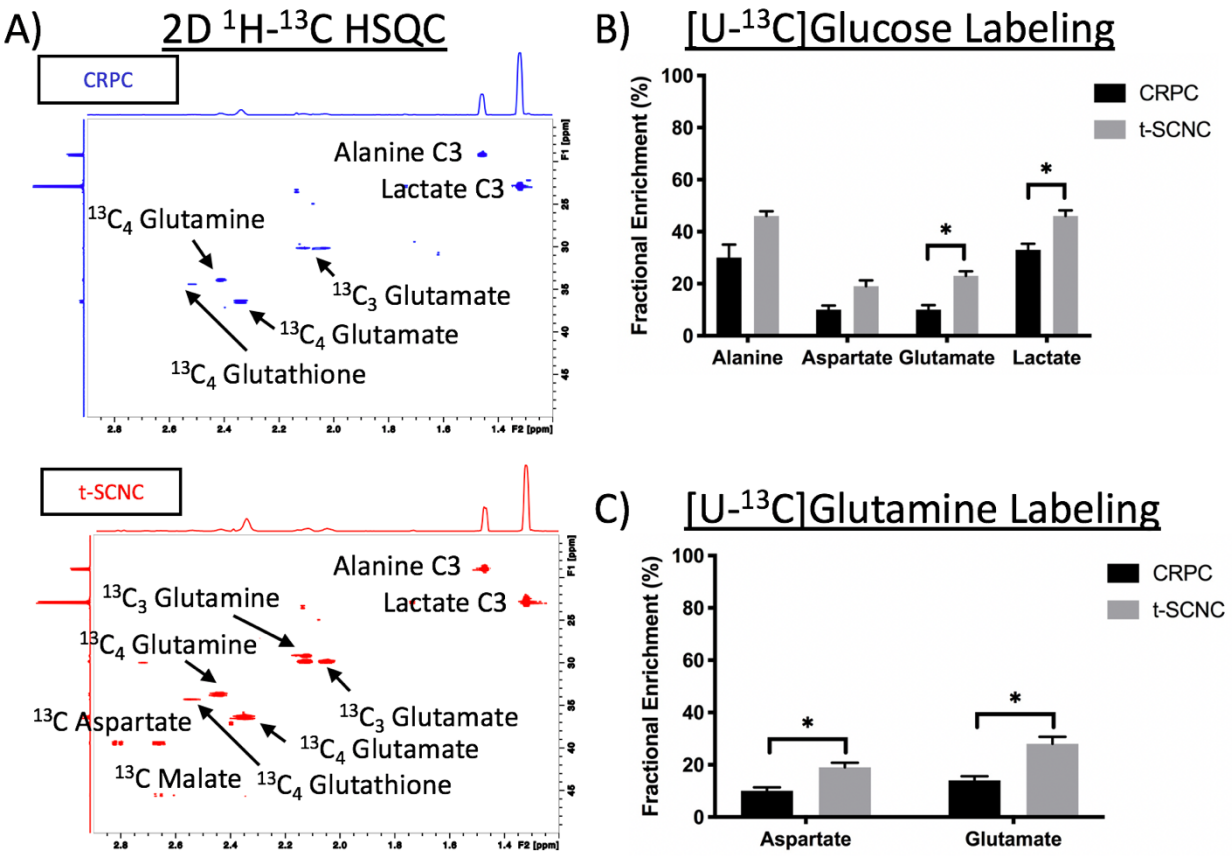

Figure 4.3. Fractional enrichment profiles of aCRPC and t-SCNC PDXs labeled with [U-^{13}C]glucose and [U-^{13}C]glutamine. (A) Representative spectra of 2D ^{1}H-^{13}C HSQC of aCRPC (LuCaP 77CR) and t-SCNC (LTL-352) tumor extracts after [U-^{13}C]glucose labeling. (B) After [U-^{13}C]glucose infusion, t-SCNC (LTL-352, LTL-610, LuCaP 93, LuCaP 145.1, N=12) tumors had significantly elevated alanine FE, glutamate FE, and lactate FE compared to aCRPC (LuCaP 77CR, LTL-313HR, N=6) tumors. (C) After [U-^{13}C]glutamine infusion, t-SCNC (LTL-352, LTL-610, LuCaP 93, LuCaP 145.1, N=12) tumors had significantly elevated aspartate FE and glutamate FE compared to aCRPC (LuCaP 77CR, LTL-313HR, N=6) tumors.

Following [U-^{13}C]glucose infusion, t-SCNC tumors compared to aCRPC tumors had elevated lactate FE (46±2 vs 30±2, $p<0.05$), glutamate FE (23±2 vs 9±3, $p<0.05$) and aspartate FE (19±2 vs 12±2, $p=0.06$) (**Figure 4.3B**), suggesting that t-SCNC has significantly increased glycolytic flux and up-regulated utilization of glucose in TCA metabolism. These findings are consistent with published transcriptomic and proteomic studies which show that t-SCNC PDXs

have elevated glycolysis and OXPHOS compared to prostatic adenocarcinoma PDX models[187,188].

Following [U-^{13}C]glutamine infusion, t-SCNC compared to aCRPC tumors had elevated aspartate FE (20±2 vs 9±2, $p<0.05$) and glutamate FE (30±3 vs 14±2, $p<0.05$) (**Figure 4.3C**), suggesting that t-SCNC tumors have elevated glutaminolysis and glutamine utilization in TCA metabolism.

4.5. Discussion

In this study, NMR-based ^{13}C-labeling studies and principal component analysis were performed to compare the metabolic profile of aCRPC and t-SCNC using LuCaP and LTL PDX models. As depicted in **Figure 4.4**, t-SCNC PDXs had significantly elevated flux of glucose through glycolysis and TCA metabolism, as well as elevated flux of glutamine through glutaminolysis and TCA metabolism, compared toa CRPC PDXs. This is consistent with our hypothesis that these pathways are upregulated in t-SCNC due to increased MYC expression[171]which upregulates both glutamine transport into the cell via SLC1A5 as well as glutaminase conversion of glutamine to glutamate via glutaminase[189,190]. The increase in glutamine metabolism is also partially driven by the need for anaplerotic substrates to replenish TCA cycle intermediates being used to support biosynthesis of macromolecules (e.g,. nucleotides, proteins, and lipids) that are necessary for rapid cellular proliferation[149,191].

An interesting finding is that PCA of 1D proton spectra can be used to differentiate the two phenotypes. Furthermore, the influence of glucose and glutamate bins played an important role in differentiating aCRPC from t-SCNC using PCA analysis even though the steady-state concentrations of these metabolites were not significantly different. This suggests that PCA is

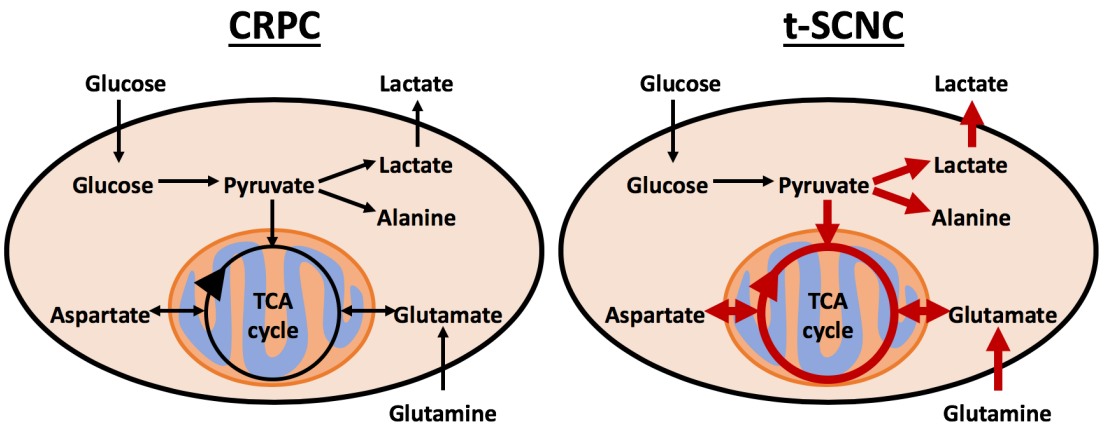

Figure 4.4. Schematic detailing the metabolic alterations observed between aCRPC and t-SCNC tumors.

better at differentiating aCRPC from t-SCNC than steady state metabolic profiling, likely due to the ability of PCA to pick up more information with less bias than manual spectral processing. Future work will integrate other pre-processing techniques such as peak alignment to correct for peak shifts due to variations in pH and temperature between samples. Instead of traditional fixed binning used in this work, adaptive binning methods will be used to minimize the variability in integrated bin intensities by preventing peaks from different metabolites within each bin and ensuring that the same peaks are consistently within the same bin boundaries between samples. Additional PCA analysis on unlabeled PDX tissues will also provide further insight into the robustness of our findings.

A limitation of this study was that only two aCRPC PDX models were studied in comparison to four t-SCNC models. Ongoing work is being performed to include additional aCRPC PDX models to the analysis. Another limitation is the inherent insensitivity of NMR, which prevents characterization of low-concentration intermediates of glycolysis, pentose phosphate pathway, the TCA cycle, and fatty acid metabolism. Future studies will use mass spectrometry, which is several orders of magnitude more sensitive than NMR, in order to fully

characterize the metabolic alterations associated with small cell neuroendocrine differentiation in prostate cancer.

In conclusion, unique metabolic alterations in glucose and glutamine metabolism were identified between aCRPC and t-SCNC PDXs. Stable isotope labeling methods demonstrated that glycolysis, TCA metabolism of pyruvate and glutamine, and glutaminolysis was upregulated in t-SCNC PDXs. These results support the use of hyperpolarized [1-^{13}C]pyruvate to assess glycolysis, [2-^{13}C]pyruvate to assess TCA metabolism, and [5-^{13}C]glutamine to assess glutaminolysis as non-invasive imaging biomarkers. Imaging biomarkers or drugs targeting these pathways could greatly improve the diagnosis and treatment of patients with aCRPC and t-SCNC. Future work will focus on whole transcriptome analysis as well as an integrated metabolomic and transcriptomic models to confirm the underlying basis of the metabolic alterations observed in this study.

CHAPTER FIVE

Metabolic Comparisons of Patient-Derived Models of Renal Cell Carcinoma using NMR and Hyperpolarized ^{13}C MRI

5.1. Abstract

This pilot study investigated the metabolic changes that occur when tissues or cells from a renal cell carcinoma (RCC) patient-derived xenograft (PDX) are propagated in culture. High-resolution NMR and hyperpolarized ^{13}C MRI studies showed that RCC PDX tumors and tissue slice cultures (TSCs) had similar metabolic flux profiles, with the majority of glucose being converted to lactate via glycolysis and less glucose being converted to glutamate via the TCA cycle. PDX tumors appeared to be more proliferative than TSC and cell cultures based on elevated choline concentration, and had higher redox capacity based on elevated glutathione and 3-hydroxybutarate concentrations. Furthermore, PDX-derived cells grown in hypoxic conditions had elevated glucose flux through glycolysis and alanine synthesis and reduced glucose flux through the TCA cycle compared to cells grown in normoxic conditions. Finally, hyperpolarized [1-^{13}C]pyruvate and [1-^{13}C]dehydroascorbate can be used to assess glycolysis and redox capacity in real time by performing dynamic HP ^{13}C MR studies using a NMR-compatible TSC bioreactor and a PDX model. The results of this study increase our understanding of the attributes and limitations of each of the model systems for studying the metabolic underpinnings of RCC.

5.2. Introduction

Renal cell carcinoma (RCC) is the most common type of kidney cancer and one of the top 10 malignancies in the United States, with ~50,000 Americans diagnosed each year and ~14,000 deaths[12]. Over the past 30 years, there has been a consistent increase in the diagnosis of RCC with no decline in mortality. Metastatic RCC remains an incurable disease due to over-diagnosis and over-treatment of clinically insignificant disease and lack of reliable diagnostic tools to detect aggressive tumors at a curable stage[38]. While several therapies targeting VEGF

and mTOR signaling pathways and an immune checkpoint inhibitor are FDA-approved for the treatment of metastatic RCC[39], all patients eventually develop resistance. Therefore, there is a clinical need for early diagnosis of treatable disease, effective therapeutic targets, and diagnostic biomarkers of therapeutic response.

Hyperpolarized ^{13}C MRI is a new molecular imaging technique that allows rapid, safe and noninvasive surveillance of dynamic pathway-specific metabolic and physiologic processes. Hyperpolarization via dynamic nuclear polarization (DNP)[110], which provides >10,000-fold increase in sensitivity, enables noninvasive imaging of ^{13}C-labeled biomolecules that are endogenous, nontoxic, and nonradioactive. In order to develop novel diagnostic imaging biomarkers of disease progression, the metabolic phenotype of RCC must be characterized to understand which pathways are altered in RCC metabolism. This is typically done using preclinical models. However, a complete investigation of preclinical models is essential to ensure that preclinical findings are clinically relevant since metabolic regulation checkpoints that include cellular membrane transport, substrate activation as well as biochemical conversions can vary across tissues. Characterizing metabolic fluxes through glycolysis, glutaminolysis, and the tricarboxylic acid (TCA) cycle in patient-derived RCC models using HP ^{13}C MRI will therefore provide valuable data for clinical translation of HP molecular imaging for the care of RCC patients. In order to understand the mechanistic underpinnings of the changes in metabolic fluxes observed via HP ^{13}C MRI and to understand the complexity of changes in fluxes through metabolic pathways, which exist in varying stages of progression of renal cancer and their responses to therapy, good preclinical models and full supporting biologic data (immunohistochemical measurements, steady state metabolite labeling patterns, and corresponding enzyme expression and activity profiles) are necessary.

5.2.1. Metabolic alterations of renal cell carcinoma

Metabolic reprogramming is strongly implicated in the development and progression of RCC[192,193] and reflects the combined effect of genomic, transcriptomic, and proteomic alterations. Understanding how metabolism is dysregulated in RCC can help identify new diagnostic, prognostic, and therapeutic approaches to improve patient care. Most gene mutations commonly observed in RCC have a fundamental role in the regulation of cellular metabolic processes, including dysregulation of oxygen sensing, energy sensing and nutrient sensing signaling cascade pathways[194].

The most common type of RCC is clear cell RCC (ccRCC), accounting for ~80% of cases. This subtype is a genetically heterogeneous and complex disease[195,196], with high frequency of von Hippel-Lindau (*VHL)* gene mutations, leading to normoxic stabilization of hypoxia inducible factors (HIFs), and ubiquitous loss of fructose-1,6-biphosphatase (FBP1)[197]. These genetic aberrations result in upregulation of aerobic glycolysis, also known as the "Warburg effect"[198]. The extracellular acidification caused by this increased lactate production and export is hypothesized to promote tissue invasion and metastasis[199,200]. Additionally, expression of lactate dehydrogenase A (LDHA), which catalyzes the conversion of pyruvate to lactate, is a predictor of poor prognosis in ccRCC[201]. Similarly, the monocarboxylate transporter MCT4, which is responsible for lactate efflux, is a prognostic marker in ccRCC patients and correlates with pathological grade[202-204]. Together these findings suggest that evaluation of glycolytic metabolites may inform on ccRCC aggressiveness.

Other metabolic pathways are also altered in ccRCC. An *ex vivo* ^{1}H NMR study showed that ccRCC had elevated lactate, glutamate, pyruvate, glutamine and creatine, and decreased

acetate, malate and amino acids compared to normal kidney tissue, with stage-related differences[205]. Metabolomic profiling by LC/MS and GC/MS also showed grade-specific metabolic reprogramming[206-208]. Furthermore, The Cancer Genome Atlas (TCGA) identified several active transcriptional hubs in ccRCC that interlinked many of the transcriptional programs promoting glycolytic shifts based on gene mutation, copy number and mRNA expression data[209]. Specifically, cross-platform analyses indicated a correlation between worse prognosis and a metabolic shift toward increased dependence on the pentose phosphate shunt, decreased AMPK, decreased Krebs cycle activity, and increased glutamine transport and fatty acid production. This mirrors the Warburg metabolic phenotype (increased glycolysis, decreased AMPK, and glutamine-dependent lipogenesis) typically observed in cancer.

5.2.2. Preclinical models of renal cell carcinoma

Predictive preclinical RCC models including patient-derived xenografts (PDXs), tissue slice cultures (TSCs), and primary cell culture models are useful for to improving diagnosis, prognosis, and treatment of RCC patients in the clinic. Each model has its merits and drawbacks based on its utility and representation of important biological features (intact stromal architecture, microenvironment, tissue heterogeneity, gene expression and perseveration of mutations). Patient-derived models such as PDXs and organoids better represent patient disease and are preferred for preclinical drug development and biomarker discovery, but have low throughput. Traditional patient-derived cell lines and cell line-derived xenografts allow for high-throughput studies. However, these models often do not accurately reflect the disease state found

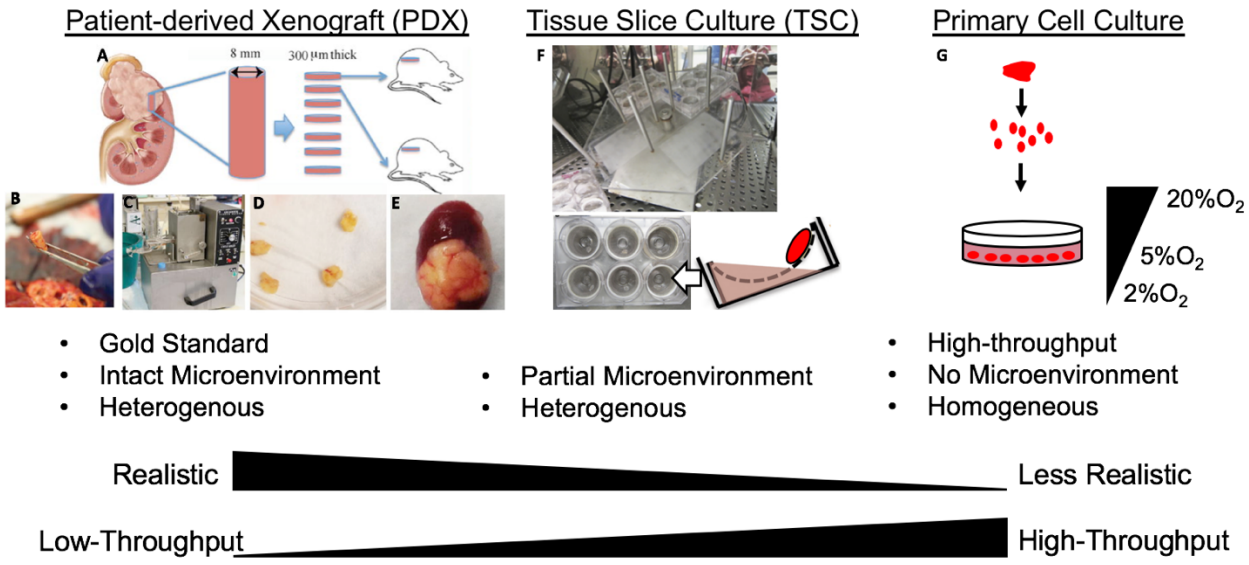

Figure 5.1. Model propagation from murine orthotopic tumors to tissue slice culture and primary cell culture. (A) Tissue core (8-mm diameter) aseptically bored from fresh nephrectomy specimen. (B) Core removed from specimen. (C) Tissue core mounted in Krumdieck tissue slicer and precision-cut at 300-µm. (D) RCC tissue slices ready for culture or implantation into mice. (E) RCC tissue slice implanted into the subrenal capsule of the mouse kidney. (F) RCC tissue slice culture in a specialized angled rotating plate. (G) Harvested PDX tumors were digested into single cells then established in primary culture. Cells were placed in incubators with 2%, 5%, and 20% oxygen overnight prior to ^{13}C-labeling studies.

in patients and are a major factor in the low success rate of oncogenic drug development[40,41]. Biological characterization of each model derived from the same parental tissue will help determine which *in vitro* and/or *in vivo* preclinical models to use for preclinical drug development and biomarker discovery studies.

This pilot study assessed the metabolic phenotypes of PDX, TSC, and primary cell culture models that were all derived from the same ccRCC patient tissue (**Figure 5.1**). These comparisons were performed to understand how key metabolic phenotypes are influenced by the microenvironment and growth conditions for each patient-derived RCC platform. Metabolism was assessed using NMR-based metabolomics and ^{13}C-glucose-labeling techniques as well as

hyperpolarized ^{13}C MRI. The results of this study can help accelerate studies on drug screening and biomarker discovery targeting metabolic pathways.

5.3. Materials and Methods

PDX Model

An RCC PDX was established from a fresh sample of a ccRCC metastasis to the colon with a VHL gene mutation as previously described[210]. Thin (~300-um), precision-cut tissue slices from cores of the fresh surgical specimen were implanted under the subrenal capsule (SRC) of $RAG2^{-/-}\gamma C^{-/-}$ mice (**Figure 5.1**). Second generation subrenal ccRCC PDX tumors were grown to ~0.8 cc (from T_2-weighted MRI) for [U-^{13}C]glucose labeling studies (N=3) and hyperpolarized ^{13}C MRI using [1-^{13}C]pyruvate (N=3) and [1-^{13}C]dehydroascorbate (N=4).

PDX-derived TSC Model

Second generation PDX tumors were precision-cut into thin (300-μm thick, 8-mm diameter) slices using a Krumdieck slicer, then cultured on grids in 6-well dishes on an angled rotator as previously described (**Figure 5.1-F**). TSCs were cultured in an atmospheric incubator (20% oxygen) in specialized medium[210,211] overnight for at least 12 hrs prior to ^{13}C-glucose labeling (N=3) and hyperpolarized ^{13}C bioreactor studies using [1-^{13}C]pyruvate (N=2).

PDX-derived Primary Cell Culture Model

Cells were harvested from second generation ccRCC PDX tumors using a protocol adapted from Young et al. (2013)[212]. Freshly harvested tissue was washed in phosphate-buffered saline (PBS), minced with scissors, and enzymatically digested for 30 min in DMEM

supplemented with 200 units/mL collagenase type I, 1 U/mL DNase I, 2 uM Y027632, 10% fetal bovine serum, and 1% penicillin-streptomycin. Tissue solution was pipetted every 10 min to aid dissociation. Tissue digestion was halted once clusters of cells were visible under the microscope prior to complete digestion to single cells. Digested tissue was incubated with Red Cell Lysis buffer and filtered through 40 um cell strainers. RCC cells recovered after enzymatic digestion were established in primary culture under 2% oxygen using previously-described medium[213]. At passage 10, cells were placed in incubators with 2%, 5% and 20% oxygen overnight prior to ^{13}C-glucose labeling studies.

^{13}C-Glucose Labeling and Extraction of Cells and Tissue

For the PDX model, mice received bolus injection of 80 uL 25%wt/volume [U-^{13}C]glucose via tail vein every 15 min for a total of 45 min as previously described[49]. Tumor tissue was collected and flash-frozen in liquid nitrogen. For the TSC model, TSCs were cultured in specialized medium supplemented with 25 mM [1,6-$^{13}C_2$]glucose for 2 hrs, gently rinsed in cold PBS, then flash-frozen in liquid nitrogen. Frozen tissues from PDXs (33.6±3.2 mg) and TSCs (104±3.3 mg) were homogenized in 400 µL cold methanol using a Tissuelyser LT at 4°C. For the primary cell culture model, cells (3.5±0.2 million) were incubated in DMEM containing 25 mM [1,6-$^{13}C_2$]glucose for 6 hrs at 37°C with 2%, 5%, and 20% oxygen. Cells were rinsed in cold PBS then directly quenched using cold methanol then scraped. Metabolites were extracted from the aqueous layer of cold 1:1:1 methanol:water:chloroform[68,214]. The aqueous layer was separated, lyophilized and resuspended in D_2O for NMR analysis. The protein layer was frozen at -80°C for protein quantification using a standard Bradford assay.

NMR acquisition

High-resolution NMR spectra were acquired on an 800 MHz Bruker AvanceI equipped with a 5 mm triple resonance TXI cryoprobe. *^{13}C-decoupled ^{1}H presaturation pulse*: α=90, TD=24k, SW=15 ppm, TR=12 seconds, AQ=0.5 seconds, NS=32. Water signal was suppressed using a presaturation pulse. Adiabatic decoupling was applied during acquisition using a CHIRP pulse with 54 kHz sweep width (equivalent to 200 ppm @ 800 MHz), and shaped pulse power level of +2 dB with respect to the power level determined for ^{13}C-GARP. Total scan time was 6 min. *^{1}H-^{1}H TOCSY*: 2D TOCSY with presaturation was used with the following parameters: TD=4096x512, SW=12x12 ppm, TR=2 seconds, AQ=0.239 seconds, NS=8, t_{mix}=60 milliseconds. Total scan time was 2 hours 45 minutes. Data were zero-filled in both dimensions to a final digital resolution of 9.4 Hz/point in the F2 dimension. *^{1}H-^{13}C HSQC*: A phase-sensitive 2D HSQC (hsqcgpph) with no ^{13}C decoupling during acquisition was used with the following parameters: TD=2048x4096, SW=6x120 ppm, TR=1.5 seconds, AQ = 0.297 seconds, NS=2, J_{CH} = 135 Hz (average J_{CH} of 127, 130, and 145 Hz for glutamate C2, C3, and C4). Data were zero-filled in both dimensions to a final digital resolution of 2.9 Hz/point in the F2 dimension. Total scan time was 4 hours.

NMR quantification

1D NMR datasets were processed using ACD/1D NMR Processor (version 9). The datasets were zero-padded by a factor of 2, apodized with a 0.5 Hz exponential filter, and manually phased and baselined. Peaks of interest were automatically fit using a Lorentzian-Gaussian shape function. 2D NMR datasets were processed using TopSpin (version 3.5). 2D datasets were zero-padded by a factor of 2, manually phased, and peak volumes were integrated.

For cells, intracellular and extracellular metabolite concentrations were quantified from ^{1}H presaturation spectra of unlabeled cell extracts. For tissues, total metabolite concentrations were quantified from ^{13}C-decoupled ^{1}H presaturation spectra of ^{13}C-labeled tissue extracts.

Fractional enrichment (FE) was quantified as [^{13}C-labeled metabolite]$_{HSQC}$/[total metabolite]$_{\{13C\}1H}$. Total metabolite concentrations for all other metabolites were quantified using ^{13}C-decoupled ^{1}H spectra by manually fitting peaks of interest using a Lorentzian-Gaussian shape. The concentration of ^{13}C-labeled metabolites was quantified using ^{1}H-^{13}C HSQC by integrating the volumes of the cross-peaks, and correcting for incomplete polarization transfer using **Equation 2.3** as previously described in Chapter 2. Glutathione FE from [U-^{13}C]glutamine-labeling studies was quantified using ^{1}H-^{1}H TOCSY by integrating the peak volumes of the ^{13}C-satellites and the central unlabeled peak.

Hyperpolarized ^{13}C MRI of RCC TSC model using NMR-compatible bioreactor

Tissue slices were maintained at physiological conditions in a NMR-compatible bioreactor in circulating medium at 37°C perfused with 95% air/5% CO_2 using a gas exchanger as previously described[107]. All bioreactor experiments were performed using a 500 MHz Varian Inova (Varian, Palo Alto, CA, USA) with a 5 mm tripe-resonance direct-detect probe at 37°C. Approximately 7.5 μL of 14.2 M [1-^{13}C]pyruvate with 15 mM trityl radical (GE Healthcare, Waukesha, WI, USA) was polarized on a Hypersense polarizer (Oxford Instruments, Oxfordshire, England) for 1 hr followed by dissolution in 5 mL of 50 mM phosphate buffer with 0.3 mM EDTA, as previously described[215], to obtain physiologic temperature of 37°C and pH of 7.5. Dynamic ^{13}C NMR (30°flip, TR 3s) was acquired after infusion of 750 μL solution into the bioreactor over 90 sec injection time. Peak areas were fitted using MestreNova to calculate the

lactate-to-pyruvate (Lac/Pyr) ratio.

Hyperpolarized ^{13}C MRI of RCC PDX model

MR imaging of mice bearing PDXs was performed on a 3T Bruker BioSpec (Bruker). T_2-weighted ^{1}H anatomical MR images were acquired in sagittal, axial, and coronal views. Approximately 24 μL of 14.2 M [1-^{13}C]pyruvate with 15 mM trityl radical (GE Healthcare, Waukesha, WI, USA) was polarized on a Hypersense polarizer (Oxford Instruments, Oxfordshire, England) for 1 hr as described previously[21] followed by dissolution in 4.5 mL 50 mM phosphate buffer with 0.3 mM EDTA and equivalents of NaOH (80 mM) to obtain physiologic temperature and pH. The ^{13}C data were acquired 15 sec after start of injection of 500 μL hyperpolarized solution over 12 sec using 2D dynamic chemical shift imaging (CSI) with spiral encoding (8mm slab thickness, 10° flip, TR 4s, 32mm FOV). Approximately 32 μL of 2.2 M [1-^{13}C] dehydroascorbate (DHA) containing 15 mM trityl radical was polarized on a Hypersense polarizer (Oxford Instruments, Oxfordshire, England) for 1 hr as described previously[216] followed by dissolution in 3.5 mL distilled water with 0.3 mM EDTA. The ^{13}C data were acquired 20 sec after start of injection of 500 μL hyperpolarized solution over 12 sec using 2D dynamic CSI (8 mm slab thickness, 30° flip, TR 4s, 32x32 mm^2 FOV). Peak areas were fitted using MestreNova to calculate the lactate-to-pyruvate (Lac/Pyr) ratio for [1-^{13}C]pyruvate studies and the ascorbate-to-DHA (VitC/DHA) ratio for [1-^{13}C] DHA studies.

Histopathological Analysis

Tissues were fixed in 10% buffered formalin overnight, transitioned into ethanol and embedded in paraffin blocks. Tissue blocks were cut on a Leica microtome then dried onto glass

slides and stained using standard protocols for hematoxylin- and -eosin (H&E) and immunohistochemistry for a human-specific marker (Ku70) and ccRCC biomarkers (CAIX, PAX8, CD10, and CD117) (**Figure 5.2**).

Oxygen Consumption

Basal oxygen consumption rate (OCR) was measured using a Clark-type O_2 electrode (Oxygraph+, Hansatech Instruments). Freshly harvested PDX (10.3±.5 mg) and TSC (33±2.4 mg) tissues was placed in a chamber with 1 mL serum-free DMEM at 37°C and respiration was assessed over 1 min. Control traces of medium without tissue were acquired after each sample to assess oxygen consumption attributed to the electrochemistry of the Clark electrode.

Statistics

Student's *t*-test was used to compare RCC models using Prism version 8.3. All statistics are reported as mean ± standard error. P-values less than 0.05 (*p <0.05, **p <0.01 and ***p <0.001) were considered significant. P-values above 0.05 were considered non-significant (n.s.).

5.4. Results

5.4.1. Validation of PDX models

The immunohistologic phenotypes and VHL gene mutation status of PDX, TSC, and cell culture models derived from the same RCC tumor were characterized. As shown in **Figure 5.2**, each model maintained similar histologic phenotypes and retained the same VHL gene mutation as the parental tumor. All models stained positive for Ku70, confirming the human origin of each. The ccRCC phenotype was confirmed based on positive stain of CAIX, PAX8 and CD10

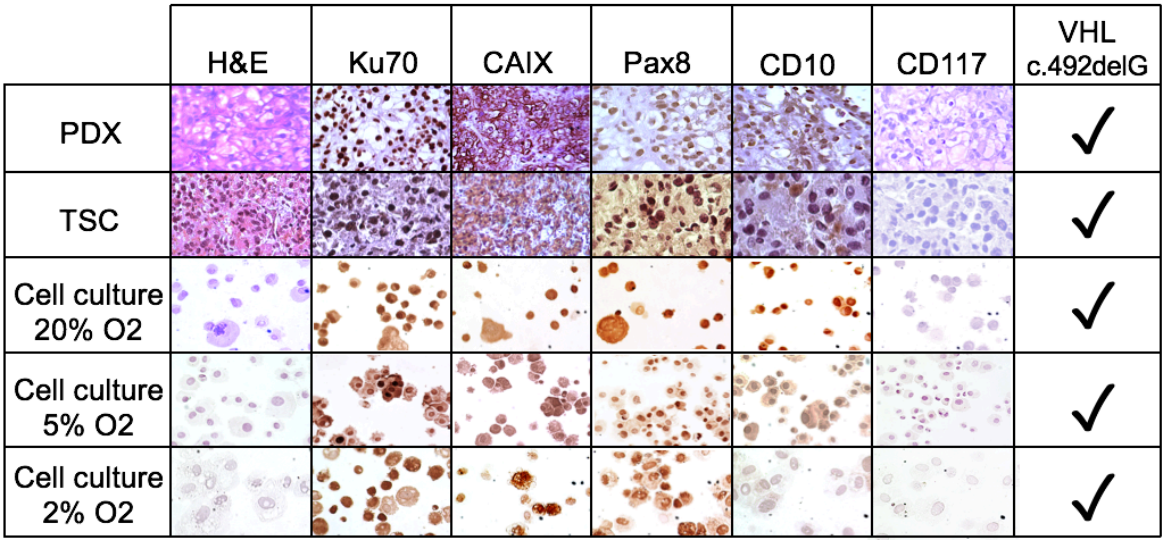

Figure 5.2. Immunohistology and VHL gene mutation status of patient-derived RCC models.

and negative stain of CD117, which are standard clinical markers of ccRCC. PDX and TSC models preserved the native tissue architecture and functional differentiation, maintained cellular heterogeneity and an intact microenvironment.

5.4.2. Characterization of ^{13}C-glucose metabolism using high-resolution NMR

The metabolic changes that occurred as the PDX model was propagated in TSC and primary cell culture at varying O_2 levels was assessed using high-resolution NMR techniques and hyperpolarized ^{13}C MRI. The following metabolic parameters were studied: steady-state metabolite concentrations, ^{13}C fractional enrichment in tissues labeled with ^{13}C-glucose, OCR, hyperpolarized Lac/Pyr ratio, and hyperpolarized VitC/DHA ratio.

Metabolic profiling showed significant differences between patient-derived RCC models

First, steady-state metabolite concentrations quantified from 1D proton NMR spectra (**Figure 5.3**) indicated large differences between the RCC PDX orthotopic tumor tissues, PDX-

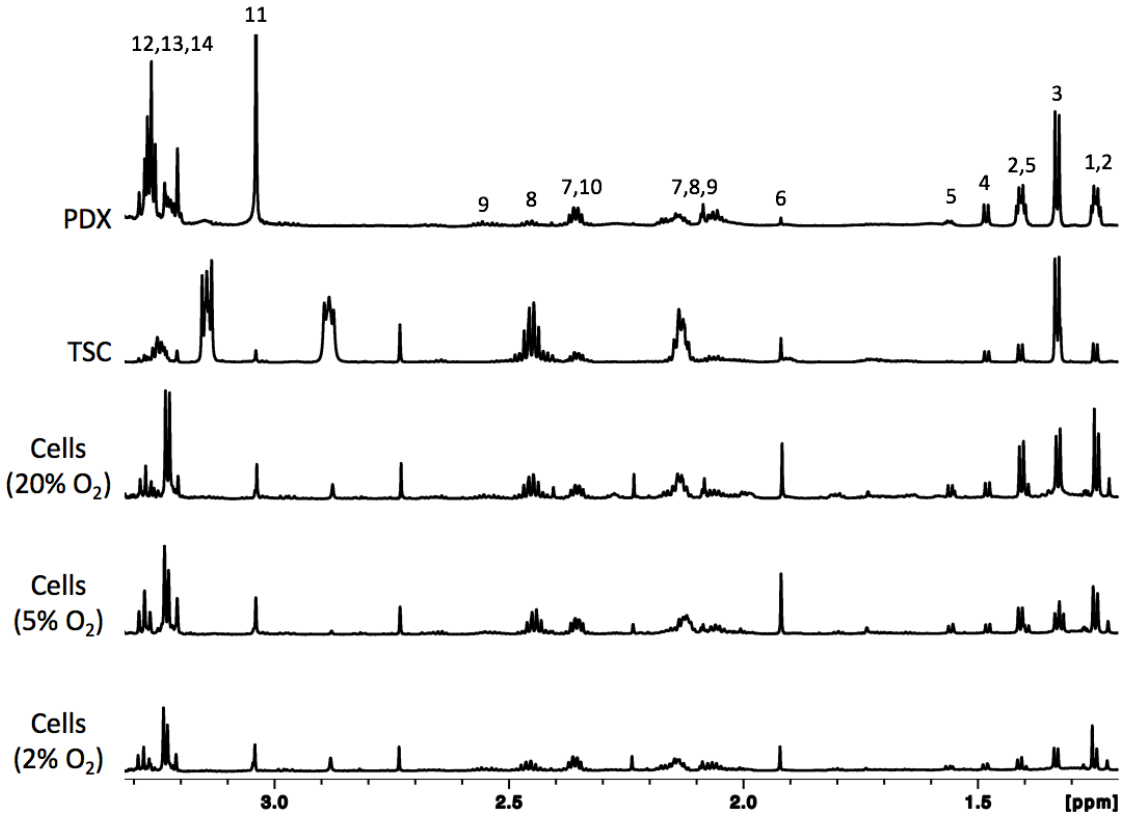

Figure 5.3. Representative 1D proton NMR spectra of patient-derived RCC models. Spectral intensity was normalized to mg protein. Metabolite peaks were assigned as follows: 1. 3-Hydroxybutyrate, 2. ^{13}C-Lactate, 3. Lactate, 4. Alanine, 5. ^{13}C-Alanine, 6. Acetate, 7. Glutamate, 8. Glutamine, 9. Glutathione, 10. Succinate, 11. Creatine, 12. Choline, 13. Phosphocholine, 14. Glycerophosphocholine

derived tissues sliced and cultured in an atmospheric incubator, and primary cell cultures derived from the PDX and grown in varying pO_2 levels. (**Table 5.1**).

PDX vs. TSC: Compared to the PDX-derived TSC, the PDX had increased concentrations of 3-hydroxybutyrate (5-fold, $p<0.05$), aspartate (2-fold, n.s.), choline (1.5-fold, n.s.), creatine (25-fold, $p<0.05$), creatine phosphate (4-fold, n.s.), glutamate (3-fold, n.s.), glutathione (2-fold, n.s.), glycerophosphocholine (1.75-fold, n.s.), lactate (1.3-fold, n.s.), and phosphocholine (1.9-fold, n.s.) concentrations. In addition, the PDX had reduced concentrations of acetate (5-fold, $p<0.05$),

glutamine (25-fold, $p<0.05$), isoleucine (4-fold, n.s.), leucine (4-fold, n.s.), succinate (2-fold, n.s.), and valine (1.3-fold, n.s.) compared to the PDX-derived TSC.

PDX vs. cells: Compared to PDX-derived primary cell cultures grown at atmospheric oxygen level (20%), the PDX had higher concentrations of 3-hydroxybutyrate (1.5-fold, $p<0.05$), aspartate (2-fold, n.s.), choline (2-fold, $p<0.05$), creatine (40-fold, $p<0.05$), creatine phosphate (5-fold, n.s.), glutamate (1.3-fold, n.s.), glutathione (5-fold, n.s.), glycerophosphocholine (1.75-fold, n.s.), lactate (3-fold, $p<0.05$), and phosphocholine (1.3-fold, n.s.). Compared to cultured cells grown in low oxygen conditions, the PDX had higher concentrations of hydroxybutyrate (4-fold, $p<0.05$), choline (2-fold, $p<0.05$), creatine (40-fold, $p<0.05$), creatine phosphate (5-fold, n.s.), glutamate (2-fold, n.s.) glutathione (7-fold, n.s.), glycerophosphocholine (1.75-fold, n.s.), lactate (4-fold, $p<0.05$), and phosphocholine (1.5-fold, n.s.).

TSCs vs. cells: Compared to cells grown at atmospheric oxygen levels, TSCs had higher concentrations of acetate (3-fold, n.s.), glutamine (16-fold, $p<0.05$), choline (3-fold, n.s.), glutathione (3-fold, $p<0.01$), isoleucine (3-fold, n.s.), lactate (2.5-fold, n.s.), leucine (5-fold, n.s.), succinate (4-fold, n.s.), and valine (1.5-fold, n.s.).

Cells cultured in varying oxygen levels: Cells grown at 2% oxygen had 50% lower glutamine concentration ($p<0.05$), 60% lower glycerophosphocholine (n.s.) and 66% lower total choline ($p<0.05$) levels than cells grown at 5% and 20% oxygen. This reduction in oxidative metabolism (glutamate) and proliferation (choline compounds) is consistent with what has been observed in

Table 5.1. Metabolic profiling of patient-derived RCC models. Metabolite concentrations (nmol/mg protein) are reported as mean ± standard error (SE) are displayed for each model with N=3 for all groups. Total choline is the summed concentration of choline, phosphocholine, and glycerophosphocholine.

	PDX			TSC			Cells (20% O_2)			Cells (5% O_2)			Cells (2% O_2)		
Metabolite	Mean	±	SE	Mean	±	SE	Mean	±	SE	Mean	±	SE	Mean	±	SE
3-Hydroxybutyrate	52.7	±	7.8	9.8	±	4.6	20.0	±	5.8	12.4	±	3.9	15.0	±	5.7
Acetate	41.5	±	9.0	197.3	±	53.2	57.8	±	0.7	60.5	±	24.4	43.4	±	11.7
Alanine	126.2	±	43.1	90.0	±	30.0	90.0	±	19.8	67.2	±	16.0	46.8	±	9.7
Aspartate	38.7	±	11.6	17.2	±	2.1	15.6	±	6.0	9.8	±	2.3	9.5	±	2.5
Choline	47.1	±	9.5	32.2	±	9.4	20.2	±	10.9	18.8	±	1.7	9.1	±	3.3
Citrate	18.5	±	4.6	17.1	±	2.1	12.1	±	5.4	7.0	±	0.9	7.7	±	2.4
Creatine	1216.5	±	286.5	47.1	±	18.2	25.5	±	1.9	30.2	±	9.0	19.8	±	5.4
Creatine phosphate	56.8	±	22.5	14.0	±	5.3	8.3	±	1.9	7.6	±	3.7	11.7	±	4.0
Glutamate	443.5	±	138.6	324.0	±	96.0	348.6	±	94.4	222.6	±	40.4	181.2	±	56.5
Glutamine	107.9	±	36.8	2459.4	±	744.5	161.2	±	8.3	153.7	±	31.9	74.8	±	21.5
Glutathione	137.1	±	56.6	65.7	±	8.2	24.6	±	9.4	17.6	±	0.8	19.4	±	6.9
Glycerophosphocholine	70.1	±	30.8	40.8	±	21.5	40.3	±	5.5	40.9	±	9.3	25.0	±	6.2
Isoleucine	15.2	±	2.1	63.3	±	18.7	24.2	±	3.1	15.7	±	2.9	7.6	±	2.6
Lactate	1280.5	±	154.1	966.4	±	232.1	476.2	±	5.3	281.7	±	46.4	158.2	±	58.1
Leucine	37.8	±	6.8	154.0	±	46.2	28.9	±	6.2	18.2	±	3.0	9.9	±	3.4
Phosphocholine	53.8	±	19.1	29.4	±	9.1	42.1	±	1.3	29.4	±	5.9	22.7	±	7.4
Succinate	10.4	±	3.7	23.6	±	10.5	5.7	±	1.8	2.4	±	0.6	2.4	±	1.1
Total Choline	215.6	±	91.8	102.5	±	38.7	91.7	±	6.6	88.7	±	10.0	58.5	±	0.8
Valine	30.1	±	4.6	45.6	±	13.6	26.6	±	5.9	15.9	±	3.0	9.6	±	3.3

cells grown in hypoxic conditions[214,217-219]. Interestingly, cells grown at 2% oxygen had lower lactate concentration (3-fold, $p<0.05$) than cells grown at 20% oxygen.

[U-^{13}C]glucose labeling studies of patient-derived RCC models

Stable isotope tracing using ^{13}C-glucose was used to compare the utilization of glucose between each model. Although the FE of metabolites measured in PDXs cannot be directly compared with that of TSC and cell models due to the differences in duration/mode of labeling, the metabolic flux profile can provide insight on the metabolic phenotypes of each model. PDX (**Figure 5.4A**) and TSC (**Figure 5.4B**) models had similar metabolic flux profiles. Lactate had the highest FE in both PDX (60±1, N=3) and TSC (13±4) models. Alanine FE was the second highest in PDX (26±7, N=3) and TSC (8±3) models. TSCs had relatively lower glutamate FE (1.6±0.4 vs 13±5, N=3) and OCR (0.10±0.003 vs 0.59±0.16 nmol O_2/mL/min/mg tissue, N=3) than the PDX model, indicating a significant reduction in oxidative metabolism in the TSC model (**Figures 5.5**).

The primary cell model had a different metabolic flux profile compared to the PDX and TSC models, with alanine having higher fractional enrichment than lactate (**Figure 5.5C**). This may indicate that alanine synthesis may be important in supporting biosynthesis of

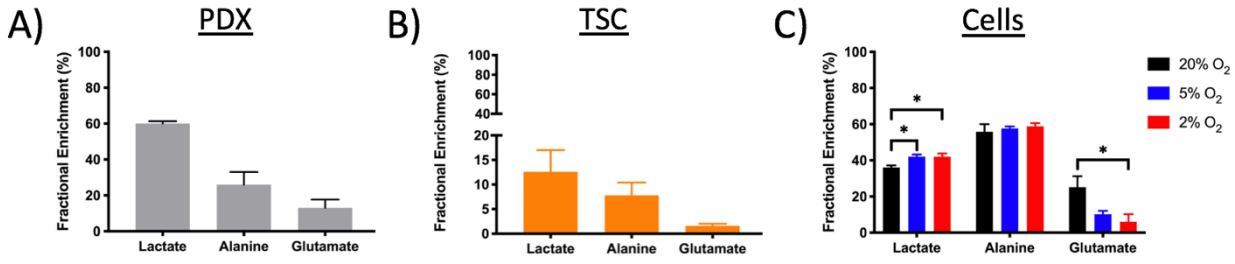

Figure 5.4. Fractional enrichment profiles of patient-derived RCC models. Fractional enrichment was quantified from (A) PDX labeled with [U-^{13}C]glucose for 45 minutes, (B) PDX-derived TSC labeled with [1,6-$^{13}C_2$]glucose for 2 hours, and (C) PDX-derived cells labeled with [1,6-$^{13}C_2$]glucose for 6 hours. N=3 for all groups. *$p<0.05$

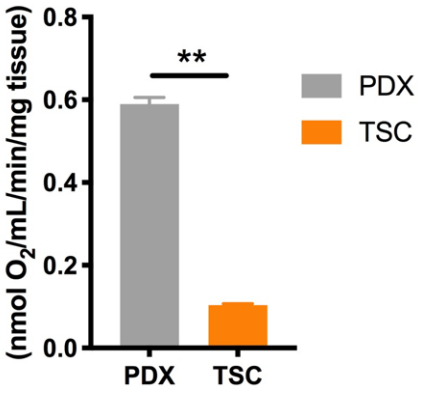

Figure 5.5. Oxygen consumption rate of TSC and PDX tissues. OCR was measured using a Clark-type O_2 electrode and normalized to wet tissue weight. **p<0.01 N=3 for all groups.

macromolecules in cell culture models compared to PDX and TSC models. Metabolic changes in response to hypoxic conditions were also observed using the primary cell model. Cells grown in 2% oxygen had significantly higher lactate FE (42±1 vs 36±1, N=3, p<0.05), indicating increased glycolytic activity, and significantly lower glutamate FE (6±4 vs 25±5, N=3, p<0.05), indicating suppressed TCA metabolism, compared to cells grown in 20% oxygen. Cells grown in 5% oxygen also had significantly higher lactate FE (42±1 vs 36±1, N=3, p<0.05) and lower glutamate FE (10±2 vs 25±5, N=3, p<0.10) than cells grown in 20% oxygen. No significant differences in fractional enrichment were observed between cells grown in 5% or 2% oxygen.

5.4.3. Characterization of glycolysis and redox capacity using hyperpolarized ^{13}C MRI

Hyperpolarized (HP) molecular imaging was used to noninvasively assess metabolism in real-time using RCC PDX and TSC models. Hyperpolarized studies on the TSCs were conducted using a homebuilt bioreactor (**Figure 5.6A**). Viability of the TSC model was confirmed by comparing the OCR of tissues in the bioreactor versus incubator. No significant difference in OCR was observed between the TSC perfused in the bioreactor and conventional culture in an

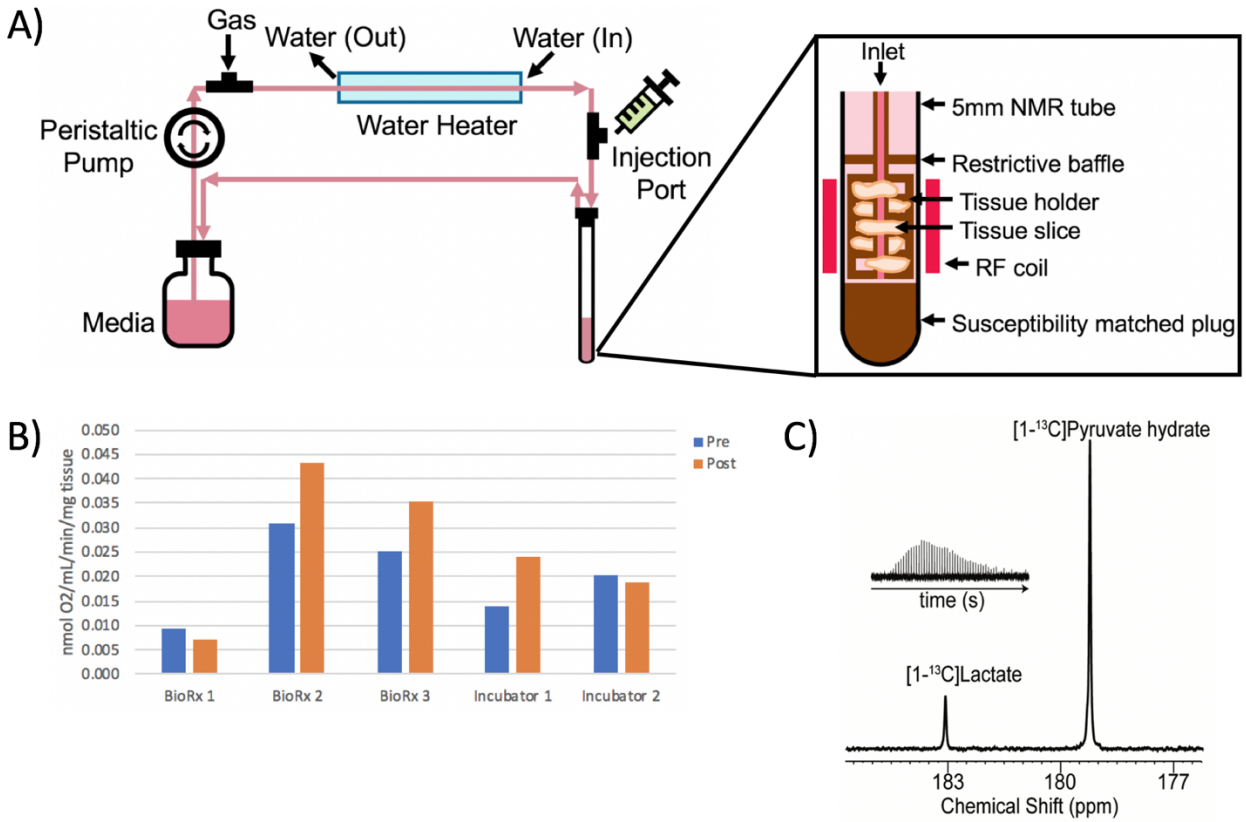

Figure 5.6. Hyperpolarized [1-^{13}C]pyruvate metabolism of RCC tissue slices in an NMR-compatible TSC bioreactor. (A) Schematic of NMR-compatible TSC bioreactor setup. (B) Oxygen consumption rates of tissue slices perfused in a homebuilt bioreactor and tissue slices cultured in a conventional incubator. Oxygen consumption was normalized to wet tissue weight. (C) Dynamic ^{13}C spectra after injection of [1-^{13}C]pyruvate into the TSC bioreactor acquired on a 500 MHz Varian Inova spectrometer.

incubator (**Figures 5.7B**). Hyperpolarized ^{13}C studies of TSC bioreactor revealed an average Lac/Pyr of 0.0048 (N=2) (**Figure 5.6C**).

Glycolysis was noninvasively assessed using hyperpolarized [1-^{13}C]pyruvate (**Figure 5.7A**). Pyruvate and lactate peaks within a tumor voxel were well resolved using 2D CSI (**Figure 5.7B**). There was a trend in correlation of Lactate/Pyruvate ratio (0.51±0.12, N=3) with LDH activity (48±8, N=2), which was independent of tumor volume (**Figure 5.7C**).

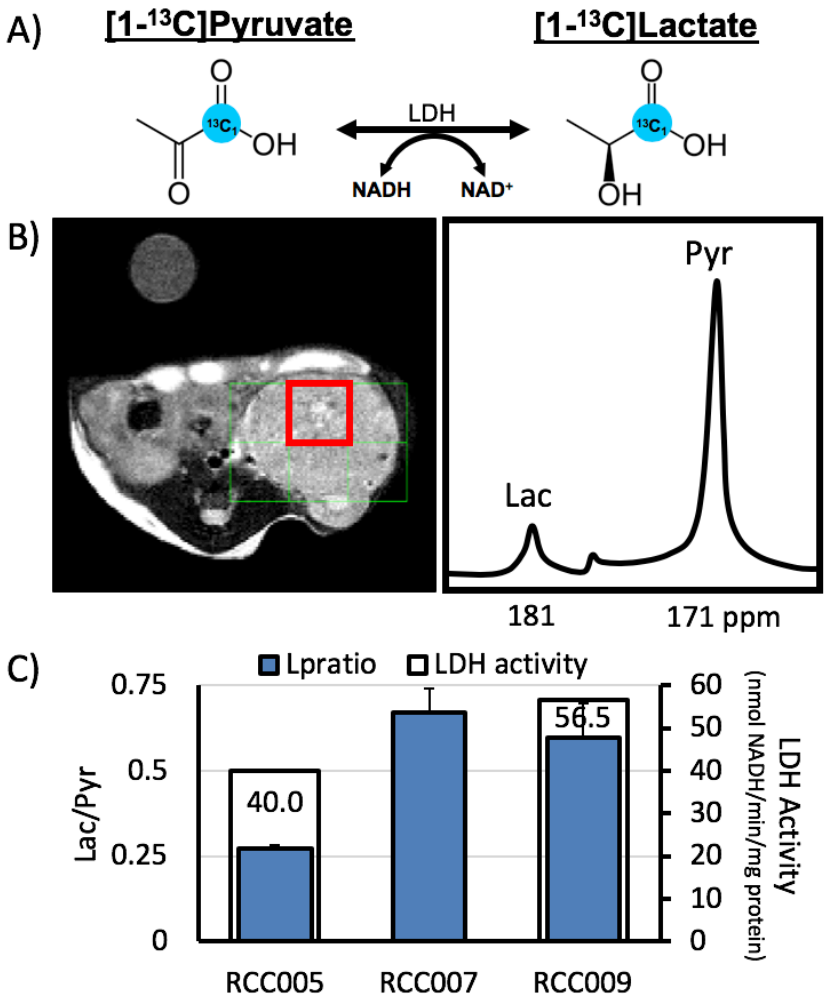

Figure 5.7. Hyperpolarized [1-^{13}C]pyruvate MRI and LDH activity using a RCC PDX model. A) Schematic of hyperpolarized [1-^{13}C]pyruvate conversion to [1-^{13}C]lactate. (B) T_2-weighted image with axial projection of 2D CSI of hyperpolarized [1-^{13}C]pyruvate in a mouse bearing a ccRCC PDX with corresponding spectrum of a tumor voxel with pyruvate (pyr) and lactate (lac) peaks labeled. (C) Lac/Pyr ratio and the corresponding LDH activity were measured to assess glycolytic activity. All tumors were ~0.85 cc. Lac = lactate, Pyr = pyruvate.

Redox capacity was noninvasively assessed using hyperpolarized [1-^{13}C]DHA. As depicted in **Figure 5.8A**, DHA is transported into cells and converted to ascorbate, also known as Vitamin C (VitC). Both DHA and VitC were resolvable using 2D CSI (**Figure 5.8B**). The VitC/DHA ratio was dependent on the tumor volume, indicating a need for higher redox capacity in larger tumors (**Figure 5.8C**).

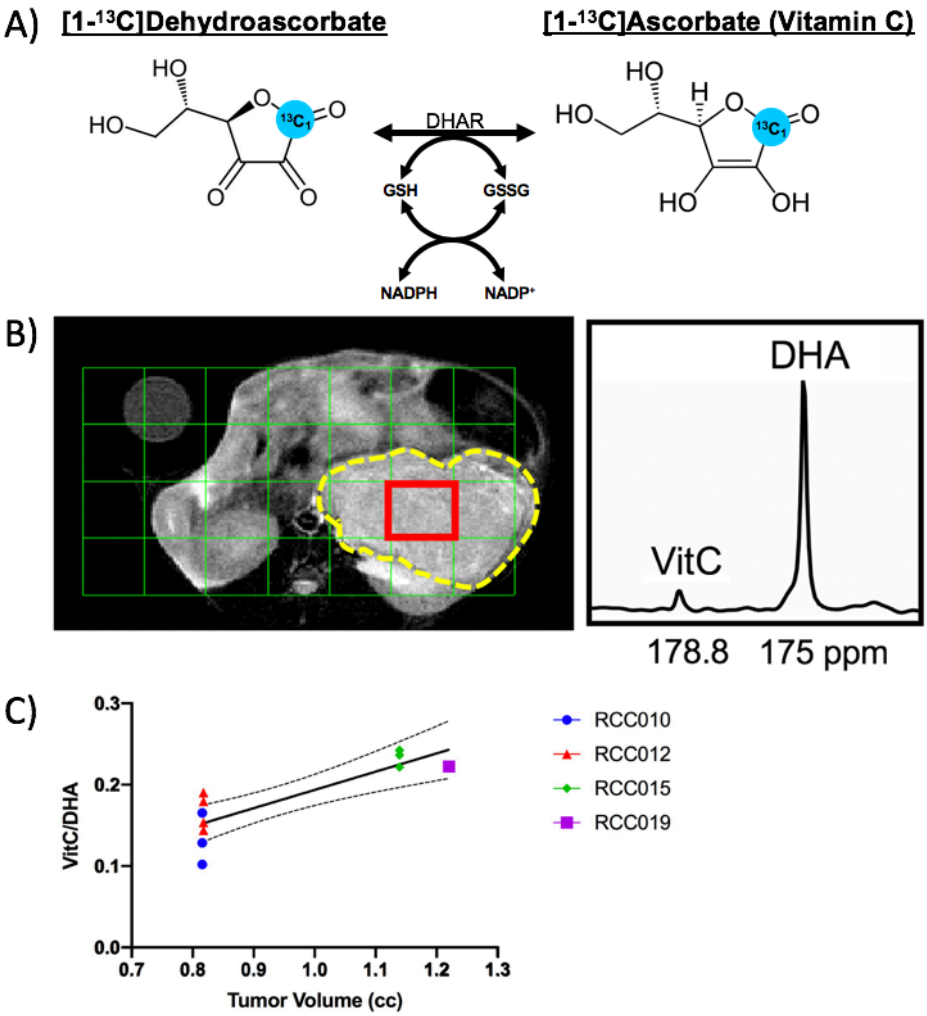

Figure 5.8. Hyperpolarized [1-^{13}C] dehydroascorbate MRI using a RCC PDX model. A) Schematic of hyperpolarized [1-^{13}C]dehydroascorbate (DHA) conversion to [1-^{13}C]ascorbate (VitC). (B) T_2-weighted image with axial projection of 2D CSI of hyperpolarized [1-^{13}C]dehydroascorbate (DHA) in an ccRCC PDX mouse with corresponding spectrum of a tumor voxel (red) with DHA and VitC peaks labeled. Tumor region of interest (ROI) is outlined in yellow. (C) Correlation between tumor volume and VitC/DHA ratio in mice bearing PDXs (N=3) was used to assess tumor redox capacity. VitC = ascorbate (Vitamin C). VitC/DHA ratio from each tumor voxel is displayed for each animal. DHA = dehydroascorbate.

5.4. Discussion and Conclusion:

In this study, NMR-based stable isotope tracing and hyperpolarized ^{13}C MRI were used to quantify the metabolic profile and assess redox capacity in several patient-derived RCC

preclinical models that had previously not been characterized nor directly compared with one another. Marked differences in metabolite concentrations and metabolic flux through glycolysis, alanine synthesis, and TCA cycle were observed among models. Some novel aspects of this study include the use of 3-D tissue slice culture and implementation of an NMR-compatible bioreactor for hyperpolarized ^{13}C studies.

Steady-state metabolic profiling showed that PDX tumors, with intact microenvironments, were more proliferative than TSC and cell models based on the significantly higher levels of total choline, which is a marker of proliferation, and creatine, which is a marker of energetic status that is catabolized to maintain elevated proliferation. The PDX model also had higher redox capacity based on the significantly elevated levels of glutathione, which is essential for protection against oxidative and nitrosative stress that arises from tumor microenvironment-related aggression or radiation. The PDX model also had elevated levels of 3-hydroxybutyrate, a ketone that serves as an alternative fuel source and indirectly protects against oxidative stress via inhibition of histone deacetylation and results in increased expression of oxidative stress resistance factors[220]. Together, this indicates that the PDX model is more suitable for testing the effects of radiation and other treatments targeting the redox pathway compared to the cell model, which has low redox capacity and thus is more susceptible to radiation. Stable isotope tracing with [U-^{13}C]glucose indicated that the PDX model was metabolically dependent on glycolysis instead of the TCA cycle. This may indicate that the PDX model is more dependent on anaplerosis to replenish TCA cycle intermediates[191].

An important finding of this study was that PDX and TSC models behaved similarly based on metabolic profiling and stable isotope tracing studies. The abnormally high levels of glutamine, isoleucine, lactate, and leucine in the TSC model may be an artifact of the culture

environment since the glutamate concentration is similar with the other models. The abnormally high levels of creatine and creatine phosphate may be an artifact of the subrenal capsule xenograft model since the kidney can absorb creatine from primary urine[221]. The low absolute fractional enrichments in TSCs compared to PDXs may be due to the lack of perfusion in the TSC model. However, the overall flux profile between PDXs and TSCs is similar with the majority of glucose being converted to lactate via glycolysis and very little glucose being converted to glutamate via TCA cycle. Compared to the PDX and TSC models, the primary cells had a drastically altered metabolic profile. This reflects the lack of cellular heterogeneity and microenvironment in the cell model.

Oxidative stress is often heterogenous in tumors *in vivo.* Tumors are hypometabolic under conditions of hypoxia and transform to highly oxidative under atmospheric conditions, with tumor metabolism rapidly switching between anaerobic glycolysis to carbohydrate oxidation[222]. This metabolic adaptation is also demonstrated in RCC cells grown *in vitro* under varying oxygen conditions. From the ^{13}C-glucose labeling study, cells grown in hypoxic conditions had elevated flux through glycolysis and alanine synthesis and suppressed glucose flux through the TCA cycle compared to cells grown in normoxic conditions. These metabolic alterations are consistent with the hypoxia-induced changes in glucose metabolism mediated by HIF1, which includes upregulation of almost all enzymes involved in glycolysis as well as the lactate transporter MCT4, and inactivation of the pyruvate dehygrogenase (PDH) complex and decreased pyruvate oxidation[223]. Cells grown under hypoxic conditions has suppressed levels of energy metabolites (acetate, alanine, glutamine, and lactate) and lower levels of total choline and creatine compared to cells grown in normoxic conditions, suggesting that the cells grown in hypoxic conditions had lower proliferation. Interestingly, it was necessary to culture primary

cells under hypoxic conditions (2% oxygen) to obtain efficient growth in early passages, with cells grown under atmospheric conditions only becoming viable in later passages. However, the metabolism of PDX tissues is better recapitulated by cells grown under atmospheric conditions, indicating maintenance of common metabolic pathways under these conditions.

Based on this study, the PDX model with its intact microenvironment is ideal for studies involving oxidative stress and perfusion, whereas the more high-throughput TSC and cell models may be more suitable for studies involving genetic alterations, hypoxia, and therapeutic drug screening. One caveat of the PDX model is that it lacks adaptive immune cells given its implantation into immunocompromised mice. Future work will focus on correlating these results with gene expression and biochemical assays. The genomic drivers underlying these metabolic changes are currently being investigated to further understand the metabolic transformations that occur in the different model systems. Based on the metabolic data and what has been shown in the literature, the PDX and TSC models may have similar global gene expression profiles, while the primary cell model will have the most altered gene expression profile. A key interest will be to integrate metabolomic and transcriptomic data to better understand the metabolic pathway alterations of each model.

Ongoing studies are extending the RCC primary cell culture model to RCC cell culture-generated xenograft models and characterizing several more RCC PDXs from a wide range of RCC subtypes, pathologic grades and clinical stages. Previous studies on orthotopic RCC xenografts derived from immortalized human RCC cell lines have shown that tumor cellularity varies between the models based on quantitative image analysis of H&E-stained tissue sections and ADC values from ^{1}H diffusion-weighted MRI[224]. Since cellularity can greatly affect the metabolic activity observed using NMR-based metabolomics and hyperpolarized ^{13}C MRI, it will

be critical to assess cellularity in the RCC PDX models in future studies. Characterization of hyperpolarized ^{13}C urea with other perfusion markers such as dynamic contrast enhancement (DCE) studies can also enhance our understanding of cellularity in these RCC models.

Limitations of this study include the inherent insensitivity of NMR, which prevents characterization of low-concentration intermediates of glycolysis, TCA cycle, and fatty acid metabolism. In this study, the metabolic activity of hyperpolarized ^{13}C pyruvate activity was assessed using Lac/Pyr ratio from a single-timepoint CSI data. However the Lac/Pyr ratios cannot be directly compared between TSC bioreactor and PDX studies since the TSC bioreactor model has an excess of HP [1-^{13}C]pyruvate in the medium over the course of the dynamic ^{13}C NMR acquisition that is not present in the PDX model. Future work will fit dynamic 2D CSI to kinetic models[225] to compare the apparent HP ^{13}C pyruvate-to-lactate conversion rate (k_{PL}) between the TSC bioreactor and PDX models using an input-less two-compartment model. Further metabolic comparisons can be obtained from hyperpolarized ^{13}C studies on the cell model for direct comparison with the PDX and TSC models, despite challenges to obtain sufficient cells (~20 million) cells for HP ^{13}C cell slurry or bioreactor studies.

In summary, an initial assessment of metabolism in patient-derived RCC models was performed by combining HP ^{13}C MR imaging studies with metabolomic profiling of steady-state concentrations of metabolites in aerobic glycolysis, glutaminolysis, and the TCA cycle. The results of this study also provide insight into the limitations associated with using these model systems for metabolic studies. Future work will integrate our metabolic findings with lipid metabolism and whole transcriptome profiling.

REFERENCES

1. Hirschey, M. D. *et al.* Dysregulated metabolism contributes to oncogenesis. *Seminars in Cancer Biology* **35,** S129–S150 (2015).
2. Lehuédé, C., Dupuy, F., Rabinovitch, R., Jones, R. G. & Siegel, P. M. Metabolic Plasticity as a Determinant of Tumor Growth and Metastasis. *Cancer Research* **76,** 5201–5208 (2016).
3. Beloribi-Djefaflia, S., Vasseur, S. & Guillaumond, F. Lipid metabolic reprogramming in cancer cells. *Oncogenesis* **5,** e189–e189 (2016).
4. DeBerardinis, R. J. & Chandel, N. S. Fundamentals of cancer metabolism. *Sci. Adv.* **2,** (2016).
5. Ward, P. S. & Thompson, C. B. Metabolic Reprogramming: A Cancer Hallmark Even Warburg Did Not Anticipate. *Cancer Cell* **21,** 297–308 (2012).
6. Muthu, M. & Nordström, A. Current Status and Future Prospects of Clinically Exploiting Cancer-specific Metabolism—Why Is Tumor Metabolism Not More Extensively Translated into Clinical Targets and Biomarkers? *International Journal of Molecular Sciences 2016, Vol. 17, Page 1208* **20,** 1385 (2019).
7. Fendt, S.-M. *et al.* Tradeoff between enzyme and metabolite efficiency maintains metabolic homeostasis upon perturbations in enzyme capacity. *Molecular Systems Biology* **6,** 356 (2010).
8. Duckwall, C. S., Murphy, T. A. & Young, J. D. Mapping cancer cell metabolism with13C flux analysis: Recent progress and future challenges. *Journal of Carcinogenesis* **12,** 13 (2013).

9. Bruntz, R. C., Lane, A. N., Higashi, R. M. & Fan, T. W. M. Exploring cancer metabolism using stable isotope-resolved metabolomics (SIRM). *J. Biol. Chem.* **292,** 11601–11609 (2017).

10. Armitage, E. G. & Barbas, C. Metabolomics in cancer biomarker discovery: Current trends and future perspectives. *Journal of Pharmaceutical and Biomedical Analysis* **87,** 1–11 (2014).

11. Liang, S.-L. & Chan, D. W. Enzymes and related proteins as cancer biomarkers: A proteomic approach. *Clinica Chimica Acta* **381,** 93–97 (2007).

12. Siegel, R. L., Miller, K. D. & Jemal, A. Cancer statistics, 2019. *CA: A Cancer Journal for Clinicians* **69,** 7–34 (2019).

13. Fradet, V. *et al.* Prostate Cancer Managed with Active Surveillance: Role of Anatomic MR Imaging and MR Spectroscopic Imaging1. *Radiology* **256,** 176–183 (2010).

14. Aggarwal, R. & Kurhanewicz, J. Prostate cancer in 2013: The changing role of imaging in clinical care. *Nature Reviews Urology* **11,** 75–77 (2014).

15. Kelloff, G. J., Choyke, P. & Coffey, D. S. Challenges in Clinical Prostate Cancer: Role of Imaging. *American Journal of Roentgenology* **192,** 1455–1470 (2012).

16. Wallace, T. J. *et al.* Current Approaches, Challenges and Future Directions for Monitoring Treatment Response in Prostate Cancer. *Journal of Cancer* **5,** 3–24 (2014).

17. Shore, N., Heidenreich, A. & Saad, F. Predicting Response and Recognizing Resistance: Improving Outcomes in Patients With Castration-resistant Prostate Cancer. *Urology* **109,** 6–18 (2017).

18. Costello, L. C. & Franklin, R. B. Novel role of zinc in the regulation of prostate citrate metabolism and its implications in prostate cancer. *Prostate* **35,** 285–296 (1998).

19. Costello, L. C. & Franklin, R. B. The clinical relevance of the metabolism of prostate cancer; zinc and tumor suppression: connecting the dots. *Molecular Cancer 2008 7:1* **5,** 1–13 (2006).

20. Costello, L. C., Franklin, R. B. & Feng, P. Mitochondrial function, zinc, and intermediary metabolism relationships in normal prostate and prostate cancer. *Mitochondrion* **5,** 143–153 (2005).

21. Albers, M. J. *et al.* Hyperpolarized 13C Lactate, Pyruvate, and Alanine: Noninvasive Biomarkers for Prostate Cancer Detection and Grading. *Cancer Research* **68,** 8607–8615 (2008).

22. Tessem, M. B. *et al.* Evaluation of lactate and alanine as metabolic biomarkers of prostate cancer using 1H HR-MAS spectroscopy of biopsy tissues. *Magn. Reson. Med.* **60,** 510–516 (2008).

23. Kurhanewicz, J. & Vigneron, D. B. in *Handbook of Magnetic Resonance Spectroscopy In Vivo MR Theory, Practice and Applications* 997–1023 (John Wiley & Sons Ltd, 2016).

24. Chen, H.-Y. *et al.* Assessing Prostate Cancer Aggressiveness with Hyperpolarized Dual-Agent 3D Dynamic Imaging of Metabolism and Perfusion. *Cancer Research* **77,** 3207–3216 (2017).

25. Aggarwal, R., Vigneron, D. B. & Kurhanewicz, J. Hyperpolarized 1-[13C]-Pyruvate Magnetic Resonance Imaging Detects an Early Metabolic Response to Androgen Ablation Therapy in Prostate Cancer. *European Urology* **72,** 1028–1029 (2017).

26. Kurhanewicz, J. *et al.* Hyperpolarized 13C MRI: Path to Clinical Translation in Oncology. *Neoplasia* **21,** 1–16 (2019).

27. Ryan, C. J. & Small, E. J. Role of secondary hormonal therapy in the management of recurrent prostate cancer. *Urology* **62,** 87–94 (2003).

28. Crawford, E. D., Petrylak, D. & Sartor, O. Navigating the evolving therapeutic landscape in advanced prostate cancer. *Urologic Oncology: Seminars and Original Investigations* **35,** S1–S13 (2017).

29. Bok, R. A. *et al.* Vascular Endothelial Growth Factor and Basic Fibroblast Growth Factor Urine Levels as Predictors of Outcome in Hormone-refractory Prostate Cancer Patients: A Cancer and Leukemia Group B Study. *Cancer Research* **61,** 2533–2536 (2001).

30. Tran, C. *et al.* Development of a Second-Generation Antiandrogen for Treatment of Advanced Prostate Cancer. *Science* **324,** 787–790 (2009).

31. Watson, P. A., Arora, V. K. & Sawyers, C. L. Emerging mechanisms of resistance to androgen receptor inhibitors in prostate cancer. *Nature Reviews Cancer* (2015).

32. Aggarwal, R., Zhang, T., Small, E. J. & Armstrong, A. J. Neuroendocrine Prostate Cancer: Subtypes, Biology, and Clinical Outcomes. *J Natl Compr Canc Netw* **12,** 719–726 (2014).

33. Siegel, R. L., Miller, K. D. & Jemal, A. Cancer statistics, 2016. *CA: A Cancer Journal for Clinicians* **66,** 7–30 (2016).

34. Wang, H. T. *et al.* Neuroendocrine Prostate Cancer (NEPC) Progressing From Conventional Prostatic Adenocarcinoma: Factors Associated With Time to Development of NEPC and Survival From NEPC Diagnosis—A Systematic Review and Pooled Analysis. *JCO* **32,** 3383–3390 (2014).

35. Missiaglia, E. *et al.* Pancreatic Endocrine Tumors: Expression Profiling Evidences a Role for AKT-mTOR Pathway. *JCO* **28,** 245–255 (2010).

36. Umemura, S. *et al.* Therapeutic Priority of the PI3K/AKT/mTOR Pathway in Small Cell Lung Cancers as Revealed by a Comprehensive Genomic Analysis. *Journal of Thoracic Oncology* **9,** 1324–1331 (2014).

37. Miller, D. M., Thomas, S. D., Islam, A., Muench, D. & Sedoris, K. c-Myc and Cancer Metabolism. *Clin Cancer Res* **18,** 5546–5553 (2012).

38. Johnson, D. C. *et al.* Preoperatively Misclassified, Surgically Removed Benign Renal Masses: A Systematic Review of Surgical Series and United States Population Level Burden Estimate. *The Journal of Urology* **193,** 30–35 (2015).

39. Ciccarese, C. *et al.* The prospect of precision therapy for renal cell carcinoma. *Cancer Treatment Reviews* **49,** 37–44 (2016).

40. Ellis, L. M. & Fidler, I. J. Finding the tumor copycat: Therapy fails, patients don't. *Nature Medicine* **16,** 974–975 (2010).

41. Johnson, J. I. *et al.* Relationships between drug activity in NCI preclinical in vitro and in vivo models and early clinical trials. *British Journal of Cancer 2001 84:10* **84,** 1424–1431 (2001).

42. Buescher, J. M. *et al.* A roadmap for interpreting 13C metabolite labeling patterns from cells. *Current Opinion in Biotechnology* **34,** 189–201 (2015).

43. Fan, T. W. M. & Lane, A. N. NMR-based stable isotope resolved metabolomics in systems biochemistry. *J Biomol NMR* **49,** 267–280 (2011).

44. Magkos, F. & Mittendorfer, B. Stable isotope-labeled tracers for the investigation of fatty acid and triglyceride metabolism in humans in vivo. *Clinical Lipidology* (2017). doi:10.1555/clp.09.9

45. Metallo, C. M., Walther, J. L. & Stephanopoulos, G. Evaluation of 13C isotopic tracers for metabolic flux analysis in mammalian cells. *Journal of Biotechnology* **144,** 167–174 (2009).

46. Walther, J. L., Metallo, C. M., Zhang, J. & Stephanopoulos, G. Optimization of 13C isotopic tracers for metabolic flux analysis in mammalian cells. *Metabolic Engineering* **14,** 162–171 (2012).

47. Ahn, W. S. & Antoniewicz, M. R. Parallel labeling experiments with [1,2-13C]glucose and [U-13C]glutamine provide new insights into CHO cell metabolism. *Metabolic Engineering* **15,** 34–47 (2013).

48. Amaral, A. A comprehensive metabolic profile of cultured astrocytes using isotopic transient metabolic flux analysis and 13C-labeled glucose. *Front. Neuroenerg.* **3,** (2011).

49. Lane, A. N., Yan, J. & Fan, T. W. M. 13C Tracer Studies of Metabolism in Mouse Tumor Xenografts. *Bio-protocol* **5,** (2015).

50. Boyd, L. K., Mao, X. & Lu, Y.-J. The complexity of prostate cancer: genomic alterations and heterogeneity. *Nature Reviews Urology* **9,** 652–664 (2012).

51. Berglund, E. *et al.* Spatial maps of prostate cancer transcriptomes reveal an unexplored landscape of heterogeneity. *Nature Communications 2019 10:1* **9,** 1–13 (2018).

52. Lin, D. *et al.* Metabolic heterogeneity signature of primary treatment-naïve prostate cancer. *Oncotarget* **8,** 25928 (2017).

53. Wang, Y., Ma, S. & Ruzzo, W. L. Spatial modeling of prostate cancer metabolism reveals extensive heterogeneity and selective vulnerabilities. *bioRxiv* **136,** 719294 (2019).

54. López, J. I. & Angulo, J. C. Pathological Bases and Clinical Impact of Intratumor Heterogeneity in Clear Cell Renal Cell Carcinoma. *Curr Urol Rep* **19,** 3 (2018).

55. Beksac, A. T. *et al.* Heterogeneity in renal cell carcinoma. *Urologic Oncology: Seminars and Original Investigations* **35,** 507–515 (2017).

56. Kim, K.-T. *et al.* Application of single-cell RNA sequencing in optimizing a combinatorial therapeutic strategy in metastatic renal cell carcinoma. *Genome Biol* **17,** 1–17 (2016).

57. Okegawa, T. *et al.* Intratumor Heterogeneity in Primary Kidney Cancer Revealed by Metabolic Profiling of Multiple Spatially Separated Samples within Tumors. *EBioMedicine* **19,** 31–38 (2017).

58. Soultati, A., Stares, M., Swanton, C., Larkin, J. & Turajlic, S. How should clinicians address intratumour heterogeneity in clear cell renal cell carcinoma? *Current Opinion in Urology* **25,** 358–366 (2015).

59. Lyssiotis, C. A. & Kimmelman, A. C. Metabolic Interactions in the Tumor Microenvironment. *Trends in Cell Biology* **27,** 863–875 (2017).

60. Chiarugi, P., Paoli, P. & Cirri, P. Tumor Microenvironment and Metabolism in Prostate Cancer. *Seminars in Oncology* **41,** 267–280 (2014).

61. Brauer, H. A. *et al.* Impact of Tumor Microenvironment and Epithelial Phenotypes on Metabolism in Breast Cancer. *Clin Cancer Res* **19,** 571–585 (2013).

62. Wang, Y. *et al.* Development and characterization of efficient xenograft models for benign and malignant human prostate tissue. *Prostate* **64,** 149–159 (2005).

63. Gowda, G. A. N. & Raftery, D. *NMR-Based Metabolomics*. (Humana, 2019).

64. Haukaas, T. H. *et al.* Impact of Freezing Delay Time on Tissue Samples for Metabolomic Studies. *Front. Oncol.* **6,** 63 (2016).

65. Burden, D. W. Guide to the homogenization of biological samples. *Random Primers.* (2008).

66. Folch, J. & Lees, M. A simple method for the isolation and purification of total lipides from animal tissues. *Journal of Biological Chemistry*

67. Fan, T. W.M. in *The Handbook of Metabolomics* (eds. Fan, T. W.-M., Lane, A. N. & Higashi, R. M.) 7–27 (Humana Press, 2012). doi:10.1007/978-1-61779-618-0_2

68. Prasad Maharjan, R. & Ferenci, T. Global metabolite analysis: the influence of extraction methodology on metabolome profiles of Escherichia coli. *Analytical Biochemistry* **313,** 145–154 (2003).

69. Fan, T. W.M. in *The Handbook of Metabolomics* **43,** 439–480 (Humana Press, Totowa, NJ, 2012).

70. Meneses, P. & Glonek, T. High resolution 31P NMR of extracted phospholipids. *J. Lipid Res.* **29,** 679–689 (1988).

71. Serge Akoka, Laurent Barantin, A. & Trierweiler, M. Concentration Measurement by Proton NMR Using the ERETIC Method. *Anal. Chem.* **71,** 2554–2557 (1999).

72. Wider, G. & Dreier, L. Measuring Protein Concentrations by NMR Spectroscopy. *J. Am. Chem. Soc.* **128,** 2571–2576 (2006).

73. Wishart, D. S., Mandal, R., Stanislaus, A. & Ramirez-Gaona, M. Cancer Metabolomics and the Human Metabolome Database. *Metabolites* **6,** 10 (2016).

74. Levin, Y. S. *et al.* Methods for metabolic evaluation of prostate cancer cells using proton and 13C HR-MAS spectroscopy and [3- 13C] pyruvate as a metabolic substrate. *Magn. Reson. Med.* **62,** 1091–1098 (2009).

75. Tiainen, M., Maaheimo, H., Soininen, P. & Laatikainen, R. 13C isotope effects on 1H chemical shifts: NMR spectral analysis of 13C-labelled D-glucose and some 13C-labelled amino acids. *Magnetic Resonance in Chemistry* **48,** 117–122 (2010).

76. Casu, M., Anderson, G. J., Choi, G. & Gibbons, W. A. NMR lipid profiles of cells, tissues and body fluids. I— 1D and 2D Proton NMR of lipids from rat liver. *Magnetic Resonance in Chemistry* **29,** 594–602 (1991).

77. Oostendorp, M. Diagnosing Inborn Errors of Lipid Metabolism with Proton Nuclear Magnetic Resonance Spectroscopy. *Clinical Chemistry* **52,** 1395–1405 (2006).

78. Lane, A. N. & Fan, T. W. M. Quantification and identification of isotopomer distributions of metabolites in crude cell extracts using 1H TOCSY. *Metabolomics* **3,** 79–86 (2007).

79. Deelchand, D. K., Uğurbil, K. & Henry, P. G. Investigating brain metabolism at high fields using localized 13C NMR spectroscopy without 1H decoupling. *Magn. Reson. Med.* **55,** 279–286 (2006).

80. Yu, B. *et al.* More accurate 1JCH coupling measurement in the presence of 3JHH strong coupling in natural abundance. *Journal of Magnetic Resonance* **215,** 10–22 (2012).

81. Lewis, I. A. *et al.* Method for Determining Molar Concentrations of Metabolites in Complex Solutions from Two-Dimensional 1H− 13C NMR Spectra. *Anal. Chem.* **79,** 9385–9390 (2007).

82. Michel, N. & Akoka, S. The application of the ERETIC method to 2D-NMR. *Journal of Magnetic Resonance* **168,** 118–123 (2004).

83. Heikkinen, S., Toikka, M. M., Karhunen, P. T. & Kilpeläinen, I. A. *Quantitative 2D HSQC (Q-HSQC) via Suppression of J-Dependence of Polarization Transfer in NMR*

Spectroscopy: Application to Wood Lignin. *Journal of the American Chemical Society* **125,** 4362–4367 (American Chemical Society, 2003).

84. Peterson, D. J. & Loening, N. M. QQ-HSQC: a quick, quantitative heteronuclear correlation experiment for NMR spectroscopy. *Magnetic Resonance in Chemistry* **45,** 937–941 (2007).

85. Koskela, H., Heikkilä, O., Kilpeläinen, I. & Heikkinen, S. Quantitative two-dimensional HSQC experiment for high magnetic field NMR spectrometers. *Journal of Magnetic Resonance* **202,** 24–33 (2010).

86. Hu, K., Westler, W. M. & Markley, J. L. Simultaneous Quantification and Identification of Individual Chemicals in Metabolite Mixtures by Two-Dimensional Extrapolated Time-Zero 1H−13C HSQC (HSQC0). *J. Am. Chem. Soc.* **133,** 1662–1665 (2011).

87. Castañar, L., Sistaré, E., Virgili, A., Williamson, R. T. & Parella, T. Suppression of phase and amplitude J(HH) modulations in HSQC experiments. *Magnetic Resonance in Chemistry* **53,** 115–119 (2015).

88. Sherry, A. D. & Malloy, C. R. 13C Isotopomer Analysis of Glutamate A NMR Method to Probe Metabolic Pathways Intersecting in the Citric Acid Cycle. *In Vivo Carbon-13 NMR* (2002). doi:10.1007/0-306-47078-0_2

89. Antoniewicz, M. R. A guide to 13 C metabolic flux analysis for the cancer biologist. *Exp Mol Med* **50,** 1–13 (2018).

90. Malloy, C. R., Sherry, A. D. & Jeffrey, F. M. Evaluation of carbon flux and substrate selection through alternate pathways involving the citric acid cycle of the heart by 13C NMR spectroscopy. *J. Biol. Chem.* **263,** 6964–6971 (1988).

91. Sherry, A. D., Jeffrey, F. M. H. & Malloy, C. R. Analytical solutions for 13C isotopomer analysis of complex metabolic conditions: substrate oxidation, multiple pyruvate cycles, and gluconeogenesis. *Metabolic Engineering* **6,** 12–24 (2004).

92. Weitzel, M. *et al.* 13CFLUX2—high-performance software suite for 13C-metabolic flux analysis. *Bioinformatics* **29,** 143–145 (2013).

93. Young, J. D. INCA: a computational platform for isotopically non-stationary metabolic flux analysis. *Bioinformatics* **30,** 1333–1335 (2014).

94. Zamboni, N., Fischer, E. & Sauer, U. FiatFlux – a software for metabolic flux analysis from 13 C-glucose experiments. *BMC Bioinformatics 2014 15:1* **6,** 1–8 (2005).

95. Sriram, G. *et al.* Quantification of Compartmented Metabolic Fluxes in Developing Soybean Embryos by Employing Biosynthetically Directed Fractional 13C Labeling, Two-Dimensional [13C, 1H] Nuclear Magnetic Resonance, and Comprehensive Isotopomer Balancing. *Plant Physiology* **136,** 3043–3057 (2004).

96. Young, J. D., Walther, J. L., Antoniewicz, M. R., Yoo, H. & Stephanopoulos, G. An elementary metabolite unit (EMU) based method of isotopically nonstationary flux analysis. *Biotechnol Bioeng* **99,** 686–699 (2008).

97. Quek, L.-E., Wittmann, C., Nielsen, L. K. & Krömer, J. O. OpenFLUX: efficient modelling software for 13 C-based metabolic flux analysis. *Microbial Cell Factories 2005 4:1* **8,** 1–15 (2009).

98. Wiechert, W., Möllney, M., Petersen, S. & de Graaf, A. A. A Universal Framework for 13C Metabolic Flux Analysis. *Metabolic Engineering* **3,** 265–283 (2001).

99. Wiechert, W., Möllney, M., Isermann, N., Wurzel, M. & de Graaf, A. A. Bidirectional reaction steps in metabolic networks: III. Explicit solution and analysis of isotopomer labeling systems. *Biotechnol Bioeng* **66,** 69–85 (1999).

100. Antoniewicz, M. R., Kelleher, J. K. & Stephanopoulos, G. Elementary metabolite units (EMU): A novel framework for modeling isotopic distributions. *Metabolic Engineering* **9,** 68–86 (2007).

101. Weinman, E. O., Strisower, E. H. & Chaikoff, I. L. Conversion of Fatty Acids to Carbohydrate: Application of Isotopes to this Problem and Role of the Krebs Cycle as a Synthetic Pathway. *Physiological Reviews* **37,** 252–272 (1957).

102. Malloy, C. R., Sherry, A. D. & Jeffrey, F. M. Analysis of tricarboxylic acid cycle of the heart using 13C isotope isomers. *American Journal of Physiology - Heart and Circulatory Physiology* **259,** H987–H995 (1990).

103. Keshari, K. R. *et al.* Hyperpolarized 13C spectroscopy and an NMR-compatible bioreactor system for the investigation of real-time cellular metabolism. *Magn. Reson. Med.* **63,** 322–329 (2010).

104. Sriram, R. *et al.* Real-time measurement of hyperpolarized lactate production and efflux as a biomarker of tumor aggressiveness in an MR compatible 3D cell culture bioreactor. *NMR Biomed.* **28,** 1141–1149 (2015).

105. Sriram, R. *et al.* Detection of Bacteria-Specific Metabolism Using Hyperpolarized [2-13C]Pyruvate. *ACS Infectious Diseases* **4,** 797–805 (2018).

106. Sriram, R. *et al.* Molecular detection of inflammation in cell models using hyperpolarized 13C-pyruvate. *Theranostics* **8,** 3400–3407 (2018).

107. Sriram, R. *et al.* Real-time measurement of hyperpolarized lactate production and efflux as a biomarker of tumor aggressiveness in an MR compatible 3D cell culture bioreactor. *NMR Biomed.* **28,** 1141–1149 (2015).

108. Gerencser, A. A. *et al.* Quantitative Microplate-Based Respirometry with Correction for Oxygen Diffusion. *Anal. Chem.* **81,** 6868–6878 (2009).

109. Wang, Z. J. *et al.* Hyperpolarized 13C MRI: State of the Art and Future Directions. *Radiology* **291,** 273–284 (2019).

110. Ardenkjær-Larsen, J. H. *et al.* Increase in signal-to-noise ratio of >10,000 times in liquid-state NMR. *PNAS* **100,** 10158–10163 (2003).

111. Comment, A. & Merritt, M. E. Hyperpolarized Magnetic Resonance as a Sensitive Detector of Metabolic Function. *Biochemistry* **53,** 7333–7357 (2014).

112. Gillies, R. J., Liu, Z. & Bhujwalla, Z. 31P-MRS measurements of extracellular pH of tumors using 3-aminopropylphosphonate. *American Journal of Physiology-Cell Physiology* **267,** C195–C203 (1994).

113. Wolfe, S. P., Hsu, E., Reid, L. M. & Macdonald, J. M. A novel multi-coaxial hollow fiber bioreactor for adherent cell types. Part 1: Hydrodynamic studies. *Biotechnol Bioeng* **77,** 83–90 (2002).

114. Mancuso, A. *et al.* Artificial tumor model suitable for monitoring 31P and 13C NMR spectroscopic changes during chemotherapy-induced apoptosis in human glioma cells. *Magn. Reson. Med.* **54,** 67–78 (2005).

115. Keshari, K. R. *et al.* Metabolic Reprogramming and Validation of Hyperpolarized 13C Lactate as a Prostate Cancer Biomarker Using a Human Prostate Tissue Slice Culture Bioreactor. *Prostate* **73,** 1171–1181 (2013).

116. Gordon, J. W. & Larson, P. E. Z. *Pulse Sequences for Hyperpolarized MRS*. **55,** 1229–1246 (John Wiley & Sons, Ltd, 2007).

117. Zhang, V. Y. Monitoring Tumor Response of Prostate Cancer to Radiation Therapy by Multi-parametric 1H and Hyperpolarized 13C Magnetic Resonance Imaging. (2014).

118. Qin, H. *et al.* Imaging glutathione depletion in the rat brain using ascorbate-derived hyperpolarized MR and PET probes. *Scientific Reports* **8,** 1–9 (2018).

119. Najac, C. *et al.* In vivo investigation of hyperpolarized [1,3- 13 C 2]acetoacetate as a metabolic probe in normal brain and in glioma. *Scientific Reports* **9,** 3402 (2019).

120. Golman, K., Zandt, R. I., Lerche, M., Pehrson, R. & Ardenkjaer-Larsen, J. H. Metabolic Imaging by Hyperpolarized 13C Magnetic Resonance Imaging for In vivo Tumor Diagnosis. *Cancer Research* **66,** 10855–10860 (2006).

121. Sukumar, S., Larson, P. E., Keshari, K. R., Kurhanewicz, J. & Vigneron, D. B. Single Shot, Chemical Shift Specific Imaging Methods for Hyperpolarized Carbon--13 Studies at 14T. *Proceedings of the International Society of Magnetic Resonance in Medicine* **11th Scientific Meeting,** 3268 (2010).

122. Bok, R. *et al.* The Role of Lactate Metabolism in Prostate Cancer Progression and Metastases Revealed by Dual-Agent Hyperpolarized 13C MRSI. *Cancers 2011, Vol. 11, Page 257* **11,** 257 (2019).

123. Chen, A. P. *et al.* Hyperpolarized C-13 spectroscopic imaging of the TRAMP mouse at 3T—Initial experience. *Magn. Reson. Med.* **58,** 1099–1106 (2007).

124. Cunningham, C. H. *et al.* Double spin-echo sequence for rapid spectroscopic imaging of hyperpolarized 13C. *Journal of Magnetic Resonance* **187,** 357–362 (2007).

125. Nelson, S. J. *et al.* Metabolic Imaging of Patients with Prostate Cancer Using Hyperpolarized [1-13C]Pyruvate. *Science Translational Medicine* **5,** 198ra108–198ra108 (2013).

126. Gordon, J. W. *et al.* Translation of Carbon-13 EPI for hyperpolarized MR molecular imaging of prostate and brain cancer patients. *Magn. Reson. Med.* **81,** 2702–2709 (2019).

127. Morze, von, C. *et al.* Frequency-specific SSFP for hyperpolarized 13C metabolic imaging at 14.1 T. *Magnetic Resonance Imaging* **31,** 163–170 (2013).

128. Milshteyn, E. *et al.* High spatiotemporal resolution bSSFP imaging of hyperpolarized [1-13C]pyruvate and [1-13C]lactate with spectral suppression of alanine and pyruvate-hydrate. *Magn. Reson. Med.* **80,** 1048–1060 (2018).

129. Tang, S. *et al.* A regional bolus tracking and real-time B1 calibration method for hyperpolarized 13C MRI. *Magn. Reson. Med.* **81,** 839–851 (2019).

130. Kirby, M., Hirst, C. & Crawford, E. D. Characterising the castration-resistant prostate cancer population: a systematic review. *International Journal of Clinical Practice* **65,** 1180–1192 (2011).

131. Koochekpour, S. Androgen receptor signaling and mutations in prostate cancer. *Asian Journal of Andrology* **12,** 639–657 (2010).

132. Jernberg, E., Bergh, A. & Wikström, P. Clinical relevance of androgen receptor alterations in prostate cancer. *Endocrine Connections* **6,** R146–R161 (2017).

133. Sharma, N. L. *et al.* The Androgen Receptor Induces a Distinct Transcriptional Program in Castration-Resistant Prostate Cancer in Man. *Cancer Cell* **23,** 35–47 (2013).

134. Massie, C. E. *et al.* The androgen receptor fuels prostate cancer by regulating central metabolism and biosynthesis. *The EMBO Journal* **30,** 2719–2733 (2011).

135. Coller, H. A. Is Cancer a Metabolic Disease? *The American Journal of Pathology* **184,** 4–17 (2014).

136. Horoszewicz, J. S. *et al.* LNCaP Model of Human Prostatic Carcinoma. *Cancer Research* **43,** 1809–1818 (1983).

137. Kaighn, M. E., Narayan, K. S., Ohnuki, Y., Lechner, J. F. & Jones, L. W. Establishment and characterization of a human prostatic carcinoma cell line (PC-3). *Invest Urol* **17,** 16–23 (1979).

138. Gingrich, J. R. *et al.* Androgen-independent Prostate Cancer Progression in the TRAMP Model. *Cancer Research* **57,** 4687–4691 (1997).

139. Huss, W. J., Hanrahan, C. F., Barrios, R. J., Simons, J. W. & Greenberg, N. M. Angiogenesis and Prostate Cancer: Identification of A Molecular Progression Switch. *Cancer Research* **61,** 2736–2743 (2001).

140. Costello, L. C. *et al.* Human prostate cancer ZIP1/zinc/citrate genetic/metabolic relationship in the TRAMP prostate cancer animal model. *Cancer Biology & Therapy* **12,** 1078–1084 (2011).

141. Hurd, R. E., Yen, Y.-F., Chen, A. & Ardenkjaer-Larsen, J. H. Hyperpolarized 13C metabolic imaging using dissolution dynamic nuclear polarization. *Journal of Magnetic Resonance Imaging* **36,** 1314–1328 (2012).

142. Crawford, E. D. Hormonal Therapy in Prostate Cancer: Historical Approaches. *Reviews in Urology* **6,** S3 (2004).

143. Gomella, L. G. Effective Testosterone Suppression for Prostate Cancer: Is There a Best Castration Therapy? *Reviews in Urology* **11,** 52

144. Clegg, N. J. *et al.* ARN-509: A Novel Antiandrogen for Prostate Cancer Treatment. *Cancer Research* **72,** 1494–1503 (2012).

145. Malloy, C. R., Thompson, J. R., Jeffrey, F. & Sherry, A. D. Contribution of exogenous substrates to acetyl coenzyme A: measurement by carbon-13 NMR under non-steady-state conditions. *Biochemistry* (1990).

146. Jeffrey, F. M., Storey, C. J., Sherry, A. D. & Malloy, C. R. 13C isotopomer model for estimation of anaplerotic substrate oxidation via acetyl-CoA. *American Journal of Physiology - Endocrinology and Metabolism* **271,** E788–E799 (1996).

147. Guo, H. *et al.* ONECUT2 is a driver of neuroendocrine prostate cancer. *Nature Communications 2019 10:1* **10,** 278 (2019).

148. Chaiswing, L., Zhong, W. & Oberley, T. D. Distinct Redox Profiles of Selected Human Prostate Carcinoma Cell Lines: Implications for Rational Design of Redox Therapy. *Cancers 2011, Vol. 11, Page 257* **3,** 3557–3584 (2011).

149. Owen, O. E., Kalhan, S. C. & Hanson, R. W. The Key Role of Anaplerosis and Cataplerosis for Citric Acid Cycle Function. *J. Biol. Chem.* **277,** 30409–30412 (2002).

150. Balaban, R. S. Regulation of oxidative phosphorylation in the mammalian cell. *American Journal of Physiology-Cell Physiology* **258,** C377–C389 (1990).

151. Zhu, X.-H., Lu, M., Lee, B.-Y., Uğurbil, K. & Chen, W. In vivo NAD assay reveals the intracellular NAD contents and redox state in healthy human brain and their age dependences. *PNAS* **112,** 2876–2881 (2015).

152. Ying, W. NAD +/NADH and NADP +/NADPH in Cellular Functions and Cell Death: Regulation and Biological Consequences. *Antioxidants & Redox Signaling* **10,** 179–206 (2008).

153. Eisenhauer, E. A. *et al.* New response evaluation criteria in solid tumours: Revised RECIST guideline (version 1.1). *European Journal of Cancer* **45,** 228–247 (2009).

154. Higgins, L. H. *et al.* Hypoxia and the metabolic phenotype of prostate cancer cells. *Biochimica et Biophysica Acta (BBA) - Bioenergetics* **1787,** 1433–1443 (2009).

155. Ros, S. *et al.* Functional Metabolic Screen Identifies 6-Phosphofructo-2-Kinase/Fructose-2,6-Biphosphatase 4 as an Important Regulator of Prostate Cancer Cell Survival. *Cancer Discovery* **2,** 328–343 (2012).

156. Vaz, C. V. *et al.* Androgen-responsive and nonresponsive prostate cancer cells present a distinct glycolytic metabolism profile. *The International Journal of Biochemistry & Cell Biology* **44,** 2077–2084 (2012).

157. Li, W. *et al.* The Role of CD44 in Glucose Metabolism in Prostatic Small Cell Neuroendocrine Carcinoma. *Mol Cancer Res* **14,** 344–353 (2016).

158. Zacharias, N. M. *et al.* Metabolic Differences in Glutamine Utilization Lead to Metabolic Vulnerabilities in Prostate Cancer. *Scientific Reports* **7,** 637 (2017).

159. Warburg, O., Wind, F. & Negelein, E. THE METABOLISM OF TUMORS IN THE BODY. *The Journal of General Physiology* **8,** 519–530 (1927).

160. Zheng, J. Energy metabolism of cancer: Glycolysis versus oxidative phosphorylation (Review). *Oncology Letters* **4,** 1151–1157 (2012).

161. Warburg, O. On the origin of cancer cells. *Science* **123,** 309–314 (1956).

162. Abeshouse, A. *et al.* The Molecular Taxonomy of Primary Prostate Cancer. *Cell* **163,** 1011–1025 (2015).

163. Chen, J. *et al.* Compartmentalized activities of the pyruvate dehydrogenase complex sustain lipogenesis in prostate cancer. *Nature Genetics* **50,** 219–228 (2018).

164. Tonry, C., Armstrong, J. & Pennington, S. R. Probing the prostate tumour microenvironment I: impact of glucose deprivation on a cell model of prostate cancer progression. *Oncotarget* **8,** (2017).

165. Wang, Q. *et al.* Targeting ASCT2-mediated glutamine uptake blocks prostate cancer growth and tumour development. *The Journal of Pathology* **236,** 278–289 (2015).

166. Naiki, T., Naiki-Ito, A., Asamoto, M. & Kawai, N. GPX2 overexpression is involved in cell proliferation and prognosis of castration-resistant prostate cancer. *Carcinogenesis* **35,** 1962–1967 (2014).

167. Liou, G.-Y. & Storz, P. Reactive oxygen species in cancer. *Free Radical Research* **44,** 479–496 (2010).

168. LIU, Y., ZUCKIER, L. S. & GHESANI, N. V. Dominant Uptake of Fatty Acid over Glucose by Prostate Cells: A Potential New Diagnostic and Therapeutic Approach. *Anticancer Res* **30,** 369–374 (2010).

169. Ryan, C. J. *et al.* Abiraterone in Metastatic Prostate Cancer without Previous Chemotherapy. *http://dx.doi.org/10.1056/NEJMoa1209096* **368,** 138–148 (2013).

170. Beer, T. M. *et al.* Enzalutamide in Metastatic Prostate Cancer before Chemotherapy. *http://dx.doi.org/10.1056/NEJMoa1405095* **371,** 424–433 (2014).

171. Beltran, H. *et al.* Molecular Characterization of Neuroendocrine Prostate Cancer and Identification of New Drug Targets. *Cancer Discovery* **1,** 487–495 (2011).

172. Small, E. J. *et al.* Characterization of neuroendocrine prostate cancer (NEPC) in patients with metastatic castration resistant prostate cancer (mCRPC) resistant to abiraterone (Abi) or enzalutamide (Enz): Preliminary results from the SU2C/PCF/AACR West Coast Prostate Cancer Dream Team (WCDT). *JCO* **33,** 5003–5003 (2017).

173. Vlachostergios, P. J. & Papandreou, C. N. Targeting Neuroendocrine Prostate Cancer: Molecular and Clinical Perspectives. *Front. Oncol.* **5,** 3072 (2015).

174. Santoni, M. *et al.* Neuroendocrine differentiation in prostate cancer: Novel morphological insights and future therapeutic perspectives. *Biochimica et Biophysica Acta (BBA) - Reviews on Cancer* **1846,** 630–637 (2014).

175. Dardenne, E. *et al.* N-Myc Induces an EZH2-Mediated Transcriptional Program Driving Neuroendocrine Prostate Cancer. *Cancer Cell* **30,** 563–577 (2016).

176. Lee, J. K. *et al.* N-Myc Drives Neuroendocrine Prostate Cancer Initiated from Human Prostate Epithelial Cells. *Cancer Cell* **29,** 536–547 (2016).

177. Yin, Y. *et al.* N-Myc promotes therapeutic resistance development of neuroendocrine prostate cancer by differentially regulating miR-421/ATM pathway. *Molecular Cancer 2008 7:1* **18,** 1–13 (2019).

178. Berger, A. *et al.* N-Myc–mediated epigenetic reprogramming drives lineage plasticity in advanced prostate cancer. *J. Clin. Invest.* **129,** 3924–3940 (2019).

179. Dang, C. V. MYC, metabolism, cell growth, and tumorigenesis. *Cold Spring Harbor perspectives in …* (2013).

180. Dang, C. V. c-Myc Target Genes Involved in Cell Growth, Apoptosis, and Metabolism. *Molecular and Cellular Biology* **19,** 1–11 (1999).

181. Chen, H., Liu, H. & Qing, G. Targeting oncogenic Myc as a strategy for cancer treatment. *Sig Transduct Target Ther* **3,** 1–7 (2018).

182. Beltran, H. *et al.* A Phase II Trial of the Aurora Kinase A Inhibitor Alisertib for Patients with Castration-resistant and Neuroendocrine Prostate Cancer: Efficacy and Biomarkers. *Clin Cancer Res* **25,** 43–51 (2019).

183. Gross, M. I. *et al.* Antitumor Activity of the Glutaminase Inhibitor CB-839 in Triple-Negative Breast Cancer. *Mol Cancer Ther* **13,** 890–901 (2014).

184. Lin, D. *et al.* High Fidelity Patient-Derived Xenografts for Accelerating Prostate Cancer Discovery and Drug Development. *Cancer Research* **74,** 1272–1283 (2014).

185. Nguyen, H. M. *et al.* LuCaP Prostate Cancer Patient-Derived Xenografts Reflect the Molecular Heterogeneity of Advanced Disease an--d Serve as Models for Evaluating Cancer Therapeutics. *Prostate* **77,** 654–671 (2017).

186. Hanson, B. A. ChemoSpec: Exploratory Chemometrics for Spectroscopy. *R package version* .. 1–19 (2019).

187. Choi, S. Y. C. *et al.* Targeting MCT4 to reduce lactic acid secretion and glycolysis for treatment of neuroendocrine prostate cancer. *Cancer Medicine* **7,** 3385–3392 (2018).

188. Flores-Morales, A. *et al.* Proteogenomic Characterization of Patient-Derived Xenografts Highlights the Role of REST in Neuroendocrine Differentiation of Castration-Resistant Prostate Cancer. *Clin Cancer Res* **25,** 595–608 (2019).

189. Wise, D. R. *et al.* Myc regulates a transcriptional program that stimulates mitochondrial glutaminolysis and leads to glutamine addiction. *PNAS* **105,** 18782–18787 (2008).

190. Gao, C., Shen, Y., Jin, F., Miao, Y. & Qiu, X. Cancer Stem Cells in Small Cell Lung Cancer Cell Line H446: Higher Dependency on Oxidative Phosphorylation and Mitochondrial Substrate-Level Phosphorylation than Non-Stem Cancer Cells. *PLOS ONE* **11,** e0154576 (2016).

191. DeBerardinis, R. J. *et al.* Beyond aerobic glycolysis: Transformed cells can engage in glutamine metabolism that exceeds the requirement for protein and nucleotide synthesis. *PNAS* **104,** 19345–19350 (2007).

192. Linehan, W. M., Srinivasan, R. & Schmidt, L. S. The genetic basis of kidney cancer: a metabolic disease. *Nature Reviews Urology* **7,** 277–285 (2010).

193. Hakimi, A. A., Pham, C. G. & Hsieh, J. J. A clear picture of renal cell carcinoma. *Nature Genetics* **45,** 849–850 (2013).

194. Massari, F. *et al.* Metabolic alterations in renal cell carcinoma. *Cancer Treatment Reviews* **41,** 767–776 (2015).

195. Gerlinger, M. *et al.* Genomic architecture and evolution of clear cell renal cell carcinomas defined by multiregion sequencing. *Nature Genetics* **46,** 225–233 (2014).

196. Network, T. C. G. A. R. Comprehensive molecular characterization of clear cell renal cell carcinoma. *Nature* **499,** 43–49 (2013).

197. Li, B. *et al.* Fructose-1,6-bisphosphatase opposes renal carcinoma progression. *Nature* **513,** 251–255 (2014).

198. Godinot, C., de Laplanche, E., Hervouet, E. & Simonnet, H. Actuality of Warburg's views in our understanding of renal cancer metabolism. *J Bioenerg Biomembr* **39,** 235–241 (2007).

199. Gatenby, R. A., Gawlinski, E. T., Gmitro, A. F., Kaylor, B. & Gillies, R. J. Acid-Mediated Tumor Invasion: a Multidisciplinary Study. *Cancer Research* **66,** 5216–5223 (2006).

200. Gatenby, R. A. & Gillies, R. J. A microenvironmental model of carcinogenesis. *Nature Reviews Cancer* **8,** 56–61 (2008).

201. Girgis, H. *et al.* Lactate Dehydrogenase A is a potential prognostic marker in clear cell renal cell carcinoma. *Molecular Cancer 2008 7:1* **13,** 1–10 (2014).

202. Gerlinger, M. *et al.* Genome-wide RNA interference analysis of renal carcinoma survival regulators identifies MCT4 as a Warburg effect metabolic target. *The Journal of Pathology* **227,** 146–156 (2012).

203. Fisel, P. *et al.* DNA Methylation of the SLC16A3 Promoter Regulates Expression of the Human Lactate Transporter MCT4 in Renal Cancer with Consequences for Clinical Outcome. *Clin Cancer Res* **19,** 5170–5181 (2013).

204. Fisel, P. *et al.* MCT4 surpasses the prognostic relevance of the ancillary protein CD147 in clear cell renal cell carcinoma. *Oncotarget* **6,** 30615 (2015).

205. Gao, H. *et al.* Application of ex vivo ^{1}H NMR metabonomics to the characterization and possible detection of renal cell carcinoma metastases. *J Cancer Res Clin Oncol* **138,** 753–761 (2012).

206. Lucarelli, G. *et al.* Metabolomic profile of glycolysis and the pentose phosphate pathway identifies the central role of glucose-6-phosphate dehydrogenase in clear cell-renal cell carcinoma. *Oncotarget* **6,** 13371 (2015).

207. Shim, E.-H. *et al.* l-2-Hydroxyglutarate: An Epigenetic Modifier and Putative Oncometabolite in Renal Cancer. *Cancer Discovery* **4,** 1290–1298 (2014).

208. Wettersten, H. I. *et al.* Grade-Dependent Metabolic Reprogramming in Kidney Cancer Revealed by Combined Proteomics and Metabolomics Analysis. *Cancer Research* **75,** 2541–2552 (2015).

209. Chen, F. *et al.* Multilevel Genomics-Based Taxonomy of Renal Cell Carcinoma. *Cell Reports* **14,** 2476–2489 (2016).

210. Thong, A. E. *et al.* Tissue slice grafts of human renal cell carcinoma: An authentic preclinical model with high engraftment rate and metastatic potential. *Urologic Oncology: Seminars and Original Investigations* **32,** 43.e23–43.e30 (2014).

211. Sriram, R. *et al.* Non-Invasive Differentiation of Benign Renal Tumors from Clear Cell Renal Cell Carcinomas Using Clinically Translatable Hyperpolarized 13C Pyruvate Magnetic Resonance. *Tomography* **2,** 35–42 (2016).

212. Young, S. R. *et al.* Establishment and serial passage of cell cultures derived from LuCaP xenografts. *Prostate* **73,** 1251–1262 (2013).

213. Varna, M. *et al.* Stem Cells Increase in Numbers in Perinecrotic Areas in Human Renal Cancer. *Clin Cancer Res* **21,** 916–924 (2015).

214. Glunde, K., Bhujwalla, Z. M. & Ronen, S. M. Choline metabolism in malignant transformation. *Nature Reviews Cancer* **11,** 835–848 (2011).

215. Keshari, K. R. *et al.* Hyperpolarized 13C-Pyruvate Magnetic Resonance Reveals Rapid Lactate Export in Metastatic Renal Cell Carcinomas. *Cancer Research* **73,** 529–538 (2013).

216. Keshari, K. R. *et al.* Hyperpolarized [1-13C]Dehydroascorbate MR Spectroscopy in a Murine Model of Prostate Cancer: Comparison with 18F-FDG PET. *J Nucl Med* **54,** 922–928 (2013).

217. Chandel, N. S. & Budinger, G. R. S. The cellular basis for diverse responses to oxygen. *Free Radical Biology and Medicine* **42,** 165–174 (2007).

218. Kimura, R. E., Thulin, G. E., Wender, D. & Warshaw, J. B. Decreased oxidative metabolism in neonatal rat lung exposed to hyperoxia. *J Appl Physiol* **55,** 1501–1505 (1983).

219. Papas, K. K., Long, R. C., Sambanis, A. & Constantinidis, I. Development of a bioartificial pancreas: II. Effects of oxygen on long-term entrapped βTC3 cell cultures. *Biotechnol Bioeng* **66,** 231–237 (1999).

220. Shimazu, T. *et al.* Suppression of Oxidative Stress by β-Hydroxybutyrate, an Endogenous Histone Deacetylase Inhibitor. *Science* **339,** 211–214 (2013).

221. Wyss, M. & Kaddurah-Daouk, R. Creatine and Creatinine Metabolism. *Physiological Reviews* **80,** 1107–1213 (2000).

222. Kulkarni, A. C., Kuppusamy, P. & Parinandi, N. Oxygen, the Lead Actor in the Pathophysiologic Drama: Enactment of the Trinity of Normoxia, Hypoxia, and Hyperoxia in Disease and Therapy. *https://home.liebertpub.com/ars* **9,** 1717–1730 (2007).

223. Eales, K. L., Hollinshead, K. E. R. & Tennant, D. A. Hypoxia and metabolic adaptation of cancer cells. *Oncogenesis* **5,** e190–e190 (2016).

224. Sriram, R. *et al.* Non-Invasive Assessment of Lactate Production and Compartmentalization in Renal Cell Carcinomas Using Hyperpolarized 13C Pyruvate MRI. *Cancers 2011, Vol. 11, Page 257* **10,** 313 (2018).

225. Zierhut, M. L. *et al.* Kinetic modeling of hyperpolarized 13C1-pyruvate metabolism in normal rats and TRAMP mice. *Journal of Magnetic Resonance* **202,** 85–92 (2010).

Publishing Agreement

It is the policy of the University to encourage open access and broad distribution of all theses, dissertations, and manuscripts. The Graduate Division will facilitate the distribution of UCSF theses, dissertations, and manuscripts to the UCSF Library for open access and distribution. UCSF will make such theses, dissertations, and manuscripts accessible to the public and will take reasonable steps to preserve these works in perpetuity.

I hereby grant the non-exclusive, perpetual right to The Regents of the University of California to reproduce, publicly display, distribute, preserve, and publish copies of my thesis, dissertation, or manuscript in any form or media, now existing or later derived, including access online for teaching, research, and public service purposes.

DocuSigned by:
Jinny Sun
23BB2F3CB66647E...
Author Signature

3/9/2020
Date